Charles University
Faculty of Mathematics and Physics

HABILITATION THESIS

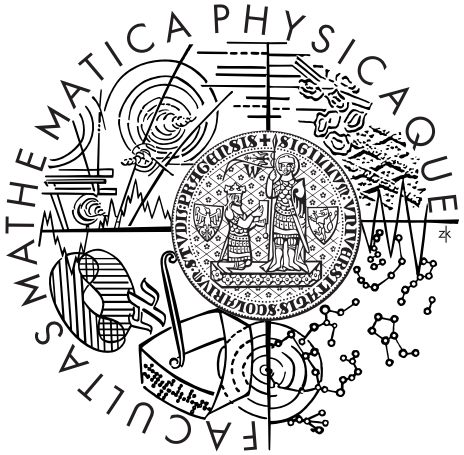

Frustrated magnetism in rare-earth *227* oxides

Milan Klicpera

Department of Condensed Matter Physics

Prague 2024

Preface

The present habilitation thesis summarises my six-year work on the topic of rare-earth oxides crystallising in geometrically frustrated crystallographic lattices. The thesis consists of a set of 17 relevant scientific publications I have authored and co-authored, reprinted at the end of the thesis, and a unifying commentary forming the thesis body, together with an introduction to our recent unpublished results.

During my Ph.D. studies and post-doc work at the Institute Laue-Langevin, Grenoble, France, I have been mostly focused on conductivity and magnetism of intermetallic rare-earth compounds. Commencing my academic career in 2017 at the Department of Condensed Matter Physics (DCMP), Faculty of Mathematics and Physics, Charles University, I completely changed the subject of main interest to oxides crystallising in geometrically frustrated lattices, mostly rare-earth $A_2B_2O_7$ oxides. During the last six years, in cooperation with my students and colleagues, I have established this exciting topic on the ground of the institution; also as a principal investigator and a co-principal investigator of the Czech Science Foundation projects.

At present, world-quality samples, especially single crystals of $A_2Ir_2O_7$ iridates and $A_2Zr_2O_7$ zirconates, are synthesised at the DCMP and their structural and electronic properties are studied at home laboratories, as well as at international large-scale facilities. Importantly, establishing a new scientific direction at the DCMP allowed a broadening of its research field in recent years. Namely, frustrated rare-earth oxides and fluorites or frustrated magnetoelectrics and multiferroics are heavily studied at DCMP nowadays. The frustrated magnetism group, previously non-existent, is currently the largest group at the DCMP, supervising about half of students at the department.

Acknowlegements

I express gratitude to my colleagues from the Department of Condensed Matter Physics: Dr. Ross Harvey Colman; doc. RNDr. Martin Diviš, CSc.; doc. RNDr. Jiří Pospíšil, Ph.D.; prof. Mgr. Pavel Javorský, Dr.; doc. RNDr. Jiří Prchal, Ph.D.; prof. RNDr. Vladimír Sechovský, DrSc.; Gaël Bastien, Ph.D.; and Taras Kovaliuk, Ph.D., for excellent collaboration, friendship, trust, enthusiasm, stimulating scientific discussions, and support in scientific and academic work.

The great thanks belong to my colleagues from large-scale facilities and institutes abroad: Dr. Martin Böhm, Dr. Paul Steffens, Dr. Inés Puente Orench, Dr. Oscar Ramon Fabelo Rosa, Dr. Bachir Ouladdiaf, Dr. Juan Rodríguez-Carvajal, and Dr. Michael Marek Koza from the Institut Laue-Langevin (ILL), Grenoble, France, for their support during my postdoc stay at ILL and continuous collaboration on various scientific projects; Quentin Faure, Ph.D., Dr. João Elias Rodrigues, Ph.D., Dr. Blanka Detlefts, Ph.D., Christoph Sahle, Ph.D., and Dr.

Samuel Tardif, Ph.D. from the European Synchrotron Radiation Facility (ESRF), Grenoble, France, for their enthusiasm and broadening my scientific horizon and technical skills utilising synchrotron radiation techniques in the last two years; Dr. Devashibhai T. Adroja, Dr. Adam Berlie, and Dr. Duc Le from the ISIS Neutron and Muon Source of the Rutherford-Appleton Laboratory, Didcot, United Kingdom, for numerous discussions and contributions to my ongoing research; Dr. Elsa Lhotel from Institut Néel, CNRS, Université Grenoble Alpes, France; and Dr. Sylvain Petit, Ph.D from Université Paris-Sacley, France, for new collaboration opportunities on frustrated magnetism systems and participation in our newly established joint project; and Dr. Koji Kaneko and Dr. Yo Tokunaga from Japan Atomic Energy Agency in Tokai, Japan, for their help with our recent experiments at Japan Proton Accelerator Research Complex (J-PARC), following discussions and new fruitful collaboration.

My thanks also go to RNDr. Jiří Kaštil, Ph.D. from the Institute of Physics of the Academy of Sciences of the Czech Republic (IoF AS CR) for his help with measurements of some bulk properties of synthesised materials; and Margarida Isabel Sousa Henriques, Ph.D. also from IoF AS CR for her structural analyses of newly synthesised samples from $A_2Ir_2O_7$ family. I thank also to Ing. Petr Veřtát, Ph.D.; Ing. Ladislav Straka, D.Sc; and Oleg Heczko, Dr. from IoF AS CR for our long-term collaboration. I would like to express my gratitude also to Ing. Pavel Marton, Ph.D.; and Dr. Marek Paściak from IoF AS CR for our new collaboration on recently commenced project of the Czech Science Foundation.

I thank my Bachelor, Master, and Ph.D. students: Mgr. Kristina Vlášková, Ph.D.; Mgr. Daniel Staško; Bc. Jiří Zelenka; Bc. Filip Hájek; Denisa Vojtasová; and Balázs Szalai who substantially contributed to our work and helped to establish new scientific topic on the ground of the Charles University.

My work has been supported by the Czech Science Foundation as well as Czech Research Infrastructures: Institut Laue-Langevin - participation of the Czech Republic (ILL-CZ) and Materials Growth and Measurement Laboratory (MGML); and Czech Ministry of Education, Youth and Sports through Project MATFUN and MOBILITY fund. I appreciate these segments of support.

Finally, I wish to thank my entire family for their endless support in my work.

.....

RNDr. Milan Klicpera, Ph.D.

Contents

1. Introduction and state of art ¶

The present work is an overview of the original results attained by the author with a primary focus on rare-earth geometrically frustrated systems. In the course of the author's six-year work, the scientific topic was established at the home institution by securing all: (i) synthesis methods and routes for preparation of world-quality (large and stoichiometric) powder and mainly single-crystalline samples; (ii) ways to investigate their structural, phase, and bulk properties; (iii) access to the large-scale facilities to study their microscopic properties - local structures, magnetic structures, lattice and magnetic excitations (dozens of experiments in last five years); and (iv) collaborations with colleagues in the Czech Republic and abroad contributing to the field by both experiment and theory, resulting in joint studies. Each point had represented a non-trivial task and significant effort had been dedicated to each of them. Sample synthesis of $A_2B_2O_7$ (A = rare-earth element, B = d- or p-electron element) oxides had never been done at the Department of Condensed Matter Physics (DCMP) and Charles University. Simultaneously, there had been no experience with the investigation of these materials and frustrated oxide systems' physics in general.

The author commenced the work on the below-described systems after setting up at the DCMP arriving from his post-doctoral stay at the Institute Laue-Langevin, Grenoble, France, in 2017. He changed his main focus of interest, previously being the physics of rare-earth intermetallics, and began building a group concentrating on systems with geometrically frustrated lattices and strong spin-orbit coupling; also in the course of his Czech Science Foundation project. The new scientific direction attracted several colleagues from abroad joining the DCMP, as well as bachelor, master and Ph.D. students. At present, the frustrated magnetism group at the DCMP, previously non-existent, is the largest of the department groups.

The submitted habilitation thesis illustrates the exciting route of the author and collaborators to attaining experience and expertise with synthesis, characterisation, macroscopic and microscopic investigations, and interpretations of intriguing properties of two selected families of frustrated rare-earth oxides $A_2Ir_2O_7$ and $A_2Zr_2O_7$. Although other frustrated systems have also been studied at the DCMP, e.g., $NaCdB_2F_7$ with B = 3d-element, or $AMgAl_{11}O_{19}$, the author focusses only on the $A_2B_2O_7$ family of compounds in this thesis; as it is being the most investigated series so far and to maintain a reasonable consistency and length of the thesis.

The thesis is organised into seven chapters. The first chapter introduces the geometrically frustrated systems and related physics, as well as $A_2B_2O_7$ oxides and their characteristics. It explains why these materials are interesting from the fundamental research viewpoint and potentially important for applications. The second chapter focusses on the synthesis of these materials, specifically the preparation of $A_2Ir_2O_7$ and $A_2Zr_2O_7$ poly- and single crystals. Chapter 3 represents a

preview to our results on rare-earth pyrochlore iridate oxides, including macroscopic and microscopic data measurements and their interpretation, as well as respective models. Chapter 4 is dedicated to our investigations of the zirconium family, namely its bulk properties and average and local structures, depending on rare-earth or Ti-Zr substitutions. The results are summarised in chapter 5, together with the prospects of our work. Chapter 6 is formed by the list of author's publications related to the thesis' subject with indicated author's contribution to individual publications, and linked with respective sections of the thesis. These published manuscripts are attached to the thesis in chronological order in chapter 7.

1.1 Geometrically frustrated systems ¶

The Nobel Prize in Physics for the year 2021 was awarded "*For groundbreaking contributions to our understanding of complex physical systems*" from the largest scales, such as Earth's climate, down to the microscopic structure and dynamics of frustrated materials [1]. A proper understanding of the complexity of physical systems in their broadest sense, from microscopic to macroscopic properties, is essential for correct comprehension of their behaviour and prospective usage in technical applications.

The concept of frustrated magnetism is defined by the inability of all magnetic interactions to be simultaneously satisfied in a specific material. Frustrated materials have been profoundly studied since the 1950s, when the systems with antiferromagnetically coupled Ising moments on the triangular lattice revealed a different behaviour from isostructural ferromagnets or bi-partite antiferromagnets [2]. Since then, frustrated magnetic systems have attracted an ongoing attention of the scientific community due to the variety of competing magnetic ground states. Systems with 3d metals have been intensively studied (numerous publications). Systems with heavier magnetic elements were studied less intensively in the past. Nowadays, these systems attract well-deserved attention also due to strong spin-orbit coupling (SOC), which may imply strong anisotropy of magnetic interactions, and reinforcing the magnetic frustration (e.g. [3, 4]). Some materials are magnetically ordered at low temperature, but there are also magnetically disordered/frustrated ground states down to the lowest temperature. Among others, we highlight the classical spin liquid, quantum spin liquid, spin ice, and spin glass states [5, 6, 7, 8]. For example, the spin-ice state, the arrangement of magnetic moments analogous to the bonds in water ice [6], can host magnetic monopole-like states and Dirac strings. The quantum spin liquid state, defined by the entanglement of spins without any long-range magnetic ordering down to zero temperature, is proposed to host fractionalised Majorana-fermion quasiparticle excitations [9, 10]. Both are highly relevant for (topological) quantum computating applications.

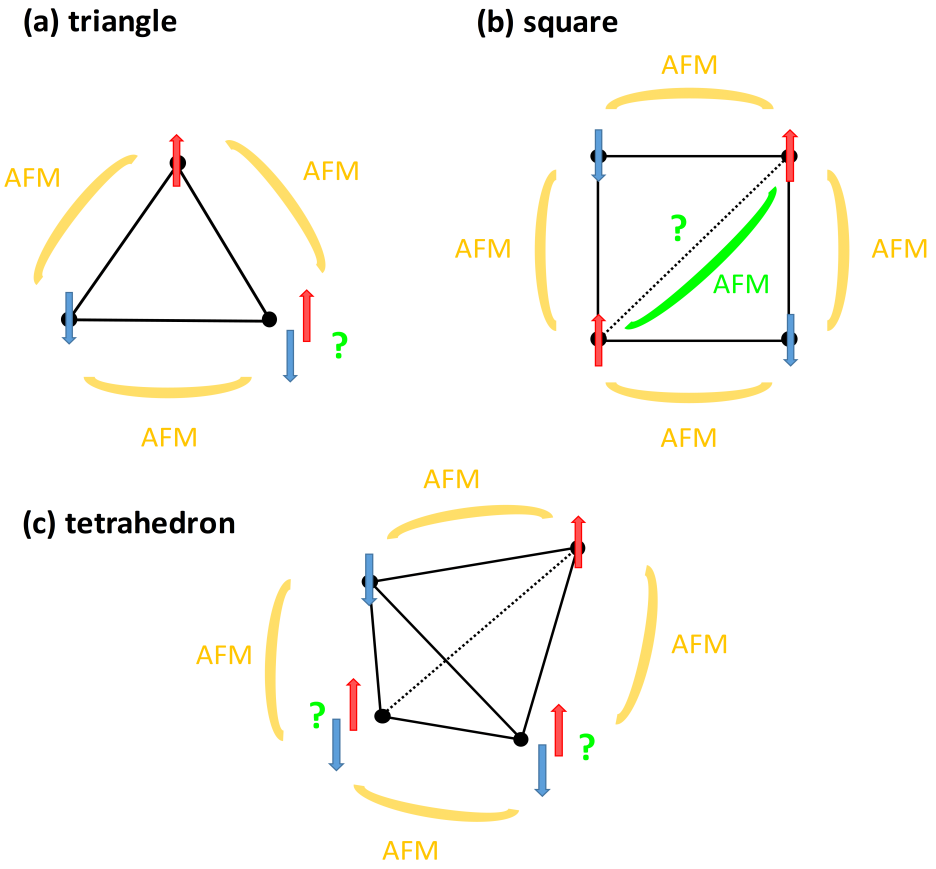

Figure 1.1: Geometrical frustration introduced on examples of triangle (a), square (b), and tetrahedron (c); antiferromagnetic interactions between Ising moments are schematically shown.

The frustrated magnetism is tightly bound to the geometrically frustrated crystallographic lattices. Among a variety of geometrically frustrated and quasi-frustrated lattices, we mention the most important ones: triangular, square, hyper-kagomé, and pyrochlore lattices. For illustration see Fig. 1.1.

The equilateral triangular lattice with vertices occupied with magnetic ions and Ising magnetic moments governed by antiferromagnetic correlations represents a simple 2D frustrated lattice. Two moments align antiparallel; however, the third moment cannot simultaneously satisfy the condition that it is antiparallel to both other moments. The lattice can be formed by edge-sharing triangles or corner-sharing triangles, the so-called kagomé lattice. The triangular lattice consists of well-separated layers of triangles. Considering only nearest-neighbour antiferromagnetic interactions, the lattice harbours the so-called 120-degree phase as the magnetic ground state [11]. Importantly, exciting the moments by an applied magnetic field could lead to a variety of induced magnetic phases, including the so-called $\frac{1}{3}$-magnetisation plateau or the umbrella phase [12]. Recent theoretical studies predict that anisotropic interactions among spins could lead to quantum spin-liquid phases [13, 14]. The kagomé lattice with corner-sharing triangles could also harbour many complex states, including superconductivity and

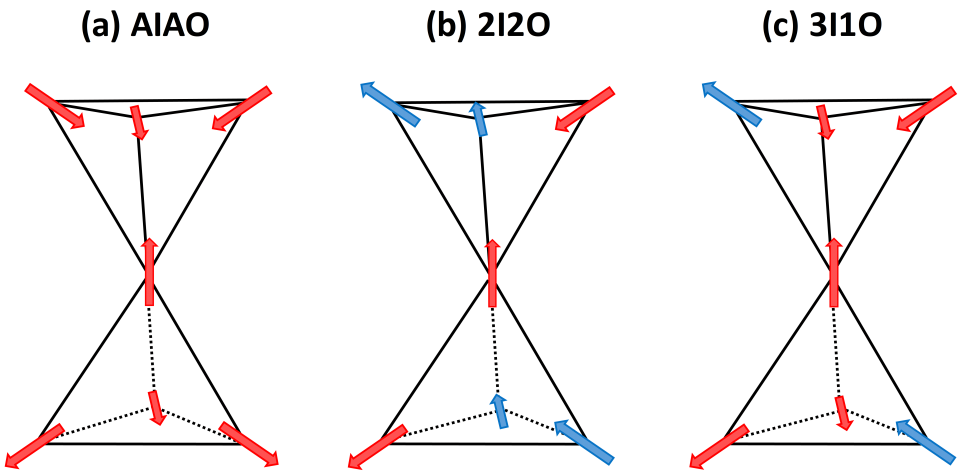

Figure 1.2: Selected types of arrangement of magnetic moments on the pyrochlore lattice. Two tetrahedra with Ising moments along local [111] directions are shown. All-in-all-out (AIAO) structure (a); two-in-two-out (2I2O) structure (b); and three-in-one-out (3I1O) structure (c) are depicted.

charge-density-wave order [15, 16, 17], or chiral magnetic order [18, 19, 20].

Frustration of magnetic moments on the square lattice origins in two non-equal antiferromagnetic pathways between nearest- (along the edge of the square) and next-nearest neighbours (along square diagonal) and the competition of interactions. The ground state of the material is dictated by dominating interaction; that is, Néel antiferromagnetic order for dominant nearest-neighbour coupling and columnar order for prevailing next-nearest-neighbour interaction. Recently, experimental studies showed a long-predicted quantum spin-liquid state in spin-$\frac{1}{2}$ Heisenberg square-lattice antiferromagnets on the border between the Néel and columnar phases [21, 22, 23].

Considering the 3D systems, canonical examples of frustrated lattices are the pyrochlore and hyperkagomé lattices. A hyperkagomé lattice is formed by corner-sharing triangles, similar to the 2D kagomé lattice; however, not in the plane, but in the space. The antiferromagnetic interactions among magnetic moments on the hyperkagomé lattice lead to 3D magnetic frustration. A quantum spin-liquid state has been recently reported in several materials that adopt this structure [24, 25]. Moreover, first steps to study and realise spin-orbit driven quantum phenomena have been taken in a few systems [26].

The pyrochlore lattice is formed by corner-sharing tetrahedra and is described in detail in section 1.2 of this thesis. When the lattice is adopted by magnetic ions, it can lead to the frustration of magnetic moments in both the isotropic Heisenberg antiferromagnet and the Ising limit. Antiferromagnetic interactions between Ising-like moments could result in a double degenerate ground state with four moments on the tetrahedron pointing all out or all in, the so-called all-in-all-out magnetic structure (AOAI) [27, 28]. See Fig. 1.2 for illustration.

Ferromagnetic interactions, on the other hand, lead to the ground state governed by the so-called ice rule [29]. In analogy with hydrogen and oxygen ions in water ice, two moments on the tetrahedron point in and two moments point out, that is, the two-in-two-out (2I2O) arrangement of moments [7, 30, 31]. The degeneracy of the ground state (6-times degenerate) is higher than in case of AIAO (2-times degenerate), as all combinations of 2I2O moments arrangement in the tetrahedron are enabled. The application of an external magnetic field can lift the degeneracy, resulting in magnetic ordering without symmetry-breaking (the first-order transition). Importantly, spin configurations tunnel between themselves through thermal or quantum fluctuations and form classical or quantum spin liquids [32]. Even the magnetic monopole-like state consisting of three moments pointing in and one moment pointing out of the tetrahedron, 3I1O configuration, can be induced and influenced by the external magnetic field [33].

1.2 $A_2B_2O_7$ oxides (A = rare-earth, B = d- or p-electron element) ¶

One of the most investigated geometrically frustrated systems, e.g., perovkites, spinels, volborthite, herbertsmithite, etc., is a broad family of the $A_2B_2O_7$ oxides (A = rare-earth element, B = d- or p-electron element). The complex physical properties of $A_2B_2O_7$ are determined not only by the geometrically frustrated lattice hosting A and/or B cations with nonzero magnetic moment, but also by mutual strengths and confluence of electron (Coulomb) correlations and spin-orbit coupling (SOC; playing a significant role especially in heavy B elements), as well as the crystal field acting on the cations. A delicate balance among interactions could generate, in addition to various conducting states, topologically non-trivial phases, e.g., the topological Mott insulator or topological band insulator, a Weyl semi-metal state, and Fermi arc surface states [34, 35, 36, 37]. See Fig. 1.3 for an illustration. Depending on the magnetic A and B elements, the exchange interactions and the f-d exchange could lead to, e.g., anisotropy-tuned magnetic order and properties [7, 38] or giant magnetoresistance [39].

Geometric frustration and competing spin interactions can also cause the freezing of spins leading to spin-glass, or even spin-liquid states [5]. The term spin liquid state is used for the system with distinct dynamics of (highly) correlated non-ordered spins fluctuating down to the lowest temperature. The so-called spin-ice state, representing the arrangement of magnetic moments on the lattice analogous to the bonds in water ice [6], can host magnetic monopole-like states and Dirac strings. That is, two moments point in (short bonds in water ice) and two moments point out (longer bonds in water ice) of the pyrochlore tetrahedron (Fig. 1.2b). By exciting the spin-ice, the moments' arrangement changes into three moments pointing in and one moment pointing out of tetrahedron (3I1O

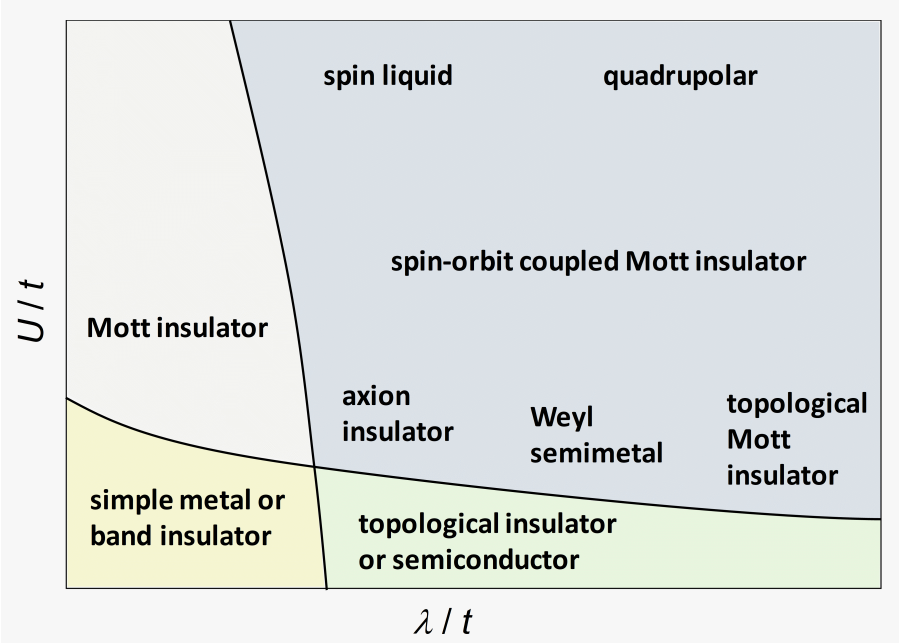

Figure 1.3: Schematic diagram of electronic states varying relative strength of spin-orbit coupling λ and electron-electron (Coulomb) correlations U normalised to the kinetic energy hopping t. The figure is adopted from and fully interpreted in Ref. [34].

arrangement, or analogously 1I3O arrangement; Fig. 1.2c). The tetrahedron can be therefore viewed as a superposition of four moments with single moment direction, that is, magnetic monopole-like state.

Furthermore, a fragmentation of the ground state, that is, a simultaneous antiferromagnetic AIAO order and a Coulomb phase spin-liquid or spin-ice, was proposed for several members of the series [7, 30]. Very recent studies evidenced a coupling between magnetic monopole-like states on the A sublattice and antiferromagnetic domains and domain walls of the B sublattice [33], paving the way for the design of next-generation spintronic devices.

1.2.1 Crystal structures

The $A_2B_2O_7$ oxides were repeatedly reported crystallising in two cubic variants: pyrochlore $Fd\bar{3}m$ (space group n. 227) and defect-fluorite $Fm\bar{3}m$ (space group n. 225), or orthorhombic $Pnma$ (space group n. 62) structure [40]. Focussing further on the cubic variants; defect-fluorite lattice is a disordered lattice with A and B cations sharing single Wyckoff position (4a; frustrated fcc sublattice of cations) and oxygen anions forming cubes around the A/B cations (8c position; occupied by 7 oxygen anions). See Fig. 1.4 for illustration. The pyrochlore lattice, on the other hand, is a fully ordered lattice. A and B cations (16d and 16c sites) individually form 3D networks of interpenetrating corner sharing tetrahedra, providing the crystallographic basis for 3D frustrated magnetism (see also Fig. 1.2). Projecting the A and B layers along the cubic [111] direction, the

pyrochlore structure can be looked upon a system with alternating kagomé and triangular layers. Oxygen anions reside in two Wyckoff positions (8b and 48f), forming 8- and 6-coordinate cages around A and B cations, respectively.

The differences and interconversion from pyrochlore to defect-fluorite structure can be viewed from different perspectives: The cations that reside at two crystallographically distinct sites of the pyrochlore structure (Wyckoff sites 16d and 16c) become disordered, occupying a single site in the defect-fluorite structure (4a). See Fig. 1.4 to visualise the crystallographic sites. Oxygen anions occupying the 48f site (coordinates: x_{48f}, $\frac{1}{8}$, $\frac{1}{8}$) of the pyrochlore lattice shift to a higher symmetry position in the defect-fluorite lattice (8c with ($\frac{1}{4}$, $\frac{1}{4}$, $\frac{1}{4}$) coordinate); the oxygen anions located at two crystallographically distinct sites (48f and 8b) and ordered oxygen vacancy at the virtual-Wyckoff site 8a of the pyrochlore structure disorder onto a single $\frac{7}{8}$-occupied 8c site of the defect-fluorite structure. The translational shift of the 48f oxygen to the higher symmetry tetrahedral void changes the cation coordination geometry from being eight-coordinate and six-coordinate for the A and B sites, respectively, in the pyrochlore structure to an average seven-coordinate for both A and B in the defect-fluorite structure. Both pyrochlore and defect-fluorite lattices are frustrated lattices; however, different exchange pathway types and thus different magnetic exchanges are realised. Moreover, the defects of the fluorite lattice influence the oxidation number dramatically; a vacancy can lead to a change of the oxidation number of a part of the cations, which strongly influences the metallic/insulating and magnetic properties of the material, e.g., [41, 42].

The reported long-range ordered crystal structure of the rare-earth $A_2B_2O_7$ oxides is strongly dependent on the size ratio between A and B cations (r_A/r_B). Demonstrating the dependence on zirconates $A_2Zr_2O_7$, they exhibit a cubic pyrochlore structure at room temperature and pressure when the ratio is within the range $1.48 < r_A/r_{Zr} < 1.63$, that is, for A = La - Gd. $A_2Zr_2O_7$ with $r_A/r_{Zr} \leq 1.47$, that is, for A = Tb - Lu, the defect-fluorite structure was observed/postulated. However, the true nature of the disordered defect-fluorite structure in several $A_2B_2O_7$ oxides has recently attracted attention due to the discordance between the local environment (total scattering, pair-distribution function (PDF)) and space-averaged (Rietveld) analysis of the diffraction data, e.g., $Ho_2Zr_2O_7$ [43]. Analysis of diffraction data across different length scales shows that the average cubic defect-fluorite structure is locally comprised of short-range presumably orthorhombic structural units. Both local and long-range structural considerations are important to understand the magnetic and electronic properties of $A_2B_2O_7$ oxides. Indeed, a recent investigation [44] on the synthesis-dependent disorder in nominal defect-fluorite $Tb_2Hf_2O_7$ has promoted interesting physics with the observation of both Coulomb phase and spin-glass behaviour! Despite a high density of structural disorder, the correlated phase is governed by the local structure rules of pyrochlore, with the hallmark power-law correlations [44]. Furthermore, our recent total neutron scattering (PDF) experiments showed that the local struc-

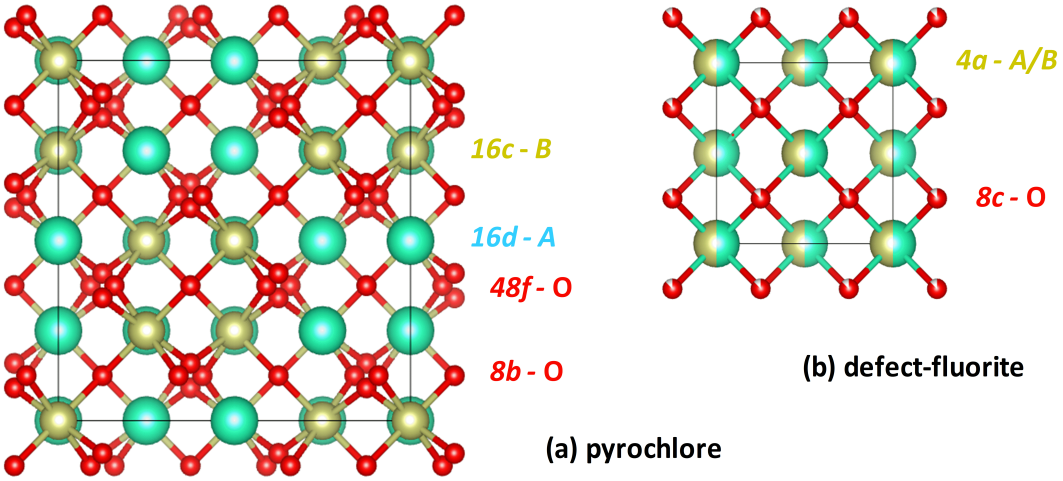

Figure 1.4: Unit cells of cubic pyrochlore (a) and defect-fluorite structure (b). The 8c position of the defect-fluorite structure is occupied by oxygen from $\frac{7}{8}$.

ture of the heavy $A_2Zr_2O_7$ cannot be adequately described by the defect-fluorite model (see chapter 4, section 4.2). Instead, a model consisting of lower-symmetry structural units describes the experimental data well [45]. Future detailed structural studies of $A_2Hf_2O_7$ series are also highly desirable, as this series is prone to show qualitatively the same local structural correlations in average defect-fluorite members. Moreover, the synthesis method and subsequent thermal treatment of the samples can play a significant role in formation of global and local structure; and they represent another research direction (tuning the material properties for applications).

The inherent disorder and reduced geometrical frustration of the defect-fluorite lattice (compared to the pyrochlore lattice) meant that the low-temperature electronic and magnetic properties of the respective $A_2B_2O_7$ have been significantly overlooked. However, instead of a sharp (space-average) border between the two structural types, a smooth and continuous increase in (local) disorder should be considered in the $A_2B_2O_7$ family; that is, unconventional pyrochlore-like correlated electron physics could be present in a nominal defect-fluorite lattice. More generally, only a proper determination of the crystal structure and local structure allows a correct explanation of the frequently complex and exotic states observed in $A_2B_2O_7$ and generally in any material. Here, we also highlight possible technical applications of defect-fluorite materials, namely, $A_2Zr_2O_7$. These materials are suitable for use in solid oxide fuel cells due to their high ionic conductivity [46, 47, 48, 49], as well as thermal barrier coatings [50], or as nuclear waste storage elements [51]. To be utilised for these applications, a complete picture of structural stability, defect energies, and transformation behaviour in various environments is necessary; particularly for accurate modelling and prediction of ionic conductivity pathways and activity, as well as for the determination of crystal-structure - conductivity relationships.

1.2.2 Electronic properties

In addition to the structure stability and geometrical frustration, the magnetic and electronic properties of the material are strongly influenced/dictated by microscopic interactions. Electron correlations and spin-orbit coupling (SOC); that is, interactions among individual atoms (their moments), and interactions between electron spin and orbital angular momentum in the ion, respectively; represent basic mechanisms staying behind a variety of physical phenomena. Relativistic SOC is considered a small perturbation to the overall properties of light elements, but becomes rapidly stronger with increasing atomic number of the element. Such a trend is well demonstrated in the d-elements. Only weak SOC perturbations are present in compounds with lighter 3d elements, while for the heavier 4d and 5d elements SOC starts to play a significant role in their electronic properties and magnetic ground state formation. Simultaneously, the d-orbitals become more extended with increasing atomic number, leading to a reduction of the electronic repulsion and thus to a weakening of the electron correlation effects. Consequently, both the SOC and electron correlations are expected to have a similar strength in heavy elements (especially 5d elements), which leads to a spectrum of complex physical phenomena: Weyl semimetal [35], topological Mott insulator [37], axion insulator [52], spin-ice with monopole-like excitations [6], or spin-liquid states [5]. See Figs. 1.2 and 1.3. A strong SOC is, moreover, a prerequisite for the spin Hall effect (SHE) and the inverse SHE; that is, the control of a spin current in a material via a charge current and vice versa [53]. Crystallographic families with adequate symmetry conditions and a sizeable correlated SOC regime, hosting these phenomena, have been proposed, among them the pseudo-cubic and planar perovskites [54, 55], spinel-related structures [56] and $A_2B_2O_7$ pyrochlores.

Focussing further on the system relevant from the viewpoint of the present thesis; $A_2Ir_2O_7$ iridates crystallise in pyrochlore type of cubic structure on global and locale scales, as was very recently demonstrated also by our neutron diffraction (ND) and pair-distribution function (xPDF and nPDF) studies. Geometrically frustrated lattice and SOC and electron correlations in $A_2Ir_2O_7$ provide a ground for a variety of complex conductive and magnetic properties (as discussed in the previous paragraph). Furthermore, the rare-earth (with magnetic A^{3+} cation) and Ir^{4+} cations/sublattices impact each other through f-d exchange, leading to, e.g., fragmented magnetic states [7, 30], Ir-magnetic-ordering induced A sublattice ordering (anisotropy-tuned magnetic order) [28], or phase competition between Ir-induced ordering and A-A exchange interactions [27]. On the other hand, according to (our, see section 3.1.3) studies, the transition temperature (T_{Ir}) and ordering of the Ir sublattice are negligibly influenced by the A sublattice, at least at high temperature [57], and depend primarily on the A cation size; see Fig. 1.5. Such smooth behaviour, mostly irrespective of the particular magnetic and electronic properties of the A-site, has been attributed to the wide

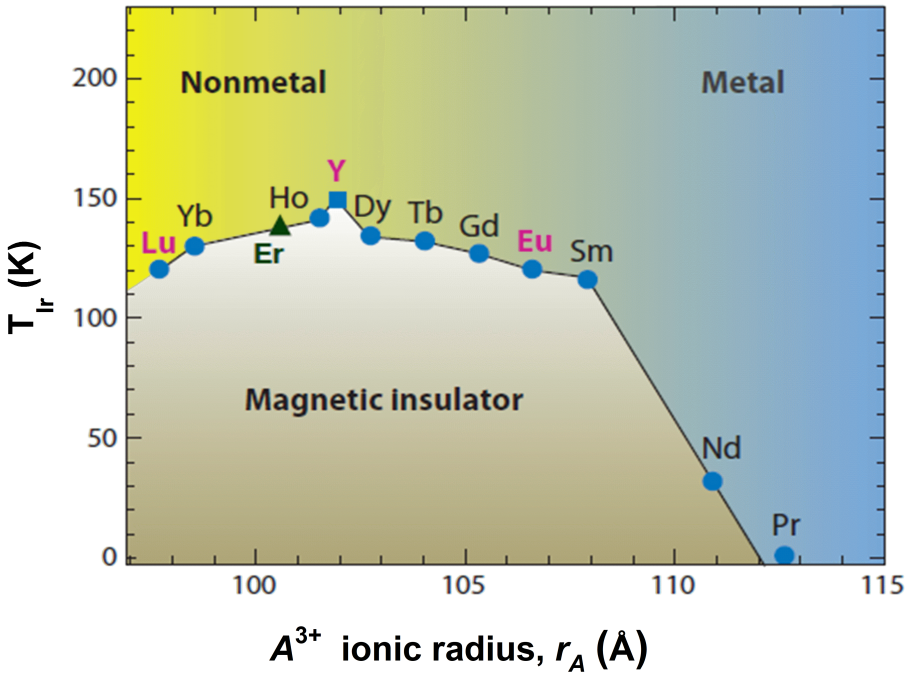

Figure 1.5: Phase diagram of $A_2Ir_2O_7$ compounds - development of the transition temperature of the magnetic ordering of the Ir sublattice T_{Ir} with the ionic radius of rare-earth element A^{3+}. Metal/nonmetal to insulator transition (MIT) coincides with magnetic transition and is indicated as well. The diagram is adopted from Ref. [60].

t_{2g}-block bandwidth of iridium, resulting in strong 5d-orbital overlap with oxygen ligand 2p-orbitals, and a strong sensitivity to structural changes (Ir-O-Ir bond angle variation) associated with the lattice contraction [58]. That is, an application of chemical pressure, and more apparently hydrostatic and uniaxial pressure is bound to impact bond angles and lengths, and in turn, magnetic and electronic properties of specific $A_2Ir_2O_7$ members [59].

The magnetic ordering of the Ir sublattice has been reported/proposed to be all-in-all-out (AIAO) ordering (see Fig. 1.2a) in $A_2Ir_2O_7$, except A = Pr member. The studies were based primarily on the powder neutron diffraction experiments [27, 28], which are harshly limited by a small magnetic moment (estimated $< 0.5\ \mu_{\mathrm{B}}$) and high neutron absorption cross-section of Ir. Although the scientific community mostly accepted the AIAO structure of Ir, no or only rather ambiguous signs of magnetic signal were observed for several members, e.g., [61] or our recent ND study on newly synthesised A = Tm member (section 3.1, Ref. [62]). Importantly, applying a magnetic field along <001> (<111>) direction has been expected/evidenced to overcome the exchange interactions, and turn two (three) magnetic moments (in AIAO tetrahedra) point in and the other two (one) point out, forming the 2I2O (3I1O) configuration [63] (Fig. 1.2). That is, spin-ice and magnetic monopole-like states can be induced by applied magnetic field.

Concomitantly with magnetic ordering of the Ir sublattice, below T_{Ir}, $A_2\mathrm{Ir}_2\mathrm{O}_7$ undergo a transition from metal/semi-metal/semiconducting to an insulating state (MIT) [35, 57]. See Figs. 1.3 and 1.5. Again, the transition is strongly influenced by the A or Ir substitutions and the application of external pressure [64, 65]; mainly due to the tuning of Ir-O-Ir bond lengths and angles, which modulates the valence-electron bandwidth and therefore the effective correlation strength. Recently, a strong electron-phonon interaction was evidenced in $A = \mathrm{Eu}$ member [66]; that is, the Ir-O-Ir bond bending vibration is strongly coupled to a continuum composed of spin, charge, and orbital excitations via a confluence of all three mechanisms. Furthermore, the electronic/conducting properties have been postulated to be significantly different in the domain walls, boundaries between AIAO and AOAI domains: The AIAO magnetic insulator is considered to have the magnetic order tied to its insulating property. Therefore, as the magnetic order is disturbed in the domain walls, the conducting properties are influenced as well [33, 63, 67], opening new opportunities to study topological conductive states. See chapter 3 and mainly section 3.1 for details and proposed mechanisms staying behind these properties.

2. Synthesis of rare-earth $A_2B_2O_7$ compounds ¶

Introduction to publications: **1., 2., 6., 7., 9., 13., 15., 16., and 17.**

A significant attention has been dedicated to $A_2B_2O_7$ oxides in recent years; where A stands for a rare-earth element and B is a p- or d- element. Numerous studies have reported mechanical and physical properties of many members of this broad family (see section 1.2). However, many previous studies were severely limited by the quality of investigated samples and lack of single crystals, especially in case of B = Mn, Ir, Pt, or Pb members. Numerous attempts have been performed to synthesise good-quality, and importantly, stoichiometric samples:

Polycrystalline samples from the $A_2B_2O_7$ family are frequently prepared by standard solid state reaction of constituent elements and/or oxides [68], while single crystals of these materials are grown using hot-floating-zone technique either from polycrystalline precursor [69] or a mixture of initial materials [70, 71, 72]. Many $A_2B_2O_7$ melt congruently [73], enabling a synthesis of large single crystals. However, high reaction and/or melting temperature of some A and B elements or oxides could complicate the growth, bringing considerable requirements on the laboratory instrumentation. E.g., ZrO_2, frequently used as an initial oxide for synthesis of $A_2Zr_2O_7$ zirconates, has a very high melting temperature of 2715 °C and is chemically stable on heating [74]. Therefore, synthesising $A_2Zr_2O_7$ materials via direct melting of initial reactants requires heating power and capacities of preparation furnace going beyond standard capabilities of laboratory kilns [71]. Nevertheless, also melt-free methods can be utilized for synthesis of these compounds, including co-precipitation reaction and sol-gel method [75]. The growth of other $A_2B_2O_7$ must be stabilised by various chemicals to enable a growth of desired compositions [76].

Another difficulty arises from the low vapour pressure of some constituent elements and oxides, preventing the synthesis under ambient conditions. The application of high pressure in a closed reaction vessel is required to produce a polycrystalline $A_2B_2O_7$ samples with B standing for Pb [77], Pt [78], V [79] or Mn [80]. Hydrothermal synthesis method, where the reaction vessel contains an aqueous solution of starting materials and mineralizing agent (e.g. KOH), also enables crystallisation of some $A_2B_2O_7$ at lower temperature [81]. To prevent evaporation of material or its components from initial mixture a proper dissolvent/flux, e.g. KF or CsCl [61, 76], can be used as well.

Establishing a successful preparation route applicable to a specific material is a non-trivial task and requires considerable experience and experimental effort. In this chapter, we focus on the preparation of rare-earth $A_2Ir_2O_7$ iridates and $A_2Zr_2O_7$ zirconates in polycrystalline and single crystalline form. Sever-

al methods were employed: the solid-state reaction of stoichiometric and non-stoichiometric mixtures of oxides, synthesis from flux using CsCl, KF and PbF_2 as a solvent, hydrothermal synthesis employing various solvents, hot-floating-zone method, and Czochralski method of growth. Synthesised samples were characterised employing powder and Laue X-ray diffraction, electron microscopy, and in many cases powder and Laue neutron diffraction, mapping their overall quality, phase purity, and homogeneity.

2.1 Preparation of polycrystalline $A_2Ir_2O_7$ ¶

Introduction to publications: **2., 7., 9., and 16.**

Polycrystalline $A_2Ir_2O_7$ compounds have been synthesised from initial A_2O_3 and IrO_2 oxides employing three methods introduced in the following text. High purity constituent oxides (99.99% metal basis, AlfaAesar) were individually heated up to 200 °C to remove the water, weighted, and thoroughly mixed in the desired ratio. Reacted samples were investigated by means of powder X-ray diffraction and electron microscopy after each synthesis process cycle. Powder diffraction patterns were collected using a Bruker D8 Advance diffractometer and Cu K_α radiation. The patterns were analysed employing the Rietveld method and the FullProf package [82]. An electron microscope MIRA, Tescan with a back-scattered electron (BSE) detector and an energy dispersive X-ray (EDX) analyser were used to examine the stoichiometry and homogeneity of the prepared oxides, as well as the shape of prepared grains.

Selected good-quality samples were subsequently investigated employing a variety of experimental techniques ranging from standard laboratory magnetisation measurements through synchrotron radiation and neutron diffraction techniques to inelastic scattering experiments in large-scale facilities. See chapter 3 for experimental details and an overview on the most important results. Further experimental and technical details are presented in respective publications.

In this section, the synthesis of polycrystalline samples from the $A_2Ir_2O_7$ series is demonstrated on A = Er member. The systematic mapping of the preparation of $Er_2Ir_2O_7$ compound enabled an optimisation of the entire synthesis process. The optimised route has been utilised to prepare other rare-earth members of the series. During last few years, $A_2Ir_2O_7$ compounds with A = Pr, Nd, Sm, Dy, Ho, Er, Tm, Yb, and Lu have been synthesised and characterised in the home laboratory.

2.1.1 Solid-state reaction

The solid-state reaction is a sample preparation method standardly used to synthesise $A_2B_2O_7$ materials at a temperature significantly lower than the melting temperature of theirs or their respective precursor elements and oxides [68]. First,

a stoichiometric ratio of Er_2O_3 and IrO_2 oxides was reacted in a Pt crucible at elevated temperature. The reaction was carried out in air for 12 hours at temperatures ranging from 300 to 1200 °C. The reacted sample was ground and inspected by X-ray diffraction. Subsequently, the sample was reacted at a higher temperature and analysed again. Repeating this process, 10 diffraction patterns at 10 temperatures were collected; see Fig. 2.1.

Several important observations were accomplished on the basis of X-ray diffraction patterns of sample reacted at different temperatures:
(i) The decomposition of iridium oxide is traceable already at 300 °C. Already at such low temperature, elemental Ir patterns (space group $Fm\overline{3}m$) are identified.
(ii) The broadness of the IrO_2 peaks (space group $P4_2/mnm$) is explained by the grains size of powder reactant. The sharpening of the IrO_2 peaks is observed at higher temperature, and could be modelled by the Scherrer formula [83]. The crystallite size increases with increasing temperature, reaching 64(5) nm at 900 °C (comparable to grain size of Er_2O_3).
(iii) The mole fraction of iridium oxide decreases slightly, whilst no $Er_2Ir_2O_7$ phase is formed up to, at least, 600 °C. The loss of IrO_2 can be attributed to the known disproportionation and loss of volatile iridium oxides [84].
(iv) At 900 °C, the pyrochlore $Er_2Ir_2O_7$ phase is formed. The mole-fraction of this phase in the sample is 4.3(3)% after the 12-hour reaction time.
(v) A further increase in the reaction temperature causes a strong increase of the $Er_2Ir_2O_7$ fraction in the sample. The reaction is almost completed at 1100 °C, when the amount of both IrO_2 and Ir in the sample is only 2.3(5)% (Fig. 2.1).
(vi) Increasing the reaction temperature to 1200 °C, $Er_2Ir_2O_7$ phase decomposes. As the volatile iridium oxides evaporate, only Er_2O_3 diffraction patterns (space group $Ia\overline{3}$) are measured.

Such observations, together with knowledge of the high melting temperature and stability of Er_2O_3(s) (melting point 2344 °C [85]), give evidence of an equilibrium state between pyrochlore (ternary oxide) and precursory binary oxides, with continuous evaporation of volatile Ir oxides, even at 1000 °C. Finally, at 1200 °C the increasing evaporation of volatile iridium oxides, which are in equilibrium with $Er_2Ir_2O_7$(s) and Er_2O_3(s) causes the eventual complete conversion of $Er_2Ir_2O_7$(s) back into Er_2O_3(s) (and evaporated IrO_x(g)) to maintain the equilibrium condition. Alternatively, one can speculate about the possible evaporation of $Er_2Ir_2O_7$. However, such an explanation is ruled out by the weight of the final sample. The mass of the product reacted at 1200 °C was within an error of the mass of Er_2O_3(s) in the initial mixture.

Utilising the acquired experience, we attempted to optimise the synthesis process. Excess IrO_2 was added to the content and the non-stoichiometric mixture was reacted at 1000 °C. At this temperature, the $Er_2Ir_2O_7$ phase is formed and its decomposition is reasonably low. A mixture of IrO_2 and Er_2O_3 in the 2.1:0.9 ratio was repeatedly ground and reacted for 12 hours in air. The X-ray diffraction patterns were collected after each reaction cycle. The pyrochlore phase was

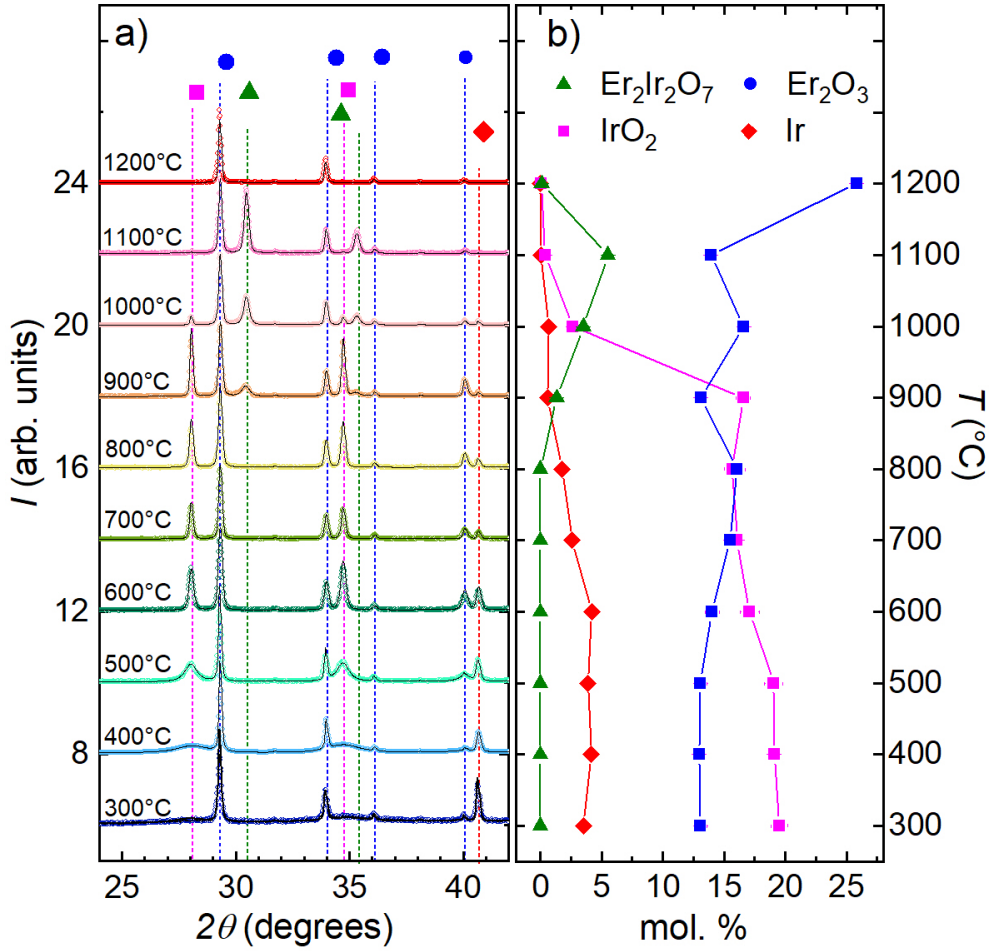

Figure 2.1: Powder X-ray diffraction patterns recorded on the $Er_2Ir_2O_7$ mixture prepared by a solid-state synthesis (a). The pattern consists of several contributions: prepared compound $Er_2Ir_2O_7$, initial oxides Er_2O_3 and IrO_2, and pure Ir metal. The most pronounced peaks are marked to illustrate respective phases. The molar concentration of individual phases dependent on the reaction temperature is also shown (b). The figure is adopted from Ref. [86].

already formed during the first cycle with 25(3) mol.%. Besides the formation of the pyrochlore phase, as previously observed, a partial decomposition of IrO_2 was followed in the diffraction patterns. Further thermal cycling led to an increase in the mole fraction of $Er_2Ir_2O_7$, and further decomposition and reduction of IrO_2. By cycle 6, almost all the IrO_2 oxide was reacted/decomposed, and the $Er_2Ir_2O_7$ fraction was maximal (48.2(7) mol.%). Additional thermal cycles did not improve the sample, but instead a decomposition of the previously prepared $Er_2Ir_2O_7$ was evidenced by the relative increase of the Er_2O_3 fraction in the sample.

The results of solid-state synthesis, both through the use of stoichiometric and non-stoichiometric starting mixtures, suggest that phase pure $Er_2Ir_2O_7$ pyrochlore cannot be acquired by this method. An additional excess of IrO_2 in the initial mixture, fine control of reaction temperature and time, careful analysis of the reacted sample, all significantly improved the quality of the final material. However, a decomposition of IrO_2 cannot be prevented, and the Ir product

(although very minor) remains stable up to the temperature at which $Er_2Ir_2O_7$ decomposes. The combination of an off-stoichiometric mixture solid-state reaction and other techniques may be considered.

2.1.2 Hydrothermal synthesis

Simultaneously with attempts to synthesise $Er_2Ir_2O_7$ by solid-state reaction, the endeavours to prepare it by means of lower-temperature hydrothermal synthesis were performed. Hydrothermal synthesis is the preparation method, when a mixture of initial oxides is closed within a hermetically sealed reaction vessel, together with an aqueous mineralisation agent(s), and thermally treated. A standard polytetraflourethylene (PTFE) liner was filled in a stainless steel autoclave reactor (Parr Instrument Deutschland) and heated in a laboratory oven. The maximum available reaction temperature is limited by the softening temperature of PTFE (220 °C). As the autoclave isolates the mixture from the outer environment, no loss of constituent elements is expected, compared to the open reaction vessel used for the synthesis employing a solid-state reaction. The increased temperature and pressure in the aqueous environment are expected to increase the mobility of the ions and aid the reaction and recrystallisation of a mixture/compound. According to the dimensions of the reactor and the inner content of 23 and 45 ml, the autogenous pressure was estimated to vary between 1 and 3 MPa [87], depending on the exact volumes of individual reactants and solution.

A stoichiometric mixture of initial oxides in individual mineralising agents was reacted at a maximum autoclave reactor temperature of 220 °C for 12 days. Although we tested a variety of mineralising agents and a significant amount of time was dedicated to fully uncover the potential of hydrothermal synthesis in the preparation of $Er_2Ir_2O_7$, the results do not indicate any direct path to the preparation of a single $Er_2Ir_2O_7$ phase.

The first attempt at sample preparation was realised using the distilled water without any additional mineralising agents. The resulting product did not show any traces of the pyrochlore phase, constituting oxides were present and 16(2) mol.% of the additional $Er(OH)_3$ phase was formed. Second, potassium and sodium hydroxides, KOH and NaOH, which are traditional basic mineralising agents, were used. The aqueous solution of the hydroxides was prepared with concentrations 1, 4 and 12 M and introduced into the reaction vessel. In addition to the mixture of initial oxides, also attempts with a prereacted precursor with about 50(2) mol.% were performed. Investigating the X-ray diffraction patterns of the reaction products revealed no improvement of the $Er_2Ir_2O_7$ phase content. Moreover, the presence of $Er(OH)_3$ as an unwanted side product was detected. Its amount increased from 50(2), to 54(2) and finally 56(3) mol.% for 1, 4 and 12 M of KOH, respectively. The situation was similar in the case of NaOH, where no increase of the pyrochlore phase was detected in any of the NaOH concentrations.

The amount of side product $Er(OH)_3$ was determined to be similar to that in the case of KOH.

Third, hydrothermal synthesis was attempted using inorganic salt solutions as the mineralising agent, trialling caesium chloride (CsCl), sodium fluoride (NaF), and potassium fluoride (KF). The CsCl and NaF agents allowed an increase of the pyrochlore phase by up to 8(2)% with respect to the original phase composition. The KF agent had a more promising impact, with a 25(4)% increase in pyrochlore phase content. Finally, we attempted the reaction employing inorganic acids HNO_3 and HCl as mineralising agents in aqueous solutions 1, 2 and 4 M with prereacted precursor. A slight improvement of up to 10(2)% of the pyrochlore content with respect to the precursor phase mixture was observed in the case of HNO_3. A smaller impact of HCl was revealed, with the resulting increase in the pyrochlore phase content by 7(2)%.

The initial results achieved by using the aqueous solutions of fluoride salt and inorganic acids as mineralising agents suggested a promise for hydrothermal synthesis. However, additional reaction cycles did not lead to any significant reinforcement of the $Er_2Ir_2O_7$ phase; additional modifications or repeating reaction cycles did not provide a route to a sufficiently pure sample.

2.1.3 Flux method

Rather negative results employing the solid-state reaction and hydrothermal synthesis of the initial Er_2O_3 and IrO_2 oxides in stoichiometric and off-stoichiometric initial and pre-reacted mixtures motivated us to search for other preparation methods. That is, the flux method of synthesis has been employed using an inorganic salt CsCl as a solvent [61, 76]. The flux mediates the formation of the pyrochlore phase and importantly protects the initial/reacted oxides from (heavy) evaporation. The oxides, (partially) dissolved in the flux, are expected to react and crystallise at a significantly lower temperature than in the case of a solid-state reaction.

To properly map the synthesis using the flux method, we started again with a stoichiometric mixture of Er_2O_3 and IrO_2 initial oxides. They were mixed with the CsCl flux in a 1:2:50 ratio, respectively. Similarly to solid-state synthesis, the mixture was placed in an open platinum crucible and reacted for 12 hours at a temperature ranging from 700 °C to 1000 °C. After each reaction cycle, the CsCl salt was cleared from the sample by dissolution in distilled water and the powder was collected by centrifuging.

Carefully mapping the sample synthesis, depending on the reaction temperature, resulted in several important observations:
(i) At 700 °C, large (approximately 1 mm) black shiny pieces were found in the mixture. The EDX analysis revealed no traces of erbium signal in these large crystals, and only Ir and O were detected. Indeed, single crystal X-ray diffraction confirmed that the crystal structure was tetragonal, with respective

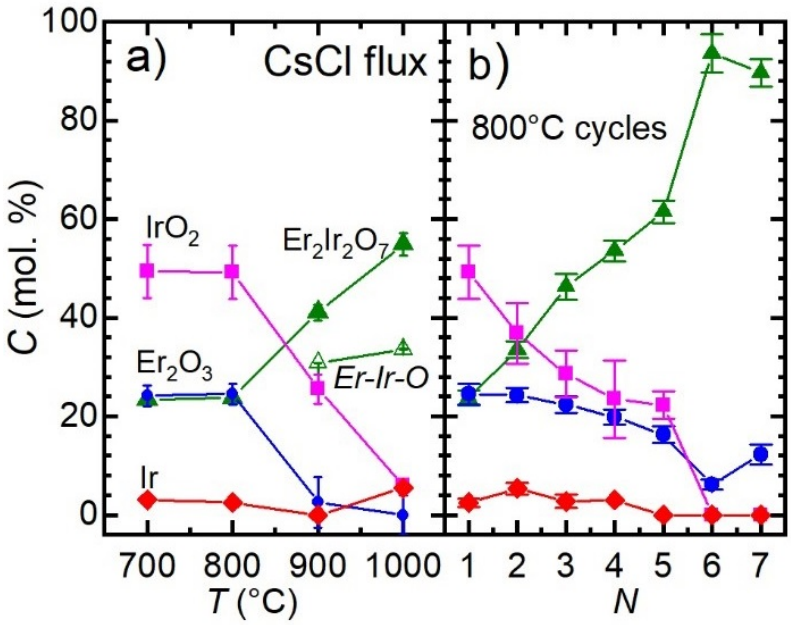

Figure 2.2: Concentration development in $Er_2Ir_2O_7$ sample synthesised using the CsCl flux method. Concentration dependencies on reaction temperature (a) and number of reaction cycles at 800 °C (b) are presented. The figure is adopted from Ref. [86].

lattice parameters corresponding to IrO_2 phase [86]. In order to unambiguously confirm that the synthesised single crystals are purely IrO_2, the mixture was divided into two parts depending on particle size (using a 40 μm sieve), and investigated by powder X-ray diffraction. The analysis showed a high amount of IrO_2 with good crystallinity in the courser part. The second part, being a finer powder, contained a significantly lower amount of iridium dioxide, and the diffraction patterns were dominated by $Er_2Ir_2O_7$ and Er_2O_3 contributions. A small amount of Ir (from the decomposition of IrO_2) was also observed.
(ii) The reaction cycle at 800 °C slightly improved the pyrochlore phase content in the sample, see Fig. 2.2. The ratio between the mole fraction of Er_2O_3 and IrO_2 remained unchanged with increasing temperature.
(iii) Further increase in the reaction temperature significantly reduced the amount of initial oxides. However, in addition to the single $Er_2Ir_2O_7$ phase, another cubic pyrochlore phase with slightly larger lattice parameter was observed. The flux growth at 900 °C provided better conditions for the formation of this secondary phase compared to lower temperatures. The amount of both the $Er_2Ir_2O_7$ phases reached 72(2) mol.%, while the secondary phase content was 31(2) mol.%. It further decreased to 13(2) mol.% when reacting the sample at 1000 °C, while the total amount of $Er_2Ir_2O_7$ phases reached 90(3) mol.%. The data quality does not allow refinement of site atomic occupations in this secondary phase; however, a rough estimate of the stoichiometry can be obtained using Vegard′s law-type arguments for the $Er_{2+2x}Ir_{2-2x}O_{7-x}$ series. Using the lattice parameters of $Er_2Ir_2O_7$ and Er_2O_3 as series end-members, the estimated stoichiometry of the

Er-Ir-O secondary phase corresponds to an approximate formula $Er_{2.71}Ir_{1.29}O_{6.64}$.

To avoid formation of this off-stoichiometric pyrochlore phase, the new sample was reacted at 800 °C several times. Several heating and grinding cycles led to an improvement of the pyrochlore phase content without any traces of the secondary Er-Ir-O phase, as illustrated in Fig. 2.2. Finally, after six cycles, the pyrochlore phase content reached 94(3) mol.%. The shape of the pyrochlore peaks in X-ray diffraction patterns was also significantly improved in comparison to previous attempts. The amount of Er_2O_3 in the sample was reduced to 6(1) mol.%, and no IrO_2 or Ir were detected in the diffraction patterns. With further heating cycles, the pyrochlore phase content began to decrease, presumably due to the same mechanism seen in the high-temperature solid-state reaction: a process of decomposition of the pyrochlore into constituting oxides, with more volatile iridium oxides evaporating from the surface of the flux, leading to an apparent increase in the fraction of Er_2O_3.

Contrary to the solid-state reaction method, with careful control of reaction conditions, temperature and duration of reaction, number of cycles, and amount of initial oxides, the flux method allows a preparation of the $Er_2Ir_2O_7$ sample of good crystallinity. To compensate for any missing IrO_2 in the final product, it can be added into the account at the beginning of synthesis, or before any reaction cycle. Many other members of the $A_2Ir_2O_7$ series have been synthesised using the flux method: A = Pr, Nd, Sm, Dy, Ho, Er, Tm, Yb, and Lu. We highlight newly synthesised $Tm_2Ir_2O_7$. These materials have been thoroughly investigated and their structural and physical properties are reported on in following subsection and chapter 3.

2.1.4 Stability of pyrochlore structure

The knowledge on the details of the crystallographic properties of $A_2Ir_2O_7$ iridates is imperative for a proper interpretation of their magnetic and conductive properties introduced in subsection 1.2.2.

The pyrochlore structure of $A_2Ir_2O_7$ (and the majority of $A_2B_2O_7$) has been repeatedly reported and confirmed also by our studies. It is perfectly ordered cubic structure (space group $Fd\bar{3}m$) with only two free parameters: lattice parameter a and fraction coordinate of the oxygen anions at 48f Wyckoff position x_{48f}. Related Ir-O bond lengths and Ir-O-Ir bond angles play a crucial role in interpreting varying electronic and magnetic properties in $A_2Ir_2O_7$ materials [65, 88]. A recent report on $Eu_2Ir_2O_7$ showed anomalies in both the bond length and the bond angle at T_{Ir} [89]. The mechanism of the magnetic ordering of the Ir sublattice being responsible for the structural changes, or vice versa, would be highly useful for interpreting the magnetic properties of iridates. Therefore, we performed complementary structural and compressibility study using synchrotron X-ray diffraction techniques on selected $A_2Ir_2O_7$ iridates (A = Pr, Sm, Dy-Lu), including significantly understudied heavy-rare-earth members, inclusive of newly

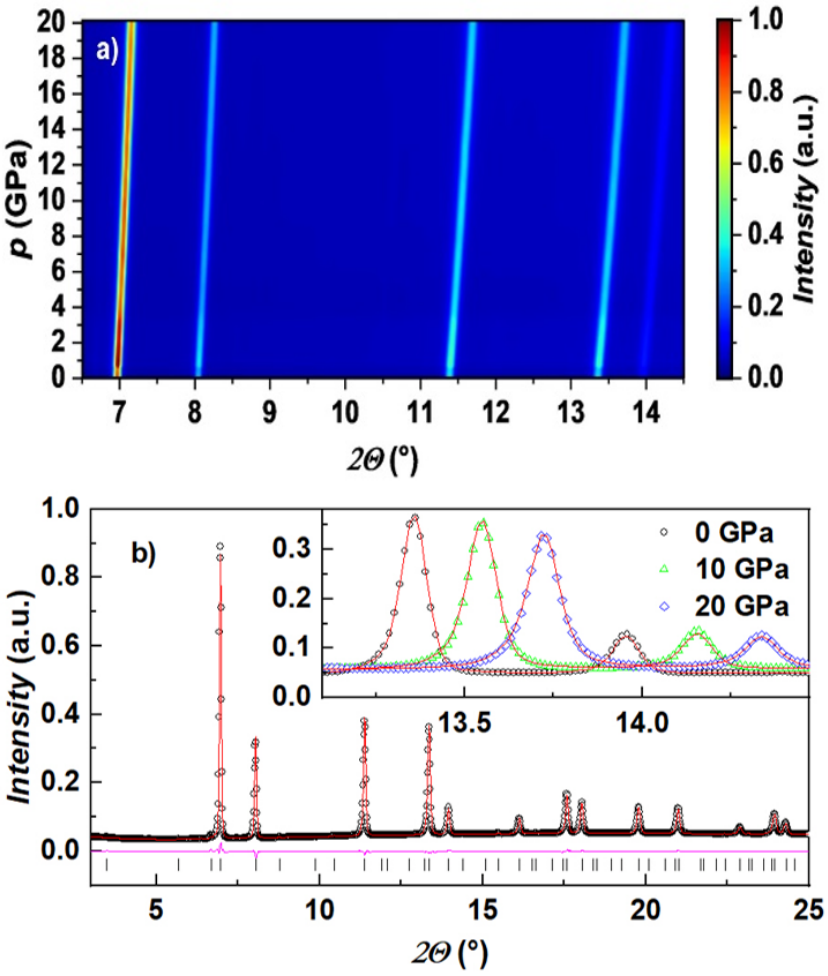

Figure 2.3: High-pressure diffraction of $Lu_2Ir_2O_7$. Pressure evolution of the pyrochlore peaks' position (a). No structural change is observed. Refined diffraction pattern at ambient pressure (b). The inset shows the pressure evolution of the peak shape - only small broadening was observed in pressure up to 20 GPa. The figure is adopted from Ref. [90] and slightly modified.

synthesised $Tm_2Ir_2O_7$.

Temperature and pressure evolution of crystallographic parameters were investigated by means of synchrotron X-ray radiation diffraction. Several synchrotron beamlines were used: ID22 and ID15b beamlines at ESRF (Grenoble, France); KMC-2 beamline at Bessy II (Berlin, Germany); and I15 beamline at DIAMOND (Didcot, United Kingdom). The diffraction patterns were collected on samples in a spinning capilary or loaded in a diamond anvil cell down to 4 K and up to 20 GPa [90]. Synchrotron data are naturally measured with high resolution up to high diffraction angles, allowing precise determination of structural parameters of investigated samples.

The diffraction patterns confirm the robustness of pyrochlore structure in investigated $A_2Ir_2O_7$ members in the whole temperature and pressure range. Essentially the same diffraction patterns were measured for all iridates at all temperatures and pressures; just changing depending on the actual lattice parameter.

The example of measured data is presented in Fig. 2.3. By pressure application, the diffraction peaks become broader, reflecting the inner strain in the material. The low-temperature diffraction patterns are sharper than those measured at room temperature due to reduced thermal fluctuations of the respective scattering centres (Debye-Waller factor). No differences from the expected behaviour was observed.

The lattice parameter a decreases with decreasing temperature, demonstrating a standard thermal contraction of the material. The compressibility of samples, or the pressure dependence of the lattice volume, follows the Birch-Murnaghan equation of state [90, 91]. The fraction coordinate x_{48f} remains constant within its error bars in the applied pressure. Simultaneously, it slightly decreases with increasing temperature (less than 1% from 4 to 300 K). Most importantly, no clear anomaly on x_{48f}, and connected Ir-O bond lengths and Ir-O-Ir bond angles, developments is observed in any temperature or pressure. Actually, comparing our data with a previous study of $Eu_2Ir_2O_7$ [89], the x_{48f} parameter behaves in a very similar way at around T_{Ir}. The anomaly previously reported cannot be unambiguously reproduced by our data as the error bars are larger than the quantitative change of x_{48f}. (Error bars in the previous report were not shown.) Moreover, similar anomalies could also be traced at different temperatures, not coincident with any characteristic temperature of the investigated $A_2Ir_2O_7$ iridates. See our recent publication [90] for further details.

The robustness of the pyrochlore structure in $A_2Ir_2O_7$ iridates allows an interpolation of structural parameters and a reasonable estimation of properties for the whole series. E.g., pressure impact on the $Yb_2Ir_2O_7$ member was not investigated; however, it can be reasonably estimated by combining compressibilities of the A = Tm and Lu members. Further, magnetic and conducting properties can be discussed with respect to structural details and application of chemical and external pressure. That is, external pressure can be compared with chemical pressure based on the change in the lattice parameter. E.g., an application of pressure on the $Pr_2Ir_2O_7$ member leads to a compression of the lattice; decreasing the lattice volume across the rare-earth series, and ultimately reaching the lattice parameter of $Yb_2Ir_2O_7$ at 20 GPa.

2.2 Growth of $A_2Ir_2O_7$ single crystals ¶

Introduction to unpublished results: **to be published in 2024.**

Being able to synthesise polycrystalline samples, including small single crystals with an edge of maximum 10 μm, we performed a number of macroscopic and microscopic experiments on $A_2Ir_2O_7$ (see chapter 3). However, investigations of anisotropic properties, as well as the use of many advanced techniques shedding light on the complex physics of these compounds, remained unattainable. There-

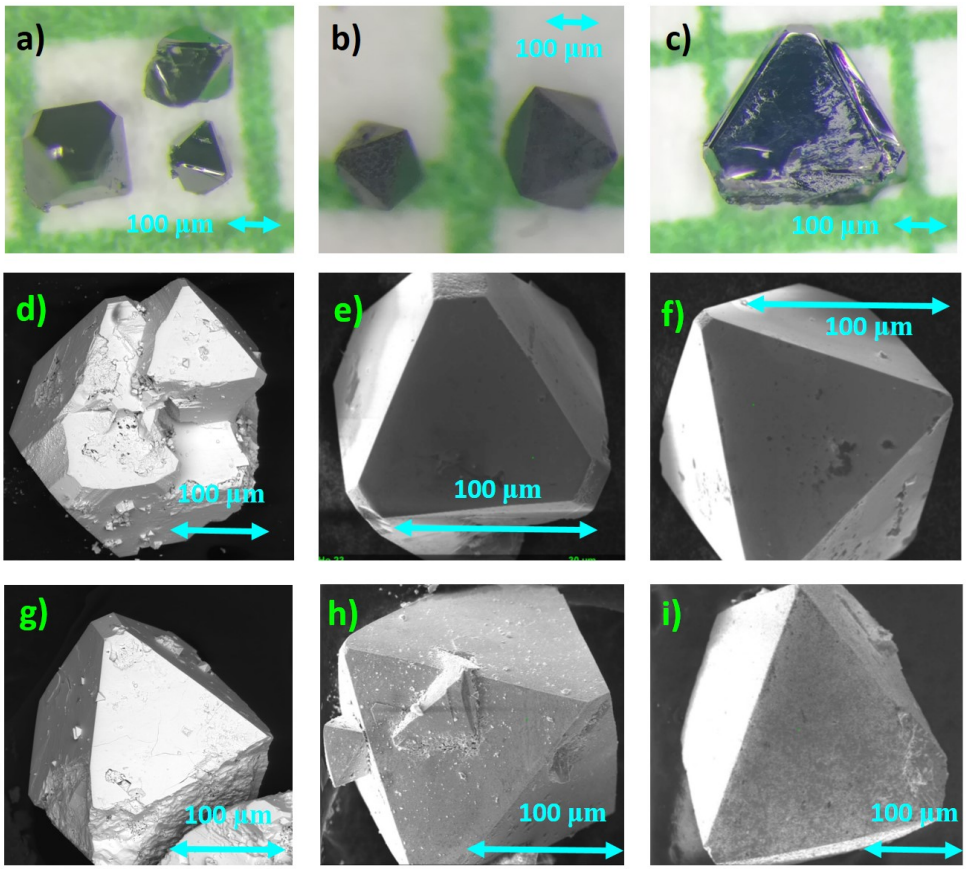

Figure 2.4: $A_2Ir_2O_7$ single crystals synthesised using PbF_2 flux. Photographs of $Er_2Ir_2O_7$ crystals (a-b) and $Nd_2Ir_2O_7$ single crystal (c) taken under optical microscope. BSE pictures from electron microscope of $Nd_2Ir_2O_7$ (d-e), $Ho_2Ir_2O_7$ (f), $Er_2Ir_2O_7$ (g-h), and $Lu_2Ir_2O_7$ (i) single crystals. The crystals with the edge larger than 100 μm were investigated by macroscopic and microscopic methods, allowing us also to reveal the anisotropic properties of respective $A_2Ir_2O_7$ iridates; these results are not presented in the thesis.

fore, we dedicated significant time and personnel to optimise the preparation process of $A_2Ir_2O_7$, aiming at larger single crystals.

First, we attempted to reproduce the recipe reported by Millican et al. [76]. The light rare-earth $A_2Ir_2O_7$ (Pr, Nd, and Eu [76, 92, 93, 94, 95]) were synthesised by mixing starting oxides A_2O_3 and IrO_2 in a stoichiometric ratio with KF flux and reacted at high temperature. Following the recipe, we were able to synthesise a relatively small single crystal with an edge of maximum 20 μm after multiple attempts. The attempts to synthesise larger single crystals were also done using CsCl flux; the same flux was employed for the growth of high-quality powder samples. However, the size of single crystals was limited as well. Searching for ideal flux material, we tested several other chemicals, namely NaCl, KCl, NaF, PbO_2, and PbF_2, and made also attempts using off-stoichiometric initial mixtures.

At first, none of the fluxes led to significant improvement of the synthesised single crystals, except the PbF_2 flux. Large single crystals of an edge of maximum 600 μm were prepared for A = Nd, Er, Tm, and Lu members. Examples

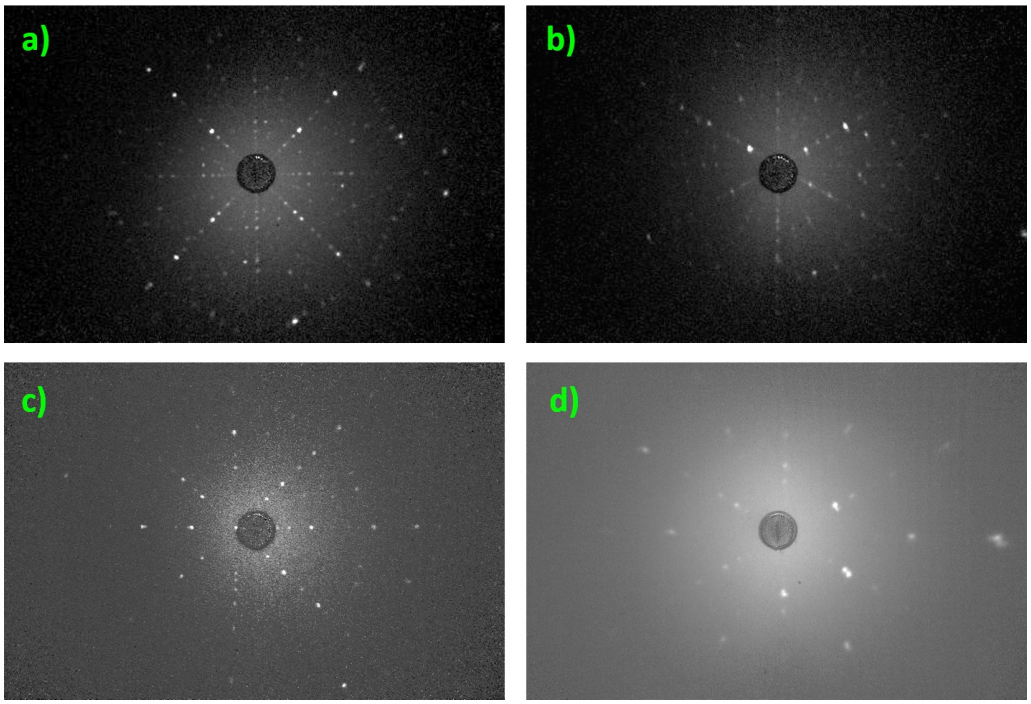

Figure 2.5: Laue X-ray images taken in back-scattering geometry on $Nd_2Ir_2O_7$ (a-b), $Er_2Ir_2O_7$ (c), and $Lu_2Ir_2O_7$ (d) single crystals. The patterns were recorded along the <100> (a,c) and <111> (b,d) crystallographic directions.

of synthesised single crystals are presented in Fig. 2.4, where a perfect shape of crystals with pronounced facets have been observed. See also examples of Laue X-ray images recorded on synthesised single crystals in Fig. 2.5. These samples were investigated by a variety of methods, leading to both consistency with polycrystalline results and information on anisotropy in the material (results to be published in the near future, not included in the present thesis). However, an accurate characterisation of these single crystals, EDX on polished surfaces, revealed inclusions of Pb in the bulk. Moreover, some samples exhibited partial substitution of rare-earth element by Pb. These observations demonstrate aggressiveness of the PbF_2 flux and prove it to be not ideal for the synthesis of $A_2Ir_2O_7$. Nevertheless, comparing e.g. the ordering temperature of iridium sublattice in polycrystal synthesised by CsCl flux and single crystal grown using PbF_2 flux, almost the same T_{Ir}'s (slightly lower in the case of single crystal) were determined.

Finally, we re-started our attempts using KF flux for single crystal synthesis. Dedicating a considerable time to the process, we optimised the preparation recipe using this flux. Single crystals comparable to PbF_2-flux grown crystals, but without inclusions and/or substitutions, were synthesised. The atomic mass/volume of potassium is significantly different from that of rare-earth and iridium, therefore, the substitutions are not very likely, compared to Pb.

Numerous measurements were made on these crystals. Besides bulk property measurements, magnetisation, specific heat and electrical resistivity, advanced microscopic techniques were employed. Neutron diffraction experiments

on $Nd_2Ir_2O_7$ single crystals (D23, ILL, Grenoble; and ZEBRA, PSI, Villigen) allowed one to study magnetic structures of Ir and Nd sublattices under applied magnetic field. Synchrotron radiation scattering experiments (D15b, ESRF, Grenoble; and I15, DIAMOND, Didcot) shed light on the evolution of the pyrochlore crystal structure under external pressure. Magnetic excitations in $Er_2Ir_2O_7$ and $Lu_2Ir_2O_7$ were investigated using resonant inelastic X-ray scattering (ID20, ESRF, Grenoble). These studies revealed and documented, e.g., domain hypothesis (see subsection 3.1.4), 2I2O and 3I1O arrangements of magnetic moments on rare-earth sublattice under applied magnetic field, or Ir magnon excitations below 100 meV and spin-orbit and crystal field excitations at higher energy. These briefly introduced results are not part of the present thesis as the analysis of the collected data has not been finished. We intend to publish our results on single crystalline samples, some of them in collaboration with our colleagues from the Institut Laue-Langevin, the European Synchrotron Radiation Facility, the Institut Néel, CNRS, and Université Paris-Sacley, in the coming year/s. In addition, several other experiments are being planned and proposed for. Most importantly, synchrotron X-ray micro-diffraction mapping of magnetic domains and domain walls promises highly important results.

2.3 Synthesis of $A_2Zr_2O_7$ zirconates ¶

Introduction to publications: **1., 3., 5., 6., 13., 15., and 17.**

Many $A_2B_2O_7$ single crystals have been prepared from a pre-reacted precursor of the same stoichiometry employing floating-zone method, e.g., Refs. [69, 96, 97]. This method can be used for chemically stable materials with low evaporation and vapour pressure on heating and in melt. (Hence, we cannot employ a floating zone method when preparing $A_2Ir_2O_7$ materials introduced above.) Crucible-free growth is realised in a furnace, typically with radiation heating, enabling melting of only a specific part of the precursor. The single crystal is formed by pulling the precursor through the hot zone under specific conditions (atmosphere, temperature of melt, speed of pulling and rotation of ingot and precursor, possible use of after-heater [98]). In the following part, we describe the preparation process of selected $A_2Zr_2O_7$ and $A_2(Ti,Zr)_2O_7$ single crystals in detail. Introduced general recipe can be, of course, used for other $A_2B_2O_7$ members, as well as for unrelated compounds.

2.3.1 Floating zone synthesis

A number of good-quality $A_2(Ti,Zr)_2O_7$ crystals have been prepared following the recipe described below. We demonstrate the preparation on $Er_2Ti_2O_7$ compound (further details are accessible in respective publications of the author, the most detailed description in Refs. [72, 99]):

(i) The mixture of powder Er_2O_3 and TiO_2 oxides (99.99% metal basis, AlfaAesar) in the molar ratio 1:2 was thoroughly homogenised and slowly packed into the rubber mould under vibrations.
(ii) Subsequently, it was compressed into the form of a rod in a home developed pressure cell under quasi-hydrostatic conditions (nominal pressure of 200 kPa).
(iii) The resulting rod of 9 mm diameter and 80 mm length was taken from the mould and pre-sintered on Pt plate at 1100 °C for several days in air. The sintering was done solely to prevent the rod from falling apart in the course of further manipulation. Optimising the precursor preparation process, we found out, that pre-sintering time of just one day, and in some cases just five hours, is sufficient. The partial reaction, solid state reaction, between two initial oxides took place. Nevertheless, sintered precursor contained only a minor fraction of $Er_2Ti_2O_7$. On sintering, a shrinkage of the sample volume of approximately $\frac{1}{6}$ was observed.
(iv) The sintered precursor was cut into two pieces: a small part of the precursor (15 mm) was used as a seed, while the second part served as a feed rod. On the cut surface, we identified the inner part of the rod to consist of a mixture of two initial oxides, while the outer ring had a clearly different texture, documenting partly reacted material. The pieces were shaped to best absorb the radiation.
(v) Single crystal was prepared employing an optical floating zone furnace (optical-image-furnace FZ-T-12000-X-VI-VP (Crystal Systems Co., Kobuchisawa, Japan) with xenon-arc-lamps; or FZ-T-4000-VI-VPM-PC furnace with halogen-lamps and focussing mirrors) or laser floating zone furnace (CSC FZ-LD-5-200W-II-VPO-PC with five laser diodes). The seed rod was held in the bottom furnace shaft, while the feed rod was freely hang on the upper shaft. The floating zone that had a width of ∼8 mm was established between the seed and feed rods, for optical furnaces. The width of the floating zone in the laser furnace was smaller, by using focussing lenses reaching only about 4 mm. Subsequently, the precursor was pulled through the molten zone at speed of 5 mm.h^{-1} while counter-rotated at 35 rpm. The growth of the single crystals was carried out in air under 155 kPag gauge pressure with a flow rate of 1.0 liter per minute.
(vi) In several cases, the precursor was melted three times to ensure a good homogeneity of the constituting elements within the ingot and a good quality of the prepared single crystal. After first melting, the precursor shrank by approximately $\frac{1}{3}$ of volume (resulting to $\sim$ 6 mm diameter) without any apparent evaporation of the constituent elements/oxides. The ingot volume did not change noticeably during second and third melting. The examples of synthesised ingots from the $Er_2(Ti,Zr)_2O_7$ and and $A_2Zr_2O_7$ series' are presented in Fig. 2.6 and 2.7 (first parts of the series' are synthesised using floating hot zone method).

We note that the commonly used preparation route, reported in many publications, e.g., Refs. [69, 96, 97], is based on melting already pre-reacted polycrystal of $A_2B_2O_7$. Our simplified preparation process, reacting directly the initial oxides, allows to minimise the composition deviations and time losses by skipping the

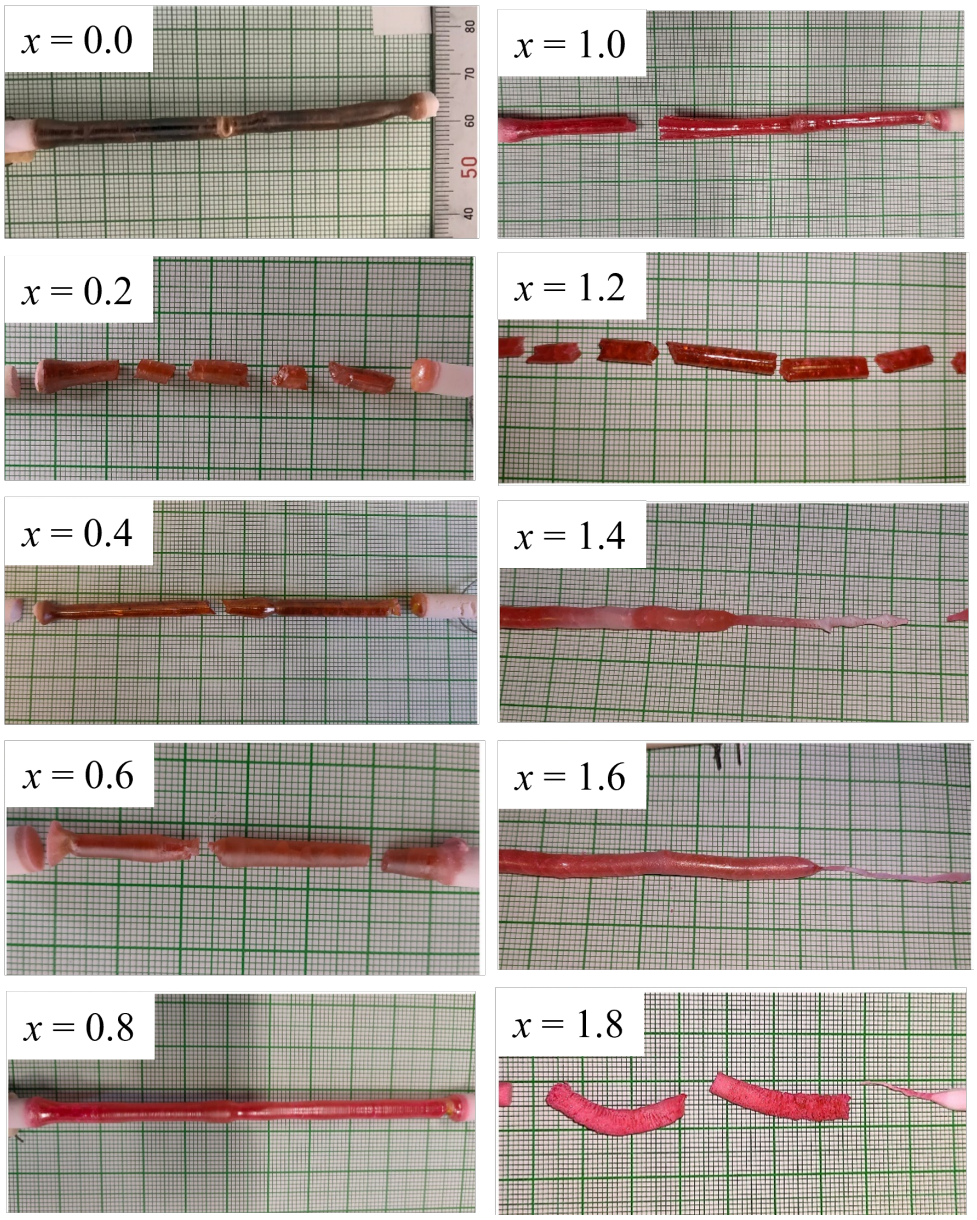

Figure 2.6: $Er_2Ti_{2-x}Zr_xO_7$ ingots synthesised using a laser furnace and floating zone ($x \leq 1.2$) or Czochralski ($x \geq 1.4$) technique. Details on the preparation and quality of the ingots are provided in the text.

initial phase of the polycrystalline precursor synthesis. Repeated heating-cooling cycles with intermediate grindings of the initial mixture are omitted. It is also possible to completely avoid any contamination of the polycrystalline precursor with the mortar material during its grinding. Moreover, the compression of powder material into seed/feed rod can be done easily under lower pressure, since non-identical powder grains of initial oxides have arbitrary surface (including sharp edges and vertices). In contrast, a pre-reacted material is ground several times (to obtain a good homogeneity within the precursor volume) leading to almost identical spherical grains which are hard (and sometimes impossible, depending on grinding method and homogeneity of pre-reacted material) to connect to each other by even relatively high pressure. Therefore, the preparation of suitable precursor might be an issue. Our preparation process naturally eliminates these

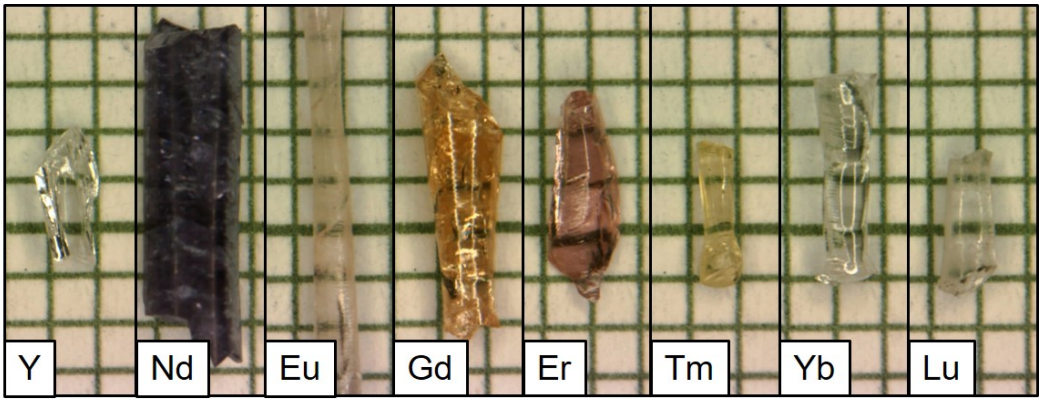

Figure 2.7: Fragments of $A_2Zr_2O_7$ ingots synthesised using a laser furnace and floating zone (A = Y, Nd, Eu) and Czochralski method (A = Gd - Lu). The edges of the squares behind the crystals are millimetre size, for scale. The figure is adopted from Ref. [99].

problems, leading to a comparable or better quality of the synthesised crystals.

In addition, the presented synthesis route enables growth of some compounds with less stable initial elements or oxides (although it is not the case of our reported zirconates). The reduced thermal treatment of the precursor, compared to the standardly used route, leads to lower material losses, which must be further compensated for by off-stoichiometry of the initial mixture. Although the presented method is ideal for preparation of many compounds, highly volatile precursor materials/products cannot be synthesised for reasons common to floating-zone methods.

2.3.2 Czochralski method

The preparation of heavy rare-earth $A_2Zr_2O_7$ single crystals and high Zr-content $Er_2(Ti,Zr)_2O_7$ compounds is severely complicated by high melting temperature of A_2O_3 and especially ZrO_2 oxides used as initial reactants (2200-2500 °C and 2715 °C, respectively). High heating power must be generated by furnaces, while a significant portion of power is lost due to:
(i) source focussing issues, beam of photons must be precisely focused on the surface of the precursor;
(ii) sample refractivity, interface between two substances changes the direction of incoming radiation;
(iii) sample absorbance for radiation, connected with colour of material/melt;
(iv) sample thermal conductivity, conducting and distributing received heat to the material volume.
It is basically impossible to counter the properties of synthesised material using the floating zone method. In order to change a wavelength of radiation, which could allow better heat absorption by the material, a different furnace must be used as the source is usually not exchangeable. Therefore, only a shape of the

precursor can be tuned to face as much radiation as possible and absorb it; to make the heating of the precursor as efficient as possible.

One end of the seed rod precursor was shaped into a cone and pointed with its vertex toward the feed rod with flat top end. We utilised two less-standard options for the used laser furnace. First, focussing lenses were used. The effective area irradiated by a laser was thus 4 x 4 mm, instead of 8 x 4 mm. Second, laser diodes were tilted up to 30 degrees from the horizontal direction (direction perpendicular to vertically held precursors). With such a setup, the radiation was directed primarily on the flat surface of the feed rod, allowing maximum absorption of heat by the precursor. Moreover, the flat surface reflected and irradiated the portion of accepted light towards the seed rod hung above. The seed rod was thus heated not only by radiation coming from the laser source, but also from the feed rod. Of course, the seed rod irradiated part of the heat received back to the feed rod. The used setup thus allowed for a significant increase in the temperature of the feed rod and, in turn, the seed rod.

By fully exploiting the laser furnace, it was used with 95-100% of maximum power (1000 W), and using shaped precursors described above, all synthesised materials (whole $A_2Zr_2O_7$ series, except A = Ce and Tb, which were not selected for the study) were melted. However, connecting the seed and feed rods was usually possible only by a narrow neck of melt. Increasing the diameter of the neck means more melt in the hot zone, which must be sufficiently heated by radiation. Nevertheless, the shape of the neck changes the geometry of the process, radiation paths to the material, and thus the heat received by the melt. Combination of these factors led to freezing of the melt. The ingot growth was forced to end for necks with diameters larger than 2 mm. Using the floating-zone method, requiring a stable connection between seed and feed rods and ideally counter-rotation of rods, was therefore mostly impossible. Only a very small part of the ingot was grown by this method before the seed and feed rods were either separated or tightly connected by frozen melt.

Together with the optimisation of the precursor shape, a different preparation technique was also used. The Czochralski method of single crystal growth is a well-known and widely used technique; most noticeable is its intensive usage for the synthesis of large and excellent-quality silicon single crystals. This technique consists in pulling the crystal seed out of the melt, which is exactly the technique usable in the situation described above. The melt is established by the geometry of the laser furnace and the shape of the precursor. The vertex of the seed rod is introduced to the melt and pulled out at a constant rate. A part of the melt removed from the pool solidifies into a crystal, as demonstrated in Fig. 2.6 for $Er_2Ti_{2-x}Zr_xO_7$ with $x \geq 1.4$. See also Fig. 2.7 for ingots of comparable quality synthesised using floating zone (A = Y, Nd, Eu) and Czochralski method (A = Gd - Lu).

Contrary to the floating zone method, the Czochralski method allowed for a preparation of significantly smaller ingots. The remainder of the precursors was

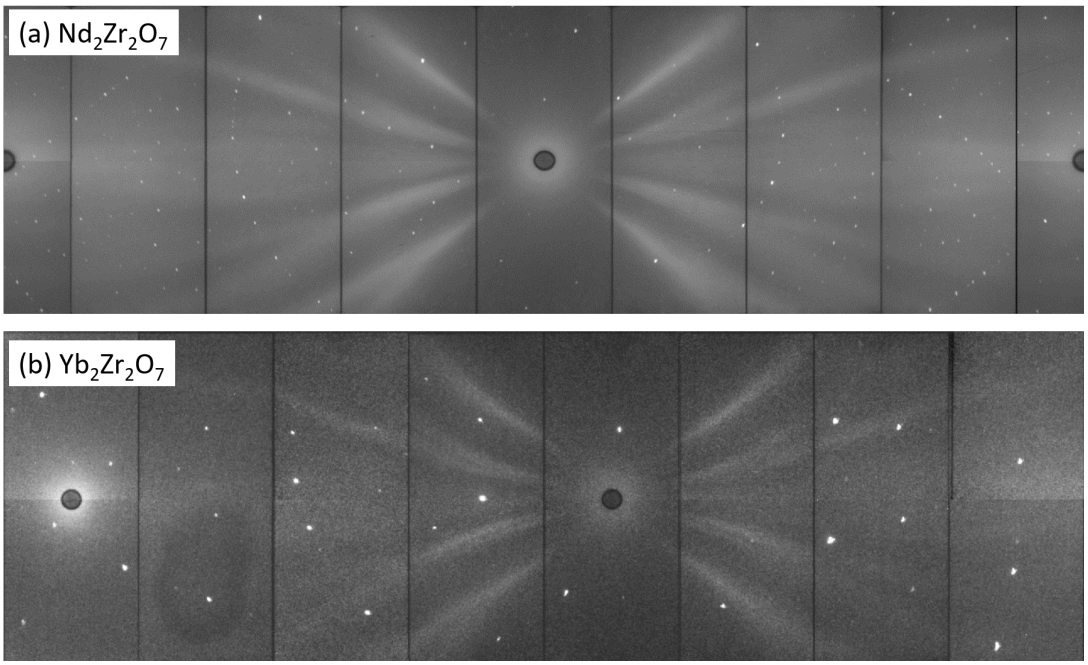

Figure 2.8: Laue neutron diffraction patterns measured on $Nd_2Zr_2O_7$ single crystal (a) and $Yb_2Zr_2O_7$ single crystal (b) using the CYCLOPS instrument at the Institute Laue-Langevin, Grenoble, France. The diffraction patterns correspond to the pyrochlore structure and defect-fluorite structure, respectively.

not melted, but sintered at a high temperature reaching 2600 °C. Sintering at such high temperature accelerated the solid-state reaction of the initial oxides (Fig. 2.6, e.g., $x = 1.8$), leading to good-quality polycrystalline heavy rare-earth $A_2Zr_2O_7$.

The quality of prepared single crystals (and polycrystals) was investigated by a spectrum of experimental methods. A small part of the prepared ingot was ground and investigated by powder X-ray diffraction (Bruker D8-Advance with CuKα radiation). The diffraction patterns indicated single phase samples in case of $A_2Zr_2O_7$, no additional peaks were observed. The average crystal structure was confirmed to be either of the pyrochlore type ($Fd\bar{3}m$) or the defect-fluorite type ($Fm\bar{3}m$), depending on A. In the case of substituted series' A_2(Ti,Zr)$_2O_7$, in addition to majority pyrochlore, defect-fluorite or even rhombohedral structure, also signs of short-range correlations were observed (see section 4.2 and 4.3). The synthesised ingot was cut to several pieces with long edges parallel to the principal crystallographic directions [100], [110], and [111] of the cubic lattice for further measurements. These parts were checked (and oriented) using Laue X-ray diffraction method in back-reflection geometry, confirming good quality of the prepared single crystals. Homogeneity and phase purity of prepared ingots were also investigated employing electron scanning microscope and EDX. Despite the low electronic conductivity of the prepared samples and the low sensitivity of EDX to oxygen, the analysis of the energy spectra allowed us to confirm the phase purity of the samples and A:B ratio to be 50($\pm$2):50($\pm$2) for all compounds. The quality of selected ingots was furthermore checked in whole volume employing

Laue neutron diffraction and the CYCLOPS instrument [100] at the Institut Laue-Langevin, Grenoble. The measured Laue neutron patterns in Fig. 2.8 demonstrate single phase single crystals crystallising in the pyrochlore and defect-fluorite structure, respectively.

3. Electronic properties of $A_2Ir_2O_7$ iridates ¶

Introduction to publications: **2., 4., 7., 8., 10., 11., 12., and 16.**

The rare-earth iridates $A_2Ir_2O_7$ belong to a broad family of pyrochlore oxides $A_2B_2O_7$ with frequently complex and exotic electronic properties, including, e.g. fragmentation of magnetic moments in $Ho_2Ir_2O_7$ [7, 30], complex magnetic structures in $Nd_2Ir_2O_7$ [101, 102], $Tb_2Ir_2O_7$ [28], and $Yb_2Ir_2O_7$ [27] originating in interaction of A and Ir sublattices, or spin-liquid and spin-ice states dictated by geometrical frustration of the pyrochlore lattice of theirs [5, 6, 103]. The diversity of ground-states observed in $A_2Ir_2O_7$ oxides stems not only from the geometrical frustration of magnetic moments, but also from the competition and delicate balance among exchange, dipolar, and spin-orbit interactions in the system. The influence of the spin-orbit coupling on the magnetic and electronic states and often weak or intermediate electron Coloumb correlations in iridates [104, 105, 106] generate topologically non-trivial phases (Fig. 1.3), e.g. topological Mott insulator or topological band insulator, a Weyl semimetal state and Fermi-arc surface states [106, 107, 108, 109].

The iridium sublattice orders magnetically at higher temperatures than rare-earth sublattice in all, so far studied, iridates, except $Pr_2Ir_2O_7$ without magnetic ordering [60, 108]. The magnetic ordering of the Ir sublattice has been reported/proposed to be antiferromagnetic of the so-called all-in-all-out (AIAO) type: All magnetic moments point along local <111> directions in or out of the tetrahedron (see Fig. 1.2a). The studies documenting this type of ordering were based primarily on neutron diffraction experiments on powder samples [27, 28, 61], which are harshly limited by a small magnetic moment on Ir (estimated $< 0.5\ \mu_B$) and relatively high neutron absorption cross-section of Ir. Although the community has mostly accepted the AIAO structure of Ir, none or only ambiguous signs of the magnetic signal were observed for several members [61, 62]. Importantly, a recent neutron diffraction study on $Lu_2Ir_2O_7$ with non-magnetic Lu^{3+} ion revealed several magnetic peaks consistent with AIAO magnetic structure [27], well demonstrating the ordering of pure Ir sublattice.

In addition to the antiferromagnetic ordering, an application of a magnetic field along the <001> (<111>) direction has been expected to overcome the exchange interactions, and turn two (three) magnetic moments in AIAO tetrahedra to point in, and the other two (one) to point out (Fig. 1.2) [6, 27]. Therefore, spin-ice and magnetic monopole-like states can be induced by an external field (due to competing interactions on the frustrated pyrochlore lattice). Concomitantly with the magnetic ordering of the Ir sublattice, $A_2Ir_2O_7$ undergo a transition from metal/semi-metal/semiconductor to an insulating state (MIT) [34, 35, 57]. See Figs. 1.3 and 1.5 for illustration. The transitions, magnetic and

related MIT, are strongly influenced by the tuning of the Ir-O-Ir bond lengths and angles [64], which modulate the valence-electron bandwidth and therefore the effective correlation strength. Ir-O-Ir bond bending vibration is strongly coupled to a continuum composed of spin, charge, and orbital excitations via a confluence of all three mechanisms [66].

Chapter 3 consists of two parts focussing on the iridium and rare-earth ion and sublattice properties, respectively. The interaction between two sublattices is discussed in the text as well. All presented results were measured/determined on newly synthesised samples (as introduced in chapter 2, section 2.1) in the home laboratory (mgml.eu) and large-scale facilities: the Institute Laue-Langevin (ILL) and the European Synchrotron Radiation Facility (ESRF), Grenoble, France; the Rutherford Appleton Laboratory (RAL, ISIS) and the DIAMOND synchrotron, Didcot, United Kingdom; and the Helmholz Zentrum Berlin (HZB), Berlin, Germany. The following text serves as a brief introduction to our recent results. More details, both technical and interpretative, are available in the respective publications of the author and cited references.

3.1 Iridium sublattice ¶

***Introduction to publications:* 2., 7., 8., 10., 12., and 16.**

Relativistic SOC is considered a small perturbation to the overall properties of light elements but becomes significantly stronger with an increasing atomic number of the element (as Z^4). Demonstrating it on the case of the d-elements: SOC plays a crucial role in the formation of electronic properties and magnetic ground state of compounds containing heavier 4d and 5d elements, while it is just a weak perturbation in 3d element compounds. Simultaneously, the d-orbitals become more extended with increasing Z. The electronic repulsion and electron correlation effects are thus weaker in heavier elements. The SOC and electron correlations are expected to have a similar strength in heavy elements (namely 5d elements), which leads to a spectrum of complex physical phenomena as demonstrated in Fig. 1.3: topological Mott insulator [37, 38], Weyl semimetal [35, 36], axion insulator [52], spin-liquid states [5], or spin-ice with monopole-like excitations [6]. A strong SOC is, moreover, a prerequisite for the spin Hall effect (SHE) and the inverse SHE [53].

$A_2Ir_2O_7$ pyrochlores with a heavy 5d-element represent one of the Ir systems revealing the properties and states introduced above and are potentially usable in applications, in addition to other heavily studied systems [53, 110, 111].

3.1.1 Magnetic ordering of iridium sublattice, μSR

The iridium sublattice orders magnetically below the ordering temperature, T_{Ir}, in A = Y, Nd - Lu members. No long-range magnetic ordering was observed

in $Pr_2Ir_2O_7$ [60, 112]. A = La and Ce members have not been synthesised, so far. The magnetic structure of the all-in-all-out type of Ir moments ordering was determined by neutron diffraction, resonant elastic X-ray scattering (REXS), Raman scattering, or muon spin resonance techniques for several members (A = Nd, Sm, Eu, Tb, Yb, Lu) [27, 28, 66, 101, 113, 114, 115]. No magnetic signal/no clear signal was observed in the neutron diffraction data for A = Er [61] and Tm [62].

Previous studies of the transport properties, as well as magnetic properties, were focused primarily on the lighter rare-earth $A_2Ir_2O_7$, mostly neglecting the later part of the series. To explore the physical properties of heavy rare-earth iridates, we synthesised polycrystalline samples with A = Dy - Lu, including newly prepared $Tm_2Ir_2O_7$ (see section 2.1). Well-defined polycrystalline samples were studied by means of a number of bulk and microscopic methods, allowing us to complete the picture on systematics in the series.

Magnetisation. The magnetic ordering of the iridium sublattice in $A_2Ir_2O_7$ compounds is characterised by a bifurcation of magnetisation data measured under zero-field-cooled (ZFC) and field-cooled (DC) regime (Fig. 3.1). Most of the samples reveal a weak anomaly on the ZFC curve just below the ZFC-FC splitting [34, 57, 60, 112, 116]. In fact, the bifurcation could be ascribed to an onset of the (short-range) magnetic ordering, whereas long-range order is established at slightly (maximum few kelvins) lower temperature. Nevertheless, the temperature at which the magnetisation curves bifurcate is usually denoted as the ordering temperature in most reports. We mark this temperature as T_{Ir}.

Contrary to light $A_2Ir_2O_7$, the change of T_{Ir} with A in heavy rare-earth members is small (Fig. 1.5). See section 3.1.3 for completed phase diagram and further details. Applying a higher magnetic field, the bifurcation closes down, and no difference between the data measured under ZFC and FC regime is observed above 0.5 T. The magnetic response, $\frac{M}{H}$, remains the same regardless of the value of the magnetic field below T_{Ir} down to temperature T_{A} (see Fig. 3.7 and Table 3.1 in the following text). A clear difference between $\frac{M}{H}$ measured at different fields is observed below T_{A}, indicating magnetic correlations among A^{3+} ions and crystal field acting on them. This conclusion is strongly supported by the μSR experiment on $Yb_2Ir_2O_7$ [112]. The reported anomaly in μSR data is observed at the temperature determined from our magnetisation data T_{A}. A similar μSR response is expected also from the other members showing magnetisation change at respective T_{A}'s.

Our recent **μSR experiments** on A = Er, Tm, Yb, and Lu iridates exhibit a strong depolarisation of the implanted muon ensemble. The large fluctuating magnetic moment of the A^{3+} ion leads to a rapid depolarisation of the muon spin, except $Lu_2Ir_2O_7$ with non-magnetic A = Lu. In addition to this component of the signal, the slow-relaxing component attributable to Ir sublattice is followed. The analysis of μSR data measured on $Er_2Ir_2O_7$ was summarised in our publication [118]. Our recent measurements of μSR on A = Tm, Yb, and Lu members

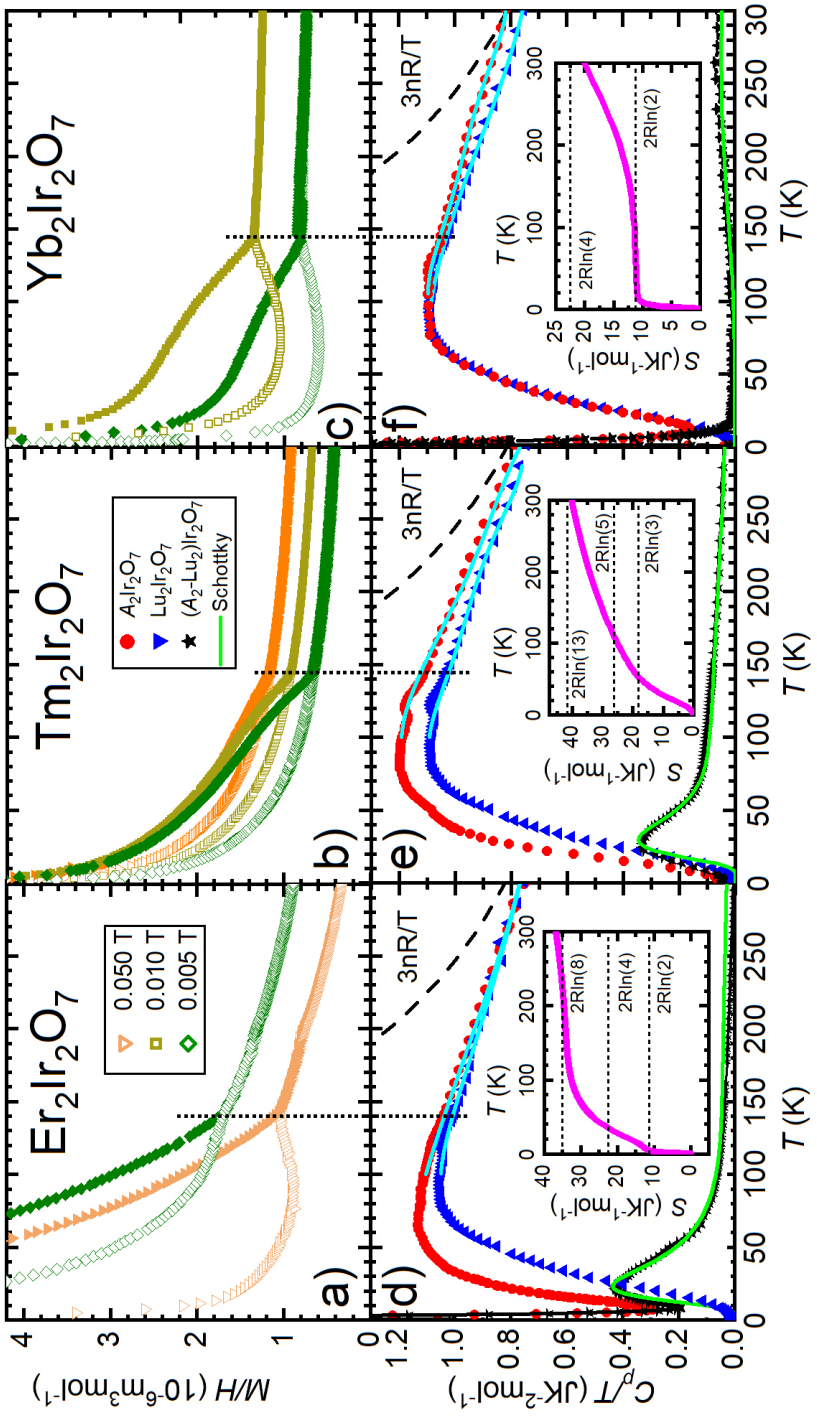

Figure 3.1: Temperature dependence of magnetisation (a-c) and specific heat (d-f). Magnetisation data measured under the ZFC regime (open symbols) and FC regime (full symbol) exhibit a bifurcation at a temperature denoted by a vertical line. The specific heat of $A_2Ir_2O_7$ is presented together with $Lu_2Ir_2O_7$ [117] and their difference. The specific heat around and above the high-temperature anomaly is approximated by a smoothed line. The calculated Schottky contribution (from crystal field energies, subsection 3.2.2) to specific heat is shown as well. The high-temperature phonon specific heat limit is shown as a dashed line. The insets contain entropy calculated from $(A_2\text{-}Lu_2)Ir_2O_7$ data for the respective oxides. The figure is adopted from Ref. [57].

are being evaluated. Preliminary analysis reveals consistent and generally the same evolution of muon oscillations with temperature (Fig. 3.2). An anomaly can be immediately seen in the magnitude of the slow-relaxing component at around 140 K for all investigated iridates, which is consistent with T_{Ir}. Additional change of the signal is clearly observed at lower temperature below T_{A} in $Er_2Ir_2O_7$ and $Yb_2Ir_2O_7$. No similar low-temperature signal is observed for non-magnetic $Lu_2Ir_2O_7$ and $Tm_2Ir_2O_7$ with singlet ground state (subsection 3.2.2). Such evolution strongly suggests the low-temperature magnetic correlations between rare-earth moments and likely also d-f coupling in these materials.

Specific heat. Specific heat data reveal an anomaly just below T_{Ir}, demonstrating a good agreement with magnetization and μSR results (Fig. 3.1). The observed anomaly was previously reported only for the light A iridates [60]. Our data thus document consistency not only between magnetisation and specific heat data, but also within the entire $A_2Ir_2O_7$ series. The anomalies in all the members are relatively broad, suggesting a rather continuous character of the magnetic transition. The effect of the A sublattice on the shape of the anomaly is concluded to be small, as no particular differences are distinguished when data on iridates with magnetic and non-magnetic A's is compared.

Electrical resistivity. High-temperature electrical resistivity data reveal increasing electrical resistivity with decreasing temperature. The increase becomes considerably steeper below T_{Ir}. The value of the electrical resistivity increases by 3 to over 6 orders of magnitude upon cooling for respective $A_2Ir_2O_7$. In light rare-earth members, the transition is pronounced as a clear anomaly in electrical resistivity data on a semi-logarithmic scale [60]. The anomaly broadens continuously with an atomic number of A for heavier rare-earth members [27, 60], and is observable only on a fully logarithmic scale. Importantly, the maximum change of resistivity slope is exhibited not at T_{Ir} but at a lower temperature, denoted as $T^{\star}$, for all investigated iridates (Fig. 3.3 and Table 3.1). No thermal hysteresis was measured around $T^{\star}$ (or T_{Ir}), indicating a continuous second-order phase transition.

Considering the temperature of a bifurcation and a weak anomaly in magnetisation data, anomaly in specific heat data and change of slope in electrical resistivity data, the temperature of magnetic transition and its determination should be addressed (for more details, see our report [119]). The ordering temperature of $A_2Ir_2O_7$ compounds is frequently identified as the temperature of a bifurcation of ZFC and FC magnetisation data measured in a low magnetic field. Here it is denoted as T_{Ir}. This bifurcation can be attributed to the Ir magnetic domain walls formation along with the long-range AFM ordering of the Ir sublattice [33]. See section 3.1.4 for detailed explanation. The long-range ordering is then characterised by a weak anomaly in magnetisation below T_{Ir}. Such explanation is supported by both specific heat and electrical resistivity data (see Fig. 3.3). T_{Ir} denotes a high-temperature onset of the anomaly in the specific heat. The anomaly is relatively broad [57, 116, 120] and is centered around $T^{\star}$ as deter-

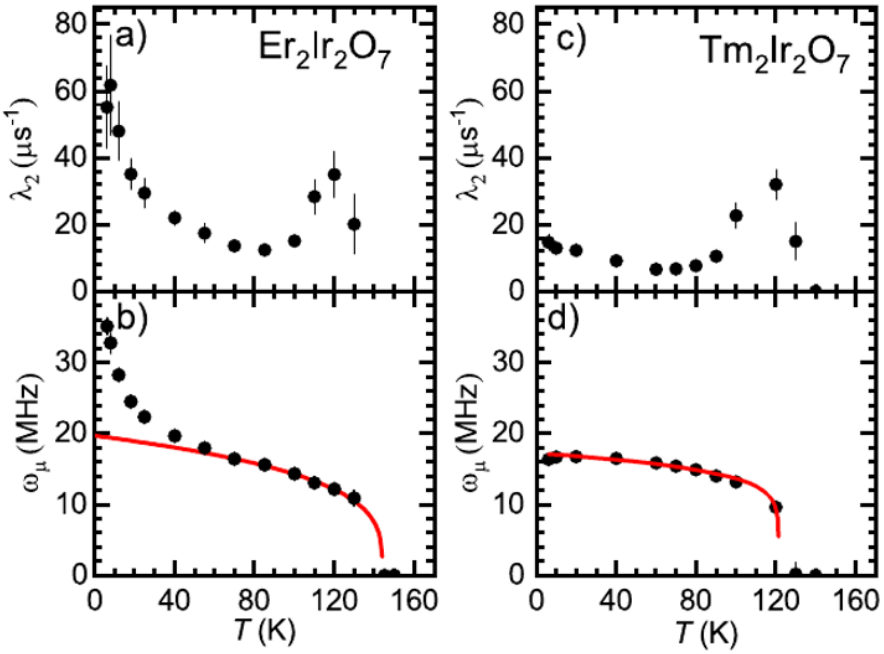

Figure 3.2: Temperature dependence of μSR coefficients showing the anomalies connected with the Ir-sublattice magnetic ordering below T_{Ir}. Apparently different behaviour below T_{A} is observed for $Er_2Ir_2O_7$ and $Tm_2Ir_2O_7$ members. The figure is intended for our final publication [118].

mined from the electrical resistivity data [119]. Importantly, both specific heat and electrical resistivity reveal a similar broadness of the transition without any thermal hysteresis, clearly indicating the continuous nature of the second-order transition.

3.1.2 Conductive properties

Concomitantly with the magnetic ordering, the conductive properties of pyrochlore iridates change below T_{Ir}. The transition from metal/semi-metal/semiconductor to insulator (MIT transition) has been followed in a number of $A_2Ir_2O_7$ iridates upon cooling ([60, 108], references therein, and Fig. 1.5). Importantly, the critical temperature is generally independent of the magnetism/electronic properties of the rare-earth ions. Instead, T_{Ir} is tightly related to interatomic distances and bond angles in the pyrochlore lattice; see the subsection 3.1.3.

The conductive properties of $A_2Ir_2O_7$ iridates are highly sensitive to the sample quality, e.g. [4, 60, 65, 121]. Significantly different properties were measured on samples with nominally the same stoichiometry, especially when comparing poly- and single crystals [94, 95, 122]. The Ir deficiency shifts the T_{Ir} to (significantly) lower temperature [94]. The absolute values of the resistivity and its relative changes with temperature were reported to differ by orders of magnitude depending on the investigated sample, e.g. [4, 60, 64, 122].

The mechanism relating the magnetic ordering and MIT in $A_2Ir_2O_7$ iridates must be discussed. Our resistivity data, well above T_{Ir}, can be reasonably de-

scribed using the Arrhenius thermal activation law. The activation energies listed in Table 3.1 suggest that all studied heavy A members are narrow-gap semiconductors above T_{Ir}. Determined energies are reasonably similar to previously published ones [60, 94] and show no clear dependence on the atomic number of A. Discussing the evolution of electrical resistivity in the insulating state, we took into consideration different models to describe our data [119]:
(i) power-law behavior ($\rho = \mathrm{p}T^{\mathrm{n}}$) with n $\simeq$ -2 is observed for A = Dy - Tm members, whereas the evolution of electrical resistivity of A = Yb - Lu resembles n $\simeq$ -4 development. The power-law behaviour with n = -4 is predicted within the single-particle model for Weyl fermions scattering from the random Coulomb potential − thermally screened charged impurities model (TSCI) [123]. This model has been used, e.g., to describe the electrical resistivity of $Y_2Ir_2O_7$ [124] and lighter A members [122]. An interplay between Weyl semimetal (WSM) and Mott insulating states was predicted for $A_2Ir_2O_7$ oxides [107]. However, inspecting the data [119], the WSM TSCI model cannot alone explain the complex behaviour of all heavy-rare-earth iridates, and does not present a well-defined dependence of the coefficient n on the atomic number.
(ii) Mott variable range hopping (VRH) model is commonly used to describe the conductive properties of strongly disordered systems with localised charge-carrier states. This model has been employed to explain the behaviour of pyrochlore iridates [121, 122, 94] despite the fact that the pyrochlore structure is fully ordered. Possible off-stoichiometry, common in these materials − that is, source of charged impurities − however, justifies the use of this model. The data are reasonably well described at intermediate temperatures, but the model fails at low temperatures (below 30 K). The disagreement between the VRH model and the data indicates good quality of our samples with none or only minor site disorder in the lattice.
(iii) Slater insulator model is related to antiferromagnetic ordering, in contrary to the Mott model based on the Coulomb interaction between charge-carrier states. As a result of commensurate AFM ordering, there is a periodic perturbation of the potential that leads to a splitting of the energy band, independent of strong Coulomb interaction [125, 126]. The Slater model was used to explain the behaviour of $Cd_2Os_2O_7$ compound [127, 128, 129]. $Cd_2Os_2O_7$ is isostructural to $A_2Ir_2O_7$ iridates and reveals the same type of antiferromagnetic ordering (AIAO type) of Os moments, as well as an MIT. As the magnetic and crystallographic unit cell are identical, the Slater mechanism without Brillouin zone-folding must be employed [128]. Due to an interplay between SOC and electron correlation is, however, difficult to distinguish between the Mott and the Slater mechanisms that are responsible for the MIT. The Stater model anticipates the gap at the Fermi level induced by the AFM ordering. Such gap is indeed observed in $Cd_2Os_2O_7$, at least just below T_{Os} [127, 129]. Heavy rare-earth iridates exhibit narrow-gap semiconducting behaviour in the paramagnetic regime, well above T_{Ir}. The emergence of a gap at the Fermi level at or below T_{Ir} might thus be masked and

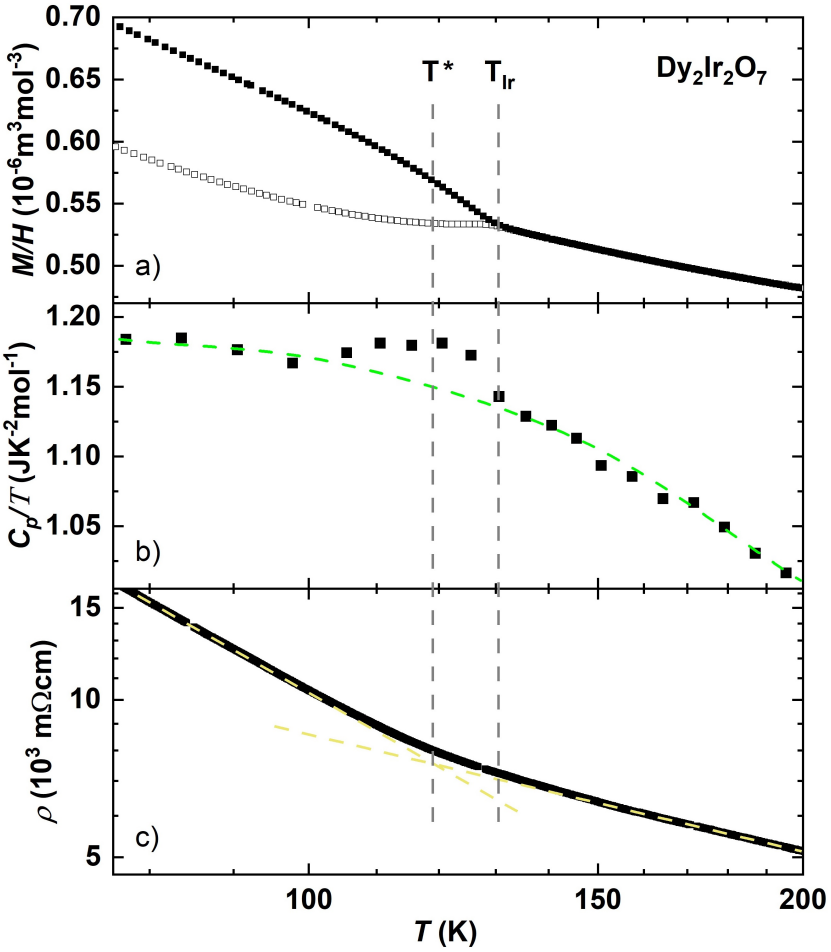

Figure 3.3: Comparison of magnetic susceptibility measured at 5 mT (open symbols stand for zero-field-cooled and full symbols for field-cooled regime) (a), specific heat (b), and electrical resistivity (c) measurements of $Dy_2Ir_2O_7$. The green dashed curve in (b) is a guide to the eye, highlighting the anomaly. Vertical lines represent the transition temperature T_{Ir} determined as the temperature of bifurcation of magnetization curves and $T^{\star}$ marking the intersection of yellow dashed lines in panel (c). The figure is adopted from Refs. [119, 120].

not clearly visible in the measured data.

To determine whether the MIT commences concurrently with AFM ordering at T_{Ir} or at (slightly) lower temperature is problematic. Nevertheless, MIT has never been observed above T_{Ir}, as it is also illustrated by studies of substituted iridates [64, 130] and isostructural $Cd_2Os_2O_7$ [128]. Within the Slater model, the MIT transition follows the magnetic transition [127]. That is, MIT is expected below T_{Ir}. On the contrary, the Mott model predicts that MIT will commence at or above T_{Ir}. Also, a continuous character of the MIT supports the Slater model [125], whereas the Mott model predicts a first-order transition connected to a more abrupt change in resistivity data [127]. Based on these observations, we ascribe the MIT transition in $A_2Ir_2O_7$ to the Slater mechanism rather than the Mott mechanism. We conclude that the AFM ordering is responsible for an opening of a gap at the Fermi level, which in turn leads to the transition to the insulating

state. Nevertheless, an unambiguous conclusion can hardly be made considering the semiconducting properties of the material in the paramagnetic state, as well as an ongoing scientific dispute regarding Mott and Slater mechanisms, e.g., in Sr_2IrO_4 [131, 132, 133], and the effect of Ir domain walls on transport properties discussed in the subsection 3.1.4.

3.1.3 Phase diagram

Discussing further the evolution of the Ir sublattice ordering temperature within the $A_2Ir_2O_7$ series, we completed the phase digram in Fig. 1.5. We synthesised and investigated, in the past understudied, heavy rare-earth $A_2Ir_2O_7$ members with A = Dy - Lu employing the preparation route described in section 2.1, including for the first time reported $Tm_2Ir_2O_7$ [57]. The finalised phase diagram containing the dependence of temperature T_{Ir} on the ionic radius of rare-earth A^{3+} ion is presented in Fig. 3.4.

$Pr_2Ir_2O_7$ does not magnetically order down to low temperature [60, 134]. Considering the insulating state in $A_2Ir_2O_7$ pyrochlores is induced by a Slater mechanism (discussed above), the $Pr_2Ir_2O_7$ member thus remains metalic (although with relatively high electrical resistivity). No signs of phase transition have been observed. Actually, the chiral-spin-liquid state has been reported for this compound [103]. All heavier members of the series reveal magnetic ordering at low temperature accompanied by a metal/semi-metal/semiconductor to insulator transition. A steep increase in T_{Ir} is observed coming from A = Pr (without ordering) through A = Nd (36 K) to A = Sm (120 K) member. $Pm_2Ir_2O_7$ has not been synthesised due to difficulties connected with radioactive Pm isotopes. Several studies attempted to bridge the gap among light A members by substituting Pr by the Nd element and Nd by Sm, respectively [135], or e.g. hole doping by substituting Eu by Sr [130] or even Ir by Ru substitution [64]. A smooth evolution of T_{Ir} was observed coming all the way from $Pr_2Ir_2O_7$ to $Sm_2Ir_2O_7$. Only a small increase of transition temperature with further increasing atomic number (or decreasing ionic radius) of rare-earth is observed for heavier members [60, 134]. T_{Ir}'s of the heaviest A members [116, 117], including $Tm_2Ir_2O_7$ [57], perfectly fit into the trend the lighter rare-earth iridates follow (Fig. 3.4).

Interpreting the phase diagram, the critical temperature is apparently independent of the magnetism/electronic properties of the rare-earth ions, at least for heavy members A = Sm - Lu. Taking into account T_{Ir} of $Lu_2Ir_2O_7$ and $Eu_2Ir_2O_7$ members with non-magnetic Lu and Eu ions [117, 136], the magnetic coupling between A and Ir sublattices is negligible at/above T_{Ir}. That is, the ordering temperature of Ir sublattice, and related insulating properties of $A_2Ir_2O_7$, are independent of the A ion and sublattice properties. Instead, the Ir sublattice ordering has an impact on the rare-earth sublattice ordering below T_{Ir}, as demonstrated in A = Nd, Tb, Ho and Yb iridates [27, 28, 30, 101]. In these members, the AIAO ordering of the Ir-sublattice acts on the A sublattice inducing corre-

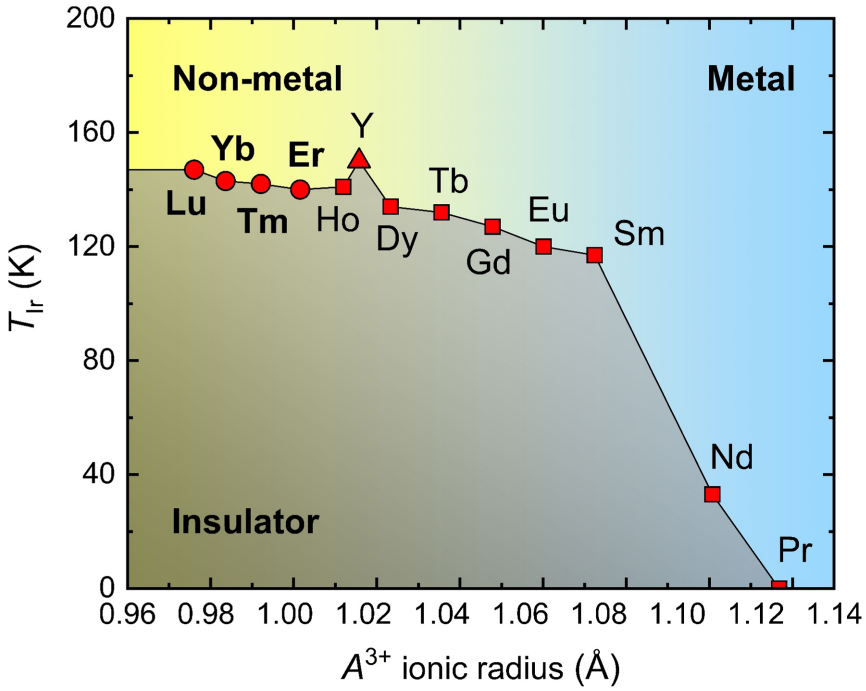

Figure 3.4: Phase diagram of $A_2Ir_2O_7$. The development of the transition temperature of magnetic ordering of Ir sublattice T_{Ir} on the ionic radius of rare-earth element A^{3+}; diagram finalised using our recent results. Compare the presented diagram with the incomplete phase diagram in Fig. 1.5 or Ref. [60]. The figure is adopted from Ref. [57].

sponding long-range AIAO ordering therein. At lower temperature, nevertheless, the exchange interactions between A moments prevail and another (component of) magnetic structure is realised (see section 3.2 for more details).

The evolution of T_{Ir} can be better understood from a structural viewpoint. The evolution of the crystallographic lattice parameter a and the single free fraction coordinate x_{48f} (of the 48f Wyckoff position of oxygen; the other atomic positions are constrained by the pyrochlore lattice symmetry) with a radius of A ion naturally leads to a change of interatomic distances and bond angles. Inspecting Table 3.1, T_{Ir} increases with the decrease in the overall size of the lattice. That is, the decrease in interatomic distances and the Ir-O-Ir angle ϕ influences the t_{2g}-block bandwidth of the iridium, resulting in a strong 5d-orbital overlap with oxygen ligand 3p-orbitals [88, 137] and, in turn, in an increase of T_{Ir}.

Magnetic ordering, T_{Ir}, MIT, and generally conducting properties of $A_2Ir_2O_7$ can be tuned by changing the structural parameters not only by substituting the elements on the A-site [138, 139, 140] or Ir site [64, 141, 142], but also by the application of external pressure. The application of pressure represents a clean way to study structural properties, avoiding the introduction of atomic disorder into the lattice by any partial site substitution. This is well demonstrated, e.g., in $Sm_2Ir_2O_7$ [143]. External and chemical pressure lead to a contrasting evolution of lattice parameter and trigonal distortion; change of bond angle ϕ, which affects the iridium bandwith; and magnetic moment anisotropy in the system.

Table 3.1: Selected parameters of $A_2Ir_2O_7$ pyrochlore iridates. A:Ir elements ratio; lattice parameter a, fraction coordinate x_{48f} and Ir-O-Ir bond-angle ϕ of the pyrochlore unit cell; temperatures T_{Ir}, $T^{\star}$, T_A and T_{LT} determined from magnetisation, specific heat and electrical resistivity data; activation energy Δ from fit to the Arrhenius law; total angular momentum of A^{3+} element J^A; effective magnetic moment for the A^{3+} free ion μ_{eff}^{A}; effective magnetic moment μ_{eff} and paramagnetic Curie temperature θ_p from fit of the magnetization data to Curie-Weiss law; μ_{eff}^{A-Lu} and θ_p^{A-Lu} from fitting the subtracted (A_2-$Lu_2Ir_2O_7$) magnetisation data. The data is adopted from our publications [57, 116, 117, 119, 120].

$A_2Ir_2O_7$	Dy	Ho	Er	Tm	Yb	Lu
A:Ir (%:%)	50(2):50(2)	50(2):50(2)	50(2):50(2)	50(2):50(2)	51(2):49(2)	51(2):49(2)
a (Å)	10.192(1)	10.184(1)	10.162(1)	10.135(1)	10.108(1)	10.104(1)
x_{48f}	0.334(2)	0.335(2)	0.334(2)	0.337(2)	0.336(2)	0.340(3)
ϕ	129(1)	129(1)	129(1)	128(1)	128(1)	126(1)
T_{Ir} (K)	131(2)	141(2)	140(2)	142(2)	143(2)	147(2)
$T^{\star}$ (K)	119(5)	121(8)	133(6)	117(7)	122(7)	113(10)
Δ (K)	218(1)	97(1)	237(1)	187(1)	375(1)	346(1)
T_A (K)	35(3)	n/i	30(2)	40(3)	30(3)	n/a
J^A	7.5	8	7.5	6	3.5	0
μ_{eff}^{A} (μ_B)	10.65	10.61	9.58	7.56	4.54	0
μ_{eff} (μ_B)	10.20(10)	n/i	9.12(4)	7.13(3)	4.05(3)	0.88(4)
θ_p (K)	-13(2)	n/i	-26(2)	-48(2)	-106(3)	-217(3)
μ_{eff}^{A-Lu} (μ_B)	8.90(10)	n/i	8.94(4)	6.89(4)	3.88(4)	n/a
θ_p^{A-Lu} (K)	-11(2)	n/i	-17(1)	-35(1)	-91(3)	n/a
T_{LT} (K)	1.6(2)	n/i	2.0(2)	–	2.7(2)	n/a

n/i - not investigated by the author

n/a - not applicable, Lu^{3+} is non-magnetic

Simultaneously, in $A_2Ir_2O_7$, the pyrochlore structure is stable up to high pressure, as illustrated by our recent work (subsection 2.1.4) [90]. The experiments under pressure were previously limited to light rare-earth pyrochlores. 10 GPa

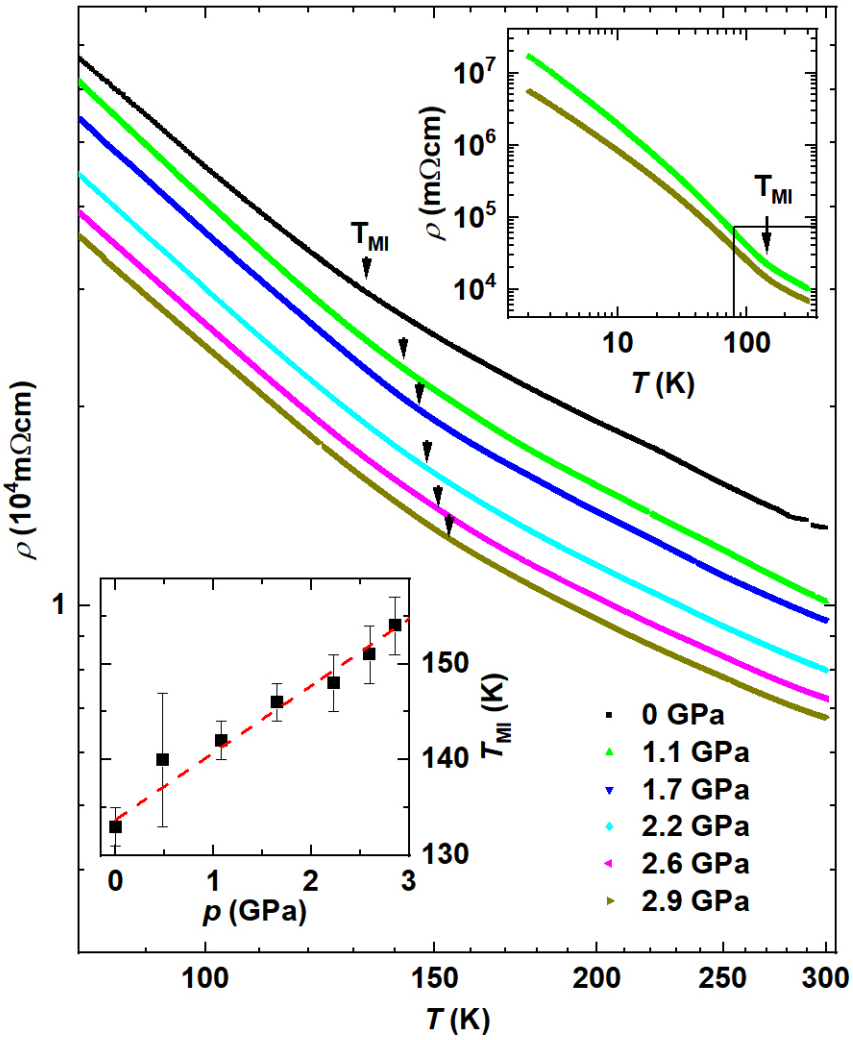

Figure 3.5: Pressure evolution of electrical resistivity of $Er_2Ir_2O_7$ zoomed on the metal-insulator transition. Temperature of the transition T_{Ir} (indicated by arrows) increases with the pressure application. Top inset shows the whole measured temperature region including the zoomed region in the fully logarithmic scale. Bottom inset shows the approximately-linear evolution of T_{Ir} under pressure. The figure is intended for our future publication (in preparation).

pressure applied to the $Nd_2Ir_2O_7$ compound causes a gradual decrease of T_{Ir} and suppression of MIT [135, 144]. Moreover, further increasing the pressure leads to the emergence of a new magnetic phase. In contrast, the transition temperature in $Eu_2Ir_2O_7$ decreases only slightly with increasing pressure up to 6 GPa, and a subtle increase is observed by further pressure application [59, 95].

The heavy rare-earth $A_2Ir_2O_7$ remained mostly uninvestigated from the viewpoint of the application of the external pressure. Very recently (to be published in the near future), we investigated $Er_2Ir_2O_7$ in pressure up to 3 GPa. Temperature of the transition from semi-metal to insulating state, T_{Ir}, increases almost linearly with the pressure application (see Fig. 3.5). Such an evolution is in a

perfect agreement with A cation phase diagram in Fig. 3.4. That is, T_{Ir} increases with the lattice contraction. Identical evolution of the phase transition in applied pressure is expected for all heavy rare-earth $A_2Ir_2O_7$ members. To verify this assumption, the pressure experiment is currently being performed on the $Lu_2Ir_2O_7$ member.

3.1.4 Antiferromagnetic domains and interfaces

The Ir magnetic moments in $A_2Ir_2O_7$ were reported to spontaneously order in the all-in-all-out structure (Fig. 1.2) below T_{Ir} [27, 28, 66, 101, 113, 114]. Importantly, in addition to the AIAO order, the time-reversal-symmetry-related all-out-all-in configuration is also realised. As the AIAO and AOAI configurations are equivalent from the energy point of view, they are both present in the bulk material below T_{Ir} and create respective domains. See Fig. 3.6 for illustration.

The interface between antiferromagnetic domains, the AIAO/AOAI interface, is formed by two types of moments, rotatable moments and frozen moments. Rotatable moments are weakly coupled with the respective domains and can be easily impacted by an external magnetic field. On the other hand, frozen uncompensated moments with the effective three-in-one-out arrangement (3I1O, or alternatively 1I3O) form a net ferromagnetic moment at the domain boundary and are strongly coupled to the domains [67]. Aligning and stabilising the antiferromagnetic domains' interfaces in $A_2Ir_2O_7$ is assumed to be done by a field of few mT, while the stabilised interfaces at lower temperature (below T_{Ir}) are robust against a field of several T [67, 145]. Therefore, these materials could serve as an ideal magnetic recording medium.

Electronic/conducting properties have been postulated to be distinct in the AIAO/AOAI domains and domain walls [146, 147]. The (strongly, Mott) insulating properties of AIAO domains are considered to be directly related to the magnetic moments' arrangement via the Slater mechanism [63, 67, 93, 148]. Contrary to the domains, AIAO/AOAI interfaces with disturbed magnetic order might reveal high metallic conductivity, as has been reported for $Nd_2Ir_2O_7$ [147]. Such distinct conductive properties of the domain interior and interfaces could be used to read the magnetically encoded information by an external electric field.

The formation and stability of ferromagnetic interfaces in pyrochlore iridates represent a very topical subject of research, opening a path to potential spintronic applications. In summary: These materials could enable magnetic recording of information applying a small magnetic field during crossing the transition temperature T_{Ir}. This information would be protected by the magnetic structure, domains, and frozen interfaces against the high magnetic field below T_{Ir}. Reading of the information would be then possible by an electric field, owing to the conductivity of domains (Mott insulator) and interfaces (high metallic conductivity) being significantly different. That is, magnetically encoded information will be read by an external electric field.

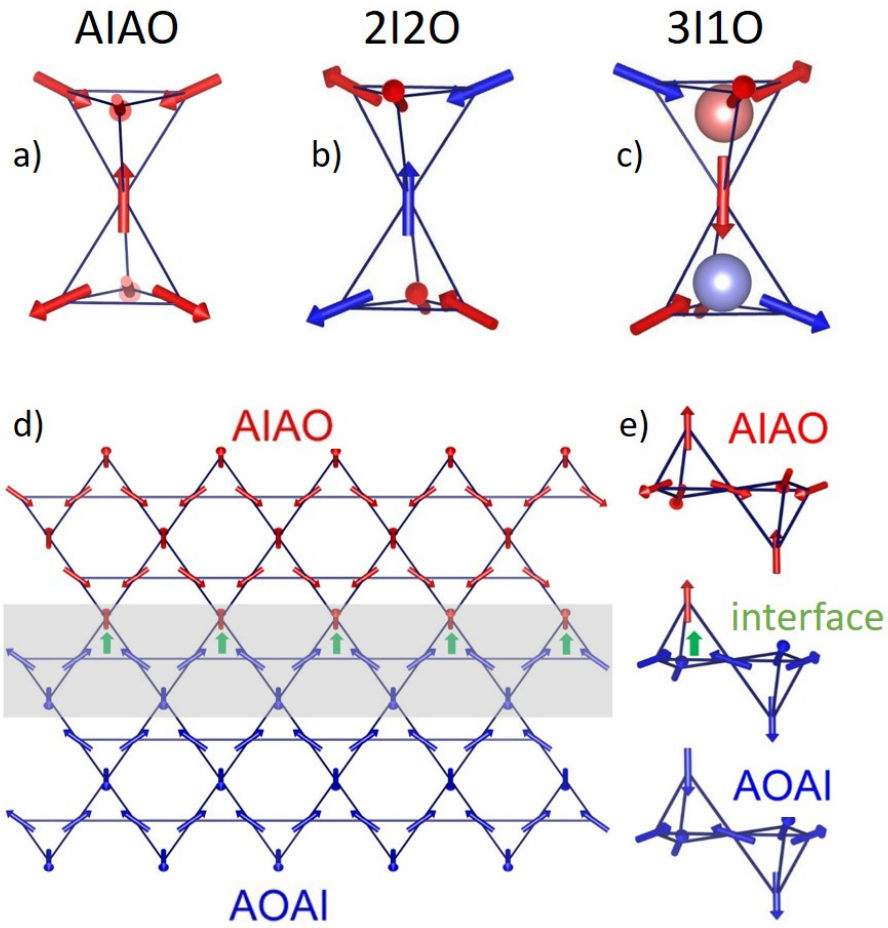

Figure 3.6: Types of magnetic moments' arrangement on the tetrahedron (a-c) and the model of the AIAO-AOAI domains' interface: 2D projection (d) and 3D scheme (e). Non-zero total magnetisation at the interface is represented by green arrows.

The magnetic ordering of the Ir sublattice can be manipulated, moreover, by rare-earth sublattice magnetism. Very recently, $Ho_2Ir_2O_7$ has been proposed to reveal a strong coupling between the magnetic monopoles (3I1O configuration) on the Ho sublattice and the ordered Ir moments at low temperatures [33]. By applying an appropriate external magnetic field, the magnetic monopole-like states on the Ho sublattice are induced. These states are coupled to the antiferromagnetic Ir domains and interfaces. That is, the AFM domains of Ir are manipulated by an external field via the rare-earth sublattice at low temperature. Such a mechanism of AFM domains manipulation would bypass the challenging problem of AFM domains switching!

To prove the presence of the domain interfaces, many experimental techniques have been/can be employed. Magnetisation measurement of bulk material, ideally single crystal (our recent unpublished work on $Lu_2Ir_2O_7$ single crystal), allows to prove the ferromagnetic component in antiferromagnetically ordered material. Cooling the sample through T_{Ir} in a zero magnetic field results in a random orientation of domain interfaces, giving zero total magnetisation. In contrast, cooling

the sample in non-zero magnetic field makes the domains and ferromagnetic interfaces (Fig. 3.6) preferably aligned along this field. Resulting uncompensated magnetisation can be observed in the data. Importantly, this ferromagnetic signal remains non-zero even after the external magnetic field has been removed. Simultaneously, further application of magnetic field of, at least, 7 T (and opposite -7 T) below T_{Ir} has no impact on the domains and interfaces structure. After removing this field, the original ferromagnetic signal is observed at zero external field. These effects are the best observable at low temperatures, sufficiently below T_{Ir}. However, the rare-earth sublattice of magnetic A elements influences the Ir ordering, and therefore the ferromagnetic interfaces, at least at lowest temperatures. As reported for $Ho_2Ir_2O_7$ [33], this interaction can be highly important for new generation of spintronic devices.

The magnetic domains, interfaces, and their magnetic and conductive properties can also be studied by means of other standardly used laboratory techniques, e.g., ac-susceptibility, magneto-transport measurements, Hall effect, and atomic/magnetic force microscopy [33, 63, 67, 92, 149]. Nevertheless, to obtain direct, microscopic information on the properties, advanced methods accessible in large-scale facilities must be employed, e.g., coherent X-ray scattering, X-ray magnetic circular dichroism, X-ray polarisation enhanced topography, or resonant micro-diffraction X-ray imaging [150, 151, 152]. We are currently proposing and performing microscopic experiments in large-scale facilities to shed light on the details of the magnetic ordering and conducting properties of $A_2Ir_2O_7$. Our efforts are currently aimed to unambiguously confirm the domain manipulation mechanism through the f-d interaction between rare-earth and iridium moments/sublattices; especially, proving it on the microscopic level, as well as imaging of domain structure (micro-diffraction X-ray experiment scheduled at ESRF Grenoble in the second half of 2024). Simultaneously, we continue to study bulk properties of synthesised single crystals (A = Nd, Er, Lu at the moment). The relevant publications will be submitted to scientific journals during the year 2024 and at the beginning of the year 2025.

3.2 Rare-earth sublattice ¶

Introduction to publications: **4., 7., 10., 11., and 12.**

In addition to the Ir sublattice magnetism (discussed in section 3.1), the physical properties of $A_2Ir_2O_7$ are governed by the electron configuration of rare-earth element. The rare-earth moments are subjected to the Ir molecular field and direct d-f coupling. Some $A_2Ir_2O_7$ members reveal induced AIAO magnetic order of the A sublattice, as evidenced by the neutron diffraction experiment in $Nd_2Ir_2O_7$ [101] and $Tb_2Ir_2O_7$ [28]. At low temperature, however, the exchange interactions between rare-earth moments become stronger, leading to a second

component of the magnetic moments. The ground state magnetic structure could then be, e.g., a superposition of AIAO and XY magnetic components. An antiferromagnetic coupling between the Ir and Sm moments and long-range ordering of the Sm moments were inferred in $Sm_2Ir_2O_7$ [153]. $Yb_2Ir_2O_7$ was reported to show a competition between AIAO and ferromagnetic ordering down to the lowest temperature [27].

Furthermore, together with the long-range Ir order, the induced A ordering, and the A-A magnetic correlations, the magnetic properties of $A_2Ir_2O_7$ iridates are defined by the A single-ion properties. The crystal field (CF) acts on the A cation ground state multiplet and removes its degeneracy. Contrary to Ir^{4+}, where the crystal field is order of magnitude stronger than spin-orbit coupling, the opposite applies for A^{3+} ion in crystalline environment. The physical properties of rare-earth compounds are thus determined mostly by crystal field effects, at least in the paramagnetic state. The crystal-field schemes of heavy rare-earth $A_2Ir_2O_7$ members have been reported for $Dy_2Ir_2O_7$ [7], $Ho_2Ir_2O_7$ [30] and $Yb_2Ir_2O_7$ [27]. Recently, we investigated crystal field schemes of the $Er_2Ir_2O_7$ [116] member and newly synthesised the $Tm_2Ir_2O_7$ member [62] and discussed them from the viewpoint of bulk properties and within the framework of other pyrochlore compounds.

3.2.1 Bulk properties

The crystal field scheme is essential to correctly understand the physical properties of the rare-earth compound, as well as its ground state. Below we present an introduction to our studies on two heavy rare-earth members of the $A_2Ir_2O_7$ series: $Er_2Ir_2O_7$ and for the first time synthesised $Tm_2Ir_2O_7$. Before giving an overview of our microscopic, inelastic neutron scattering, results, we discuss our low-temperature magnetisation and specific heat data which would support the CF schemes determination in section 3.2.2. Bulk data are also discussed for A = Dy and Yb members utilising the CF schemes determined previously by other authors [7, 27].

Magnetisation. Fitting the high temperature part of $A_2Ir_2O_7$ magnetisation to the Curie-Weiss formula led to the effective moment, μ_{eff}, and paramagnetic Curie temperature, θ_{p}, listed in Table 3.1. The value of μ_{eff} is slightly lower than the value expected for A^{3+} free ion $\mu_{\text{eff}}^{\text{A}}$. These values are, however, influenced by the Ir contribution to the magnetic response. Ir magnetisation is relatively small, as demonstrated in $Lu_2Ir_2O_7$ member with non-magnetic lutetitum; see our publication [117]. Nevertheless, subtracting the $Lu_2Ir_2O_7$ magnetisation data from other A members data and fitting the difference data to Curie-Weiss formula resulted in somewhat lower $\mu_{\text{eff}}^{A-\text{Lu}}$ values. Such result is not surprising and agrees well with previous results on light A members [154]. The contribution of the Ir sublattice is very similar in all members, strongly supporting the picture of the same magnetism, magnetic ordering and weak interaction between Ir and A sublattices, at least in the paramagnetic state.

The paramagnetic Curie temperature, θ_p, was fitted negative in all members. Its value decreases with increasing atomic number of A. The negative value of θ_p suggests antiferromagnetic correlations between magnetic moments. However, interpreting these values, one must be aware of the Ir contribution again. That is, the values for the $Lu_2Ir_2O_7$ member correspond to just Ir signal. Indeed, Curie-Weiss fits of corrected data resulted in somewhat lower θ_p^{A-Lu} values (Table 3.1). Small negative values of the paramagnetic Curie temperature without clear systematics were reported for lighter rare-earth iridates [154]. A = Er member thus fits to the previous results. A = Tm and Yb members reveal significantly larger values, which are unlikely to be connected to the A-Ir interactions. Of course, large values in these members could represent rather higher-energy CF levels, not giving much information on the ground state properties.

The antiferromagnetic correlations in $A_2Ir_2O_7$ are corroborated by the isothermal magnetisation measurements, showing no hysteresis in a sweeping magnetic field. The magnetisation value at high magnetic field (extrapolated as our measurements were performed in magnetic field just up to 7 T) exceeds the value expected for free A^{3+} ion for all members, except $Yb_2Ir_2O_7$. Such a result can be well understood considering the additional contribution of the magnetic moment of Ir^{4+} (can reach 1.74 μ_B for $S = 1/2$). $Yb_2Ir_2O_7$ exhibit a lower magnetisation (with apparent tendency to saturation) than expected for Yb^{3+} ion. The lower value of magnetisation is, nevertheless, consistent with the crystal field scheme determined from the inelastic neutron scattering experiment [27]. Actually, the measured value is higher just by the Ir contribution compared to CF calculations [57]. Indeed, the low value of magnetic moment in $Yb_2Ir_2O_7$ can be understood assuming the effective $S = 1/2$ ground state of Yb moments, similarly as in the $Yb_2Ti_2O_7$ analogue [155]. The mean field calculation revealed a strong Splayed ferromagnetic and a significantly weaker three-in-one-out (3I1O) components responsible for the reduced magnetic moment on Yb in this compound [27].

When the experimental magnetisation is compared with values calculated from the crystal field parameters (determined from inelastic neutron scattering data), a very good agreement is obtained for A = Er and Yb members (Fig. 3.7) [57, 116]. The corrected magnetisation data ($Lu_2Ir_2O_7$ data subtracted from $A_2Ir_2O_7$ data) perfectly overlap with the calculated curves. A worse agreement is observed for $Tm_2Ir_2O_7$, especially in the low temperature region (below 70 K) [62]. Although the Ir contribution was subtracted the same way as in other $A_2Ir_2O_7$ members, the effect of the molecular field of the Ir sublattice is most likely still playing a role. Attempts to add molecular field terms to the calculations, however, did not lead to a substantial improvement in compliance. Even a worse agreement comparing experimental magnetisation data to calculated curves from previously reported CF parameters was observed in $Dy_2Ir_2O_7$ [7, 120]. It was shown that the mean field approximation approach fails to properly explain the magnetisation data of this compound. Further studies, preferably on newly synthesised single crystals are necessary to shed light on intriguing properties of

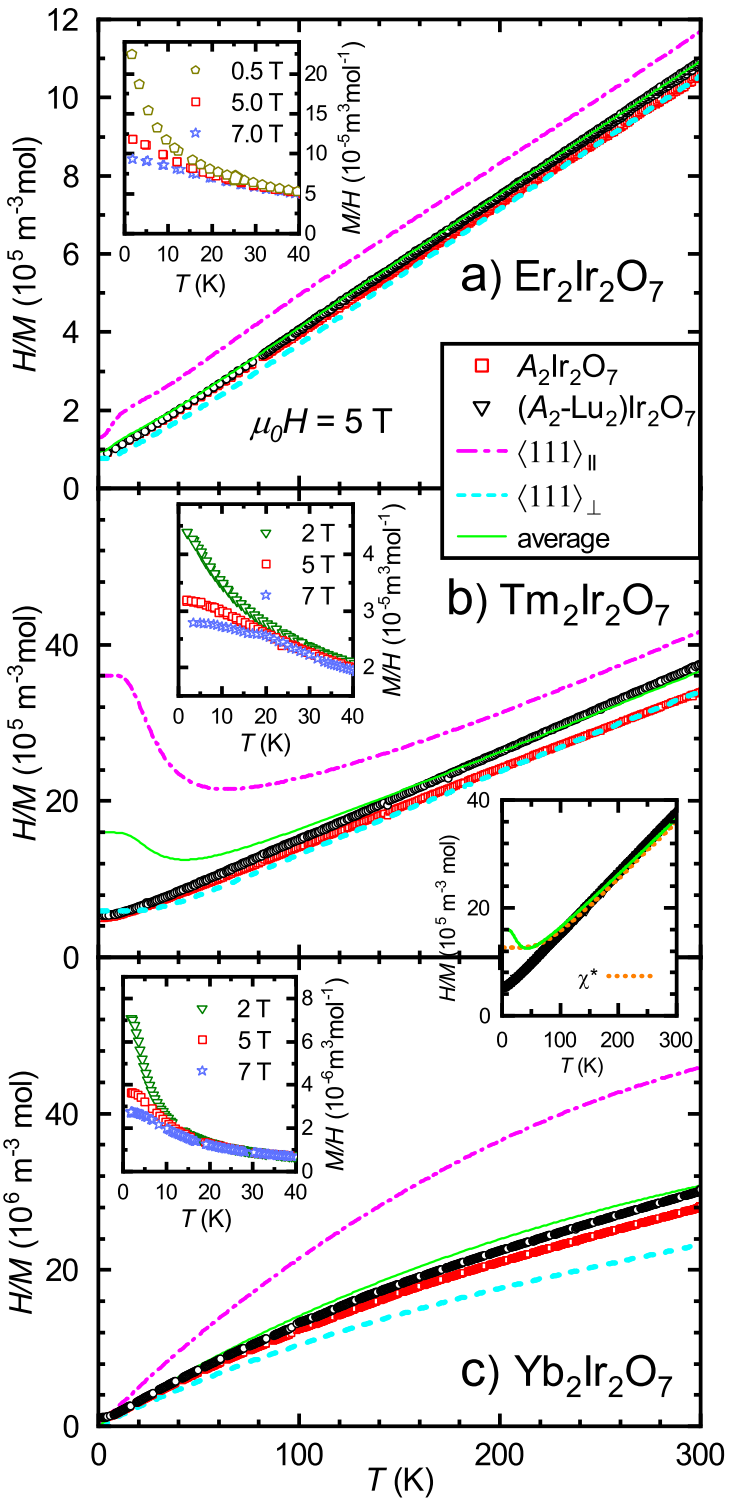

Figure 3.7: Inverse magnetic susceptibility, $\frac{H}{M}(T)$, of $A_2Ir_2O_7$ pyrochlores. The measured data and their difference subtracting Lu-member data are presented. The inverse susceptibility calculated from the CF parameters is compared with the measured data. The insets contain low-temperature $\frac{M}{H}(T)$ data in selected magnetic fields for respective iridates. The inset between panels (b,c) contains the $(Tm_2\text{-}Lu_2)Ir_2O_7$ data together with the average calculated inverse susceptibilities. Data was adopted from Refs. [57, 116].

this highly interesting material with fragmented magnetic monopole-like state [7].

Specific heat. The specific heat of $A_2Ir_2O_7$ iridates can be well understood as a sum of the (electronic,) lattice, Ir sublattice, and A sublattice magnetic contributions. Discussing the magnetic specific heat of solely rare-earth sublattice, the other contributions can be estimated by specific heat of $Lu_2Ir_2O_7$ (or alternatively $Eu_2Ir_2O_7$) member with non-magentic Lu (Eu) ion. Supposing that the mass of the A elements concerned and the interatomic distances in the lattice are not significantly different, the lattice contribution is almost the same in all members. The pure magnetic contribution of the Ir sublattice can be considered the same in $Lu_2Ir_2O_7$ and other members, most likely not only above T_{Ir}. However, the ordering temperature T_{Ir} slightly differs with A. That is, the anomaly in specific heat connected with the magnetic transition appears at (slightly) different temperatures for individual members. Therefore, the specific heat of the anomaly was roughly estimated and subtracted from the $A_2Ir_2O_7$ data (A = Dy, Er, Tm, and Yb). The specific heat connected with the interaction between A and Ir magnetic moments cannot be reasonably evaluated. Its strength is believed to be the same in all members above T_{Ir}. However, it could be significantly different at lower temperatures (see our discussion on the A-Ir sublattices interaction above, the beginning of the section 3.2). Fully aware of the uncertainties, the magnetic specific heat of A sublattice was calculated by subtracting $Lu_2Ir_2O_7$ data from other $A_2Ir_2O_7$ data sets [57, 116, 120]. Several magnetic anomalies were followed in the magnetic data.

The anomaly connected with an ordering of Ir sublattice was discussed in detail above (section 3.1.1). The lowest-temperature anomaly corresponding to the exchange interactions in most of the members will be discussed separately in the section 3.2.3. The remaining anomalies in (magnetic) specific heat are related to the CF excitations. A degeneracy of the ground state multiplet of A^{3+} ion is removed in crystalline environment. The point symmetry of the Wyckoff position of rare-earth in the pyrochlore lattice and its total angular momentum J^{A} are essential for the multiplet splitting. Dy^{3+}, Er^{3+}, and Yb^{3+} are Kramers' ions with half-integer J^{A}. The minimum degeneracy of the state is therefore two. Tm^{+3} with integer J^{A} can exhibit also singlet states. The point group symmetry of the rare-earth element in the $A_2Ir_2O_7$ pyrochlore structure (16d position, see Fig. 1.4) is not cubic (which would lead to higher degeneracy), but trigonal ($D_{3\mathrm{d}}$, $\bar{3}m$). The ground state multiplet of $A_2Ir_2O_7$ in the pyrochlore lattice will thus be split into 8 doublets for A = Dy and Er, 5 singlets and 4 doublets for A = Tm, and 4 doublets for A = Yb. The energies of the respective states were measured employing inelastic neutron scattering techniques by us or other authors [7, 27, 57, 116]. Comparing the Shottky specific heat calculated from measured CF energies with estimated magnetic contribution to specific heat leads to the perfect agreement (see Fig. 3.1). Simultaneously, the magnetic entropy calculated from this magnetic specific heat well illustrates the degeneracy of individual CF states (see insets in Fig. 3.1). That is, the slope of the temperature evolution of

magnetic entropy changes at the entropy values corresponding to the CF levels and their multiplicity. Of course, this agreement is observed only for lower-energy excitations, as the specific heat data were measured just up to 300 K ($E = k_B T$).

3.2.2 Crystal field schemes, inelastic neutron scattering

Together with the long-range Ir order (see chapter 3.1), the induced A order (of magnetic rare-earth ions) and the A-A magnetic correlations (see section 3.2.3), the low-temperature properties of $A_2Ir_2O_7$ are defined by the A single-ion properties. The crystal field (CF) acting on the A cation in the pyrochlore lattice environment has been systematically studied by inelastic neutron scattering for $Dy_2Ir_2O_7$ [7], $Ho_2Ir_2O_7$ [30], and $Yb_2Ir_2O_7$ [27], and discussed in the framework of bulk properties of these iridates [34, 57, 120]. In parallel with these studies, we investigated the crystal field schemes in the last two heavy rare-earth members of the family: $Er_2Ir_2O_7$ [116] and newly synthesised $Tm_2Ir_2O_7$ [57, 62]. Our results, determination and parametrisation of the crystal field in A = Er and Tm iridates, have completed the knowledge on the CF states and effects in the family of pyrochlore iridates, and those results are introduced below.

$Er_2Ir_2O_7$. The inelastic neutron scattering experiment on $Er_2Ir_2O_7$ revealed several energy regions containing a non-dispersive magnetic signal. Three transitions between ground state and respective excited states were observed below 20 meV. A much broader magnetic signal, consisting of several excitations, was found at higher energy between 60 and 75 meV. Finally, only a weak magnetic excitation was traced at 90 meV. No magnetic signal was observed at higher energy. The Q-dependence of observed excitations unambiguously proved their magnetic origin; the signal became weaker with increasing Q following well the Q-dependence of magnetic formfactor of erbium. The magnetic origin of excitations was further documented by the temperature evolution of their intensity; the intensity decreased with increasing temperature as a result of the thermal population of individual energy levels. In addition, thermally populated energy levels allow both (de-)excitations in neutron-energy-gain (system-energy-loss) part of the spectrum, and excitations between excited states. New magnetic excitations were observed in Q-E spectra measured at higher temperature. A high-enough temperature causes all states being (partly) thermally populated and all types of (de-)excitations being manifested.

The CF excitations in $Er_2Ir_2O_7$ are well described within a standard crystal field model. Er^{3+} ions ($J = \frac{15}{2}$) occupy the Wyckoff position 16d in $Fd\bar{3}m$ space group. The point group symmetry of this position is not cubic, but trigonal: D_{3d}. The crystal field Hamiltonian in Stevens notation is hence written as follows:

$$\hat{H}_{CEF} = B_2^0\hat{O}_2^0 + B_4^0\hat{O}_4^0 + B_4^3\hat{O}_4^3 + B_6^0\hat{O}_6^0 + B_6^3\hat{O}_6^3 + B_6^6\hat{O}_6^6, \qquad (3.1)$$

where B_n^m are the crystal field parameters and O_n^m stand for Steven's operators representing the erbium 4f-shell. The CF model implies a splitting of the Kramers

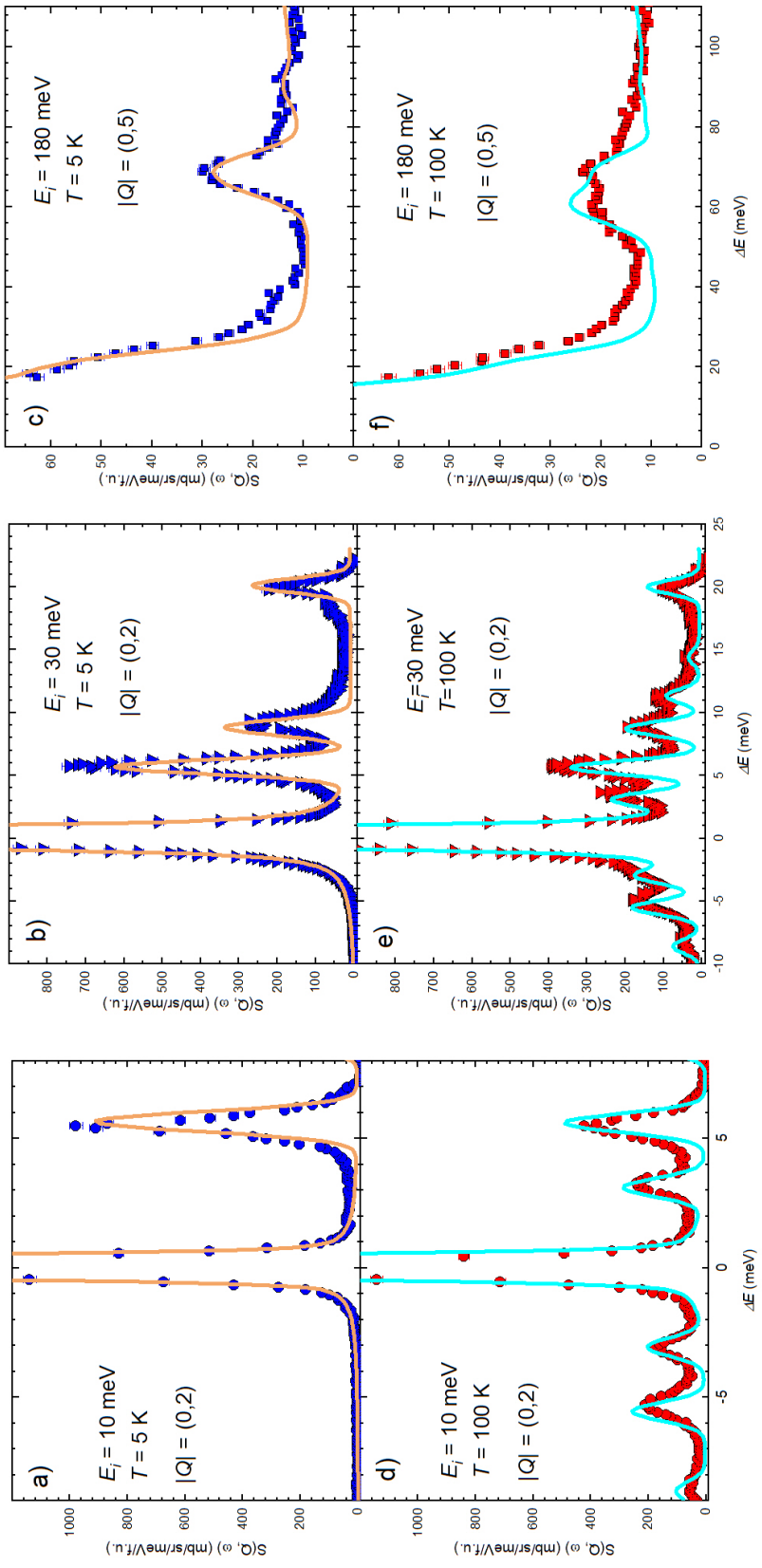

Figure 3.8: Q-cuts of inelastic neutron scattering E-Q maps of $Er_2Ir_2O_7$ measured at 5 and 100 K. The solid lines represent the fit to the CF Hamiltonian resulting in CF energies and parameters listed in Table 3.2. The figure is adopted from Ref. [116].

Er^{3+} 16-times (= $2J$+1) degenerate ground-state multiplet into 8 doublets. In the Q-E spectra, seven transitions from the ground state are expected in $Er_2Ir_2O_7$ at low temperature.

All 7 CF excitations were identified in $Er_2Ir_2O_7$ spectra. However, not all excitations were well visible in the measured data (see Fig. 3.8 for illustration). Three low-energy excitations were clearly observed, as the shape of respective well-pronounced Q-cut peaks was consistent with a single excitation. The high-energy region contained at least two relatively broad magnetic peaks in the region between 60 and 75 meV, just 4 meV apart. The highest energy peak at 90 meV was also broad and of weak intensity. Counting the excitations, one excitation was still missing compared to the CF model. The formerly missing signal was eventually found within the 65 meV peak, which, in reality, consisted of two peaks (see the list of energies in Table 3.2). Distinguishing the two excitations in our data is very problematic due to resolution limitation. Nevertheless, fitting the data considering these excitations close in energy, the agreement between measured magnetisation and magnetisation calculated from refined CF parameters (see the discussion below), and similar excitation spectra of other Er-based pyrochlores [156] confirm the presence of three peaks in a broad signal between 65 and 70 meV.

In fact, a striking resemblance of the energy scheme of $Er_2Ir_2O_7$ and other Er-based pyrochlores, especially $Er_2Pt_2O_7$, is observed [156]. The similarity of CF schemes documents the fact, that magnetism of Ir^{4+} ion has no/negligible effect on CF scheme of Er-based pyrochlores. Differences in respective CF schemes originate just in (slightly) different interatomic distances and bond angles in the pyrochlore lattice by substituting a B-site cation. The atomic radii of Ir and Pt differ negligibly, which is consistent with very similar crystallographic parameters and therefore, similar CF schemes.

The experimental data was fitted to the model CF hamiltonian (equation 3.1) using the previously reported CF parameters for $Er_2Pt_2O_7$ [156] as initial values. First, the fit of the lowest temperature data was done, combining three energy spectra measured with initial neutron energies 10, 30 and 180 meV. Refined parameters were used as starting values to fit the data measured at all temperatures. That is, the data including the excitations from thermally populated CF states was also fitted using the single CF model. The fitted 5 K and 100 K spectra are presented in Fig. 3.8 and the values of final CF energies and CF parameters are listed in Table 3.2.

The determined CF scheme was tested with respect to the measured specific heat and magnetisation data. The Schottky contribution to the specific heat calculated from CF energies perfectly agrees with the measured data (Fig. 3.1). Of course, the CF scheme is also fully consistent with the temperature evolution of magnetic entropy. The first three CF excitations are followed on both the change of slope of the entropy curve and the entropy value at temperatures corresponding to the CEF energies ($E = k_B T$). Similarly, good consistency of magnetisation

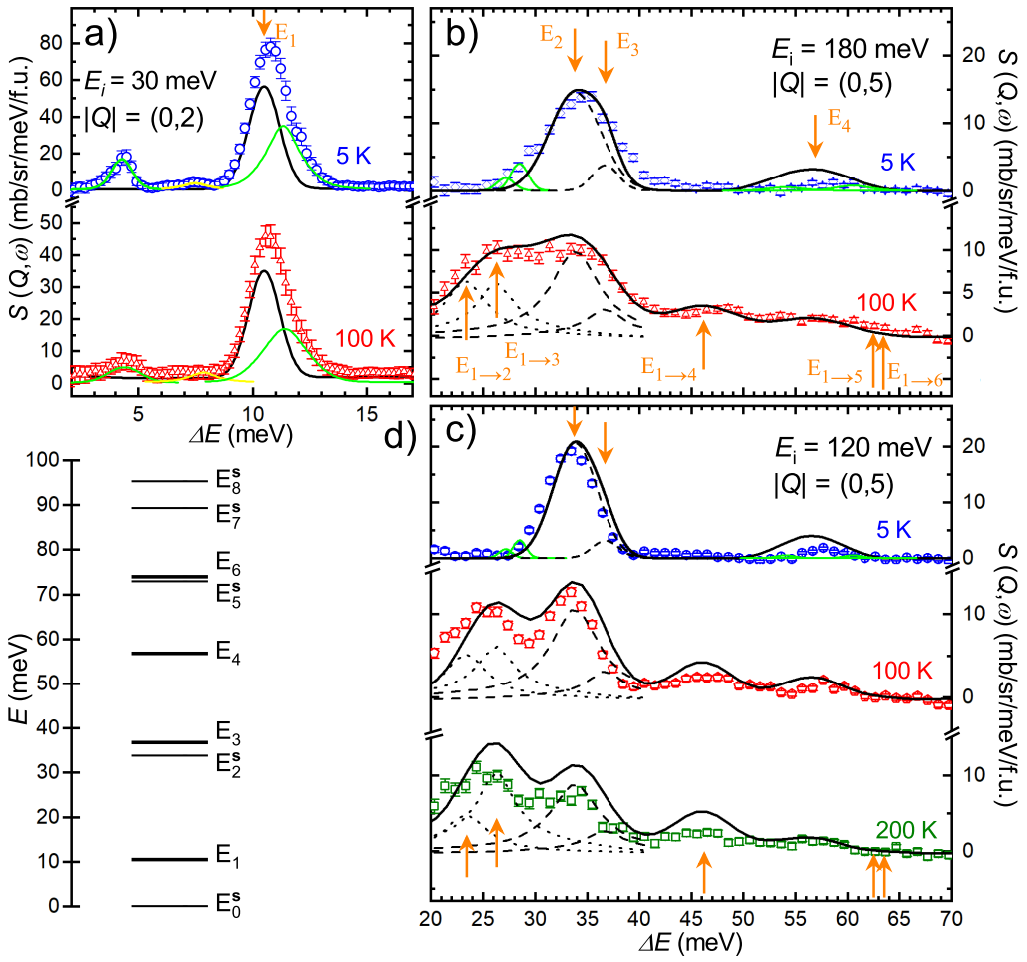

Figure 3.9: Low-Q cuts of the difference (magnetic) $Tm_2Ir_2O_7$ spectra. Black lines represent the fits to the CF Hamiltonian, resulting in the CF parameters listed in Table 3.2. Arrows mark the eigenenergies listed also in Table 3.2 and depicted in panel (d), as well as the energies of excitations between thermally populated levels (arrows from below the datasets). The excitations related to the impurity Tm_2O_3 phase are fitted as well: green line for the thulium 24d Wyckoff site [160] and yellow line for a single peak identified for the 8b site [161]. The figure is adopted from Ref. [62].

data with magnetic susceptibility calculated from CF parameters is observed in Fig. 3.7. The susceptibility was calculated for two local crystallographic directions: along and perpendicular to the local (tetrahedron) <111> axes. The average value in green perfectly fits the magnetisation data above T_A. Further details can be found in our recent publications [57, 116].

$Tm_2Ir_2O_7$. As for $Tm_2Ir_2O_7$ iridate, the determination of CF scheme was more problematic than in the Er member due to: (i) Tm^{3+} is not Kramers' ion; that is, not only doublets, but also singlet CF states are expected; (ii) several CF excitations are of low intensity; (iii) energy resolution at high energy is poor, while several excitations have relatively high energy; and (iv) investigated $Tm_2Ir_2O_7$ sample contained several percents of unreacted Tm_2O_3 oxide. Therefore, we performed the inelastic neutron scattering experiment not only on $Tm_2Ir_2O_7$, but

also on $Lu_2Ir_2O_7$ serving as a non-magnetic analogue (magnetic iridium is present in both analogues). Lattice excitations (phonons; and any signal connected with Ir - expected at higher energy [137, 157, 158]) are supposed to be the same in both analogues. Subtracting the A = Lu data from A = Tm data allowed us to obtain magnetic spectra of $Tm_2Ir_2O_7$.

Due to the secondary phase in the investigated sample, the magnetic spectra contained not only CF excitations of $Tm_2Ir_2O_7$, but also those of Tm_2O_3. Thulium oxide crystallises in a cubic structure (space group $Ia\bar{3}$) with Tm cations occupying two non-equivalent positions 8b and 24d [159]. Point group symmetries of the two Wyckoff positions $C3i$ and $C2$, respectively, lead to two sets of CF excitations. The corresponding CF schemes were previously investigated. However, only the CF scheme connected with the 24d position was unambiguously determined [160]. Excitations connected with the 8b position were studied only indirectly, investigating a magnetic part of the specific heat data of Tm_2O_3 [161]. Finding and describing the excitations of Tm_2O_3 allowed us to observe several non-dispersive magnetic excitations of $Tm_2Ir_2O_7$.

The free Tm^{3+} ion with total angular momentum $J = 6$ has a ground state of $2J+1 = 13$ times degenerate. The D_{3d} point symmetry of the Tm position in the pyrochlore lattice and the related crystal field removes the degeneracy. The ground state multiplet is supposed to split into four doublets and five singlets. Eight excitations are expected in $Tm_2Ir_2O_7$. However, only 4 out of 8 excitations were observed in magnetic spectra (see Fig. 3.9). Determining the CF scheme, that is, refining six CF parameters, utilising only four excitations, would lead to dubious results. Therefore, we considered following points in our analysis:
(i) The model CF schemes of $Tm_2Ir_2O_7$ were calculated by rescaling the CF parameters obtained by the previous INS studies on neighbouring $Er_2Ir_2O_7$ [116] and $Yb_2Ir_2O_7$ analogues [27]. Importantly, two calculated schemes (see Table 3.2) are considerably different. The degeneracy of respective excited states is not the same in two models; doublet and singlet states in the schemes have different ordering following the energy. Also, the calculated values of energy considerably differ from experimental values with the $Yb_2Ir_2O_7$-based model, leading to much worse agreement with measurement. See our publication [62] for more details regarding two models differences.
(ii) Thermal population of CF levels allows for new inter-levels excitations as discussed above. That is, the excitations between lower-energy and higher-energy states can be observed as new excitations at relatively low energy, where the instrumental resolution allows for unambiguous identification of the magnetic signal. Inspecting new excitations gave us a good idea on the energies of higher-energy excitations, which cannot be identified in magnetic spectra due to their low intensity and poor instrumental resolution. Fitting a larger number of peaks in the spectra permitted for a more reliable determination of the crystal field parameters in $Tm_2Ir_2O_7$.
The simultaneous fitting of all temperature and initial energy data sets using a

single model (equation 3.1) resulted in the CF parameters listed in Table 3.2. The fit of the inelastic neutron scattering data is presented in Fig. 3.9, together with secondary phase excitations (green and yellow curves).

Table 3.2: The crystal-field parameters in Stevens notation and corresponding CF eigenenergies of $A_2Ir_2O_7$ compounds with A = Er, Tm and Yb. Model $Tm_2Ir_2O_7$ schemes derived by scaling the CF parameters of $Er_2Ir_2O_7$ [116] and $Yb_2Ir_2O_7$ [27] by Stevens factors (Er to Tm) and transforming the Wybourne CF parameters into Stevens notation (Yb to Tm) are provided as well. Singlet states are marked (s); the other levels are doublets. Further details are provided in text and Refs. [62, 116].

$A_2Ir_2O_7$	Er	Tm^{Er}	Tm	Tm^{Yb}	Yb
B_2^0 (10^{-2} meV)	7.456	29.670	18.277	36.670	115.240
B_4^0 (10^{-3} meV)	1.886	6.949	5.057	5.265	-55.840
B_4^3 (10^{-2} meV)	1.148	4.228	3.184	5.602	-59.420
B_6^0 (10^{-6} meV)	9.720	-26.330	-31.260	-29.470	2333.770
B_6^3 (10^{-4} meV)	-1.473	3.981	3.873	7.166	-567.570
B_6^6 (10^{-4} meV)	2.418	-6.554	-5.890	-4.398	348.380
E_0 (meV)	0	0(s)	0(s)	0(s)	0
E_1 (meV)	5.581	8.733	10.467	13.733	77.780
E_2 (meV)	8.684	37.646	33.827(s)	24.359(s)	111.349
E_3 (meV)	19.937	37.935(s)	36.734	32.418	151.680
E_4 (meV)	64.149	65.429	56.559	60.740	–
E_5 (meV)	65.391	83.915	72.768(s)	71.550(s)	–
E_6 (meV)	70.214	86.147(s)	73.868	75.259	–
E_7 (meV)	89.935	117.112(s)	89.239(s)	110.438(s)	–
E_8 (meV)	–	121.177(s)	95.250(s)	113.829(s)	–

Comparing the measured magnetisation and specific heat data with values calculated from refined CF parameters and eigenenergies shows reasonable agreement. See Fig. 3.1 and Fig. 3.7 for illustration, and section 3.2.1 for detailed discussion. Importantly, the accordance between macroscopic data and calculated values from the CF parameters strongly supports our interpretation of the INS data; although not being able to unambiguously confirm the highest-energy excitations.

The refined CF parameters of $Er_2Ir_2O_7$ and $Tm_2Ir_2O_7$ were also compared with the parameters of other $A_2Ir_2O_7$ pyrochlore iridates [7, 27, 30]. We highlight a noticeable systematics within the series. All iridates reveal the values of the CF parameters of the same signs and similar magnitudes. On the other hand, the values do not follow, for instance, the contraction of the 4f-radial-wave function [162]. Most likely, this fact reflects the small difference in hybridisation between the rare-earth 4f-wave function and 2p-states of eight nearest-neighbour oxygen

anions in the pyrochlore lattice. Similar systematics is observed for the sister $A_2Ti_2O_7$ series [163]. We emphasise that the INS study of $Tm_2Ti_2O_7$ revealed the first CF excitation at 10 meV [164]. Unfortunately, no other excitations were reported. Nevertheless, by scaling the CF parameters of other titanates, the CF scheme of $Tm_2Ti_2O_7$ can be estimated [163]. Importantly, the estimated $Tm_2Ti_2O_7$ scheme and the determined $Tm_2Ir_2O_7$ scheme are generally the same. The same excitation scheme, similar excitation energies, as well as good agreement in comparing the CF schemes of other titanates and iridates [27, 57, 116, 163] strongly support our refinement of the INS data and the final set of CF parameters listed in Table 3.2.

3.2.3 Low-temperature magnetic properties

Although the Ir sublattice ordering and induced molecular field play a significant role in the ground state properties of $A_2Ir_2O_7$, similarly as crystal field effects, the low temperature behaviour is governed also by exchange interactions (generally superexchange through the oxygen ligands) between rare-earth moments. The low-temperature magnetic properties of most of the light rare-earth members have been studied thoroughly, while few results had been published on the heavy rare-earth iridates. Commencing our work on the pyrochlore iridates we aimed at filling the gap and focused primarily on heavy $A_2Ir_2O_7$, leading also to substantial low-temperature results [57, 62, 116]. Together with other authors [27, 33, 165], we completed the overall characterisation of these heavy rare-earth pyrochlores in the last three years.

$Pr_2Ir_2O_7$ shows a metallic behaviour down to low temperature (as discussed in the section 3.1), where a spin liquid state emerges [103, 166]. The AIAO ordering of the Ir moments and the d-f interaction induced AIAO ordering of the Nd moments were revealed in $Nd_2Ir_2O_7$ [115, 167]. Simultaneously, a reduced magnetic moment on Nd was observed and ascribed to strong quantum fluctuations [101]. All-in-all-out magnetic ground state and significant electronic correlations were reported for $Sm_2Ir_2O_7$ [113]. Europium in $Eu_2Ir_2O_7$ has no magnetic moment; therefore, only the AIAO ordering of iridium moments was reported [94, 136]. Quasi-isotropic magnetic exchange between gadolinium moments in $Gd_2Ir_2O_7$ leads to more complex situation, when, beside the AIAO ordering another non-collinear arrangement of magnetic moments (Palmer-Chalker correlations) are realised [165]. Both Ir and Tb sublattices order magnetically (AIAO ordering) in $Tb_2Ir_2O_7$ just below T_{Ir} [28]. The ordering of Tb moments is induced by ordering of the Ir sublattice immediately below transition temperature! Another component of the magnetic moment, the XY component, related to the interaction between Tb moments, is manifested at a significantly lower temperature (10 K) [28]. In $Dy_2Ir_2O_7$, the fragmented monopole crystal state is realised [7]. The antiferromagnetic order and a Coulomb-phase spin-liquid were observed simultaneously. The fragmentation of magnetic moments under the influence of a local

staggered field was revealed for spin-ice $Ho_2Ir_2O_7$ [168].

Focussing on the heaviest rare-earth $A_2Ir_2O_7$ members, we discuss them in the framework of determined crystal field schemes and measured bulk and microscopic properties. The low-temperature part of specific heat of A = Er and Yb members is dominated by a pronounced anomaly at T_{LT} (Fig. 3.10 and Table 3.1). The magnetic origin of the anomaly, attributed to the correlations between A magnetic moments, is supported by no similar anomaly in $Lu_2Ir_2O_7$ data (as well as $Tm_2Ir_2O_7$ data). A comparison of the specific heat of magnetic A and non-magnetic Lu members illustrates that the anomaly contains only very weak electronic, lattice and iridium sublattice contributions. The crystal field origin of the anomaly is excluded based on above presented inelastic neutron scattering data and determined CF schemes.

The broad anomaly is connected with the magnetic entropy reaching the value of R.ln(2) at the anomaly high-temperature onset, see Fig. 3.10, well corresponding to the Zeeman splitting of the ground state doublet. The shape of the anomaly is not consistent with a standard second-order magnetic phase transition, but rather with short-range magnetic correlations. No long-range magnetic ordering was inferred from the neutron diffraction data on $Er_2Ir_2O_7$, which did not show any magnetic reflections down to low temperatures [61]. On the other hand, the low-temperature magnetisation data show a bifuration between ZFC and FC magnetisation below 0.5 K, suggesting a rise of the magnetic ordering. Similarly in $Yb_2Ir_2O_7$, where a development of ferromagnetic peaks, in addition to a weak AIAO component, was observed at sub-kelvin temperatures [27].

The low-temperature magnetic correlations in both A = Er and Yb members are well consistent with a shift of the specific heat anomaly, and related magnetic entropy, with an applied magnetic field to higher temperatures (Fig. 3.10). Importantly, only a small shift of the anomaly is observed in the low magnetic field. Increasing the applied field above 1 T leads to a more pronounced shift of magnetic entropy.

A completely different evolution of low-temperature specific heat is followed in $Tm_2Ir_2O_7$. No anomalies are revealed at low temperature. That is, no anomalies are observed in addition to those connected with CF excitations in this compound. The specific heat of $Tm_2Ir_2O_7$ and $Lu_2Ir_2O_7$ differ only slightly, by CF contribution only. No magnetic ordering is, nevertheless, expected in this member due to the non-magnetic ground-state singlet of Tm (see subsection 3.2.2). In fact, our powder neutron diffraction experiment on $Tm_2Ir_2O_7$ down to 0.2 K showed only an ambiguous magnetic signal at a single scattering angle [62]. The application of a magnetic field acts on the first CF excited doublet and splits it, leading to small change of specific heat at low temperature.

Magnetoresistance measurements at low temperature reveal a decrease of electrical resistivity with applied magnetic field for all investigated $A_2Ir_2O_7$ members [119]. The decrease of resistivity is substantial for A = Dy member, reaching approximately 8% of its zero-field value at 2 T. A = Lu, at the end of the series,

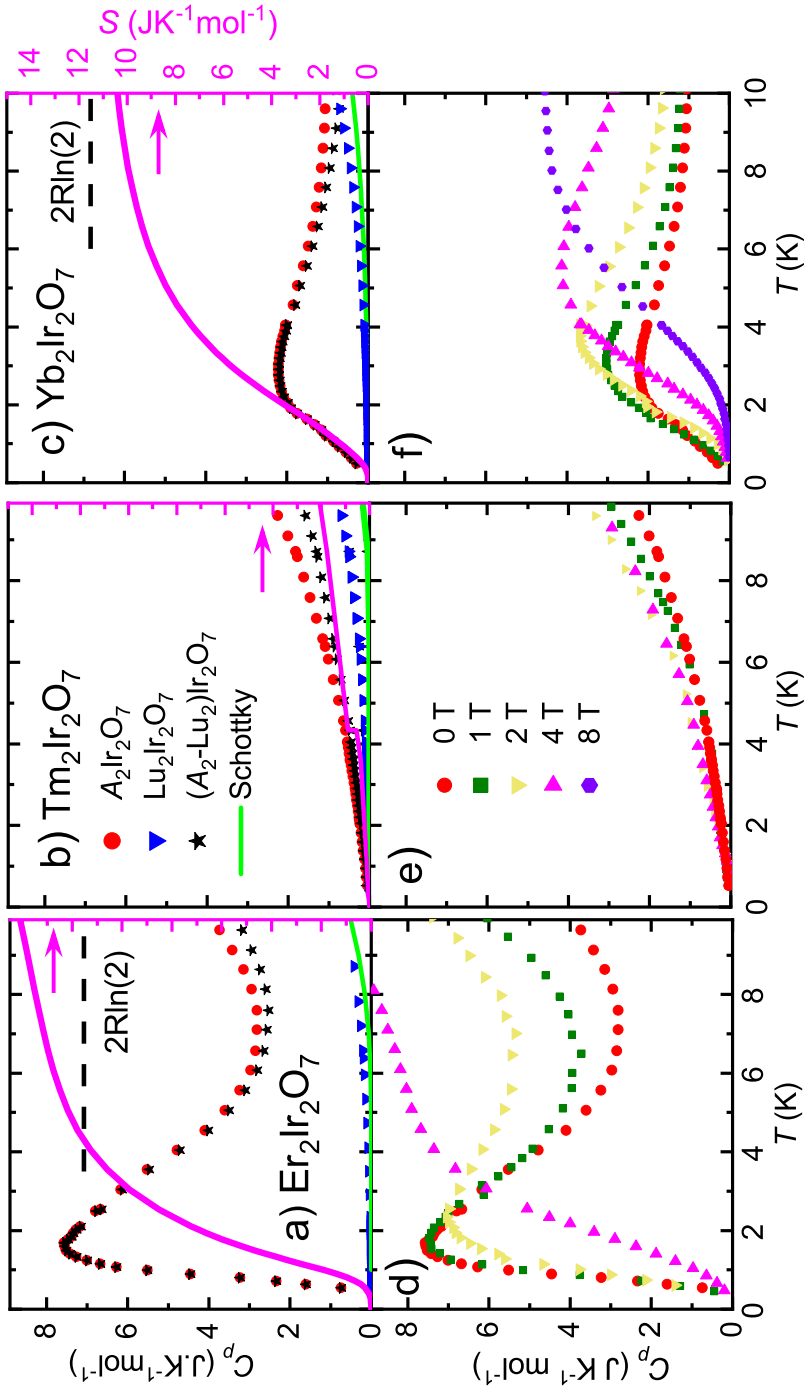

Figure 3.10: Low-temperature part of specific heat data measured on $A_2Ir_2O_7$. Panels (a-c) contain specific heat of A and Lu members and their difference. The Schottky contribution to the specific heat calculated from the CF energy scheme is shown as well. On the right axis, the entropy calculated from $(A_2\text{-}Lu_2)Ir_2O_7$ data is presented. Panels (d-f) show the temperature evolution of the specific heat in the applied magnetic field. The figure is adopted from Ref. [57].

reveals only small negative magnetoresistance (within 1%). The other members' resistivity drops fit in between the two extremes, while it seemingly develops with the atomic number of rare-earth element or alternatively with a size of magnetic moment on A^{3+} cation. In fact, the magnetoresistance is tightly connected with

the exchange coupling between A and Ir ions, which is strongly influenced by the rare-earth magnetic moment. Two important observations were made. First, no hysteresis was detected between magnetoresistance curves measured with increasing and decreasing magnetic field. Second, the effect of magnetic field becomes weaker with an increasing temperature. At 10 K, a comparable electrical resistivity was observed in the zero and 9 T field. Above 15 K, there is no difference followed in electrical resistivity measured in zero field and high magnetic field.

The application of a magnetic field affects the electrical resistivity of heavy rare-earth iridates solely at low temperature, where the magnetic correlations between A moments are strong. At higher temperature, hardly detectable change of the electrical resistivity with applied magnetic field could be traced. It could support the scenario discussed above (section 3.1.4) on ferromagnetic domain interfaces on the Ir sublattice. No change of magnetoresistance at higher temperature shows the robustness of interfaces below T_{Ir}. At lower temperatures, the interaction between the two sublattices becomes stronger, the interactions between rare-earth moments set in, and the electrical resistivity is strongly influenced by an applied magnetic field. The insulating state of $A_2\mathrm{Ir}_2\mathrm{O}_7$ related to the antiferromagnetic ordering of Ir sublattice is influenced by the magnetic field via the d-f interaction between Ir and A moments. That is, the magnetic field affects the A moments (possibly magnetic monopole-like states [33]), they couple with Ir moments via d-f interaction, and the Ir domain-interface structure is changed, leading to a significantly reduced electrical resistivity. This assumption is further supported by non-magnetic lutetium $\mathrm{Lu}_2\mathrm{Ir}_2\mathrm{O}_7$ data showing no such drop in the electrical resistivity upon application of a magnetic field.

4. Global and local structures in $A_2Zr_2O_7$ zirconates ¶

Introduction to publications: **1., 3., 5., 6., 13., 14., 15., 17.**

In addition to heavy rare-earth iridates $A_2Ir_2O_7$, we focussed in our work on physical properties and mainly details of the crystal structure of $A_2Zr_2O_7$ zirconates. These compounds remain in the forefront of scientific interest within the condensed matter community not only for their frequently complex electronic properties [27, 33, 169, 170], similar to their Ir counterparts, but also for their application potential. Heavy $A_2Zr_2O_7$ are expected to serve as solid oxide fuel cells due to their high ionic conductivity [49, 171], thermal barrier coating [50, 172], as negative-temperature-coefficient thermistors [173], or as nuclear waste storage [51, 174]. Considerable attention has been aimed at finding materials with improved thermomechanical properties and higher ionic conductivity. All these properties are naturally closely connected to details of their crystal structure.

The light rare-earth $A_2Zr_2O_7$ compounds were reported to crystallise in the pyrochlore structure; isostructural to the $A_2Ir_2O_7$ counterparts. Heavy rare-earth members of the series, in contrast, adopt the defect-fluorite structure [175, 176]. See subsection 1.2.1 for details on these crystal structures, their transformations and interconversions. Moreover, thermodynamic drive for A/Zr mixing in heavy A members, induced by more similar ionic radii of A and Zr (compared to A and Ir), leads not only to the disordered defect-fluorite structure, but ultimately to a lower-symmetry rhombohedral structure. The $Lu_2Zr_2O_7$ end-member was reported (and simultaneously confirmed by our study below) to crystallise in the rhombohedral structure [43, 45, 177]. Furthermore, other nominally (average, Rietveld) defect-fluorite members of the series reveal the same lower-symmetry structure as $Lu_2Zr_2O_7$ on a local scale [45]. The detailed characterisation of these structures and local correlations in $A_2Zr_2O_7$, as well as $A_2Ti_{2-x}Zr_xO_7$, is discussed below in sections 4.2 and 4.3.

For future applications, a complete picture of structural properties is imperative, particularly for an accurate modelling and a prediction of ionic conductivity pathways, relationships between the structure and physical properties, and material stability under extreme conditions. In addition to the crystal structure investigations, the assessment of the technical applicability of $A_2Zr_2O_7$ zirconates requires a detailed study of their physical properties. Light-A members have been thoroughly studied [178, 179, 180]. However, investigations of heavy rare-earth materials were mostly limited to mechanical and structural properties in high-temperature and high-pressure regions [181, 182, 183, 184]. In the following section 4.1, we focus just on low temperature properties of heavy rare-earth $A_2Zr_2O_7$ zirconates.

4.1 Low-temperature properties ¶

Introduction to publications: **1., 3., 13., 14., 17.**

Light rare-earth zirconates adopting an ordered pyrochlore structure have been extensively studied for their complex electronic properties. An octupolar quantum spin-liquid (QSL) phase was recently reported in $Ce_2Zr_2O_7$ [178]. Importantly, the octupolar nature of magnetic moments makes the QSL phase less prone to chemical disorder at magnetic sites, which is a general problem in other QSL candidates [179]. Antiferro-quadrupolar spin liquid state with spin-ice-like excitations, as well as dynamic interactions between lattice vibrations and magnetic degrees of freedom, were revealed in $Pr_2Zr_2O_7$ [180, 185]. Magnetic moment fragmentation and the coexistence of a fluctuating spin-liquid (Coulomb phase) with ferromagnetic interactions were reported for $Nd_2Zr_2O_7$ [180].

Heavier rare-earth $A_2Zr_2O_7$, especially those crystallising in the defect-fluorite structure, were studied rather scarcely. (Numerous studies on material properties have been published, though.) Only several reports on their low temperature properties have been published, e.g. Refs. [186, 187]. Recently, in addition to our studies of $Er_2Zr_2O_7$ single crystal [71, 188], also A = Gd, Dy and Ho members were investigated. The disordered structure prevents long-range magnetic ordering in $Dy_2Zr_2O_7$; however, the intuitively expected spin glass state is not realised in this material [189]. Instead, a disorder-induced dynamic magnetic ground state on a geometrically frustrated lattice was proposed [190]. The other heavy rare-earth zirconates (A = Gd - Er) show no freezing of spins down to the lowest temperature, unless a magnetic field of about 1 T is applied [191, 192]. Substituting the A-site cation seems to lead to negligible changes in the magnetic properties of these materials, compared to the exhaustively studied $A_2Ti_2O_7$ analogues (e.g. [193, 194, 195, 196] and references therein). We completed an overview on low-temperature properties of heavy rare-earth zirconates by investigating newly synthesised single crystals $Er_2Zr_2O_7$, $Tm_2Zr_2O_7$ and $Yb_2Zr_2O_7$ (see Fig. 2.7) by means of magnetisation and specific heat measurements.

Magnetisation. High-temperature magnetisation revealed a standard dependence on the temperature in the paramagnetic state (Fig. 4.1) and was fitted to the Curie-Weiss formula. The effective magnetic moment, μ_{eff}, and the paramagnetic Curie-Weiss temperature, θ_{p}, values were determined. See Table 4.1 for respective values. A good agreement between experimental μ_{eff} values and the values expected for the A^{3+} free ions was followed: Almost perfect agreement was determined for $Er_2Zr_2O_7$, which is also in concordance with an independent study on the polycrystalline sample [191]. μ_{eff} slightly larger than that for the respective free ion was observed in $Tm_2Zr_2O_7$ and $Yb_2Zr_2O_7$. Explaining higher μ_{eff} value considering a small A-off-stoichiometry caused by the laser furnace working on the limit of its capabilities and transparent white ingots (Erbium-based samples have a pink colour, allowing better absorption of the radiation.)

Table 4.1: Structural parameters and low-temperature properties of investigated $A_2Zr_2O_7$ compounds: constituent-elements ratio A:Zr; ratio of atomic radii r_A/r_{Zr}, space group, lattice parameter a, total angular momentum of A^{3+} free ion J^A; saturated and effective magnetic moment for the A^{3+} free ion μ_s^A and μ_{eff}^A; effective magnetic moment μ_{eff} and paramagnetic Curie temperature θ_p from fit of the magnetisation data to the Curie-Weiss law; value of magnetic moment in 7 T applied magnetic field μ_s^{7T}, temperature where magnetic response to magnetic fields becomes non-linear T_{HT}, temperature of the low-temperature anomaly in specific heat data T_{LT}, and frustration index f. The data is adopted from our publications [177, 198].

	$Er_2Ir_2O_7$	$Tm_2Ir_2O_7$	$Yb_2Ir_2O_7$	$Lu_2Ir_2O_7$
A:Zr (%:%)	50(2):50(2)	50(2):50(3)	50(2):50(2)	50(2):50(2)
r_A/r_{Zr}	1.43	1.42	1.40	1.39
space group	$Fm\bar{3}m$	$Fm\bar{3}m$	$Fm\bar{3}m$	$R\bar{3}$
a (Å)	5.196(1)	5.1788(5)	5.165(1)	9.666(3)*
J^A	7.5	6	3.5	0
μ_s^A (μ_B)	9	7	4	0
μ_{eff}^A (μ_B)	9.58	7.56	4.54	0
μ_{eff} (μ_B)	9.50(3)	7.80(3)	4.80(3)	n/a
θ_p (K)	-12.5(4)	-38.6(5)	-118.0(8)	n/a
μ_s^{7T}	4.79(2)	2.13(2)	1.83(2)	n/a
T_{HT} (K)	30(2)	29(2)	21(2)	n/a
T_{LT} (K)	0.9(1)	–	1.5(1)	n/a
f	15	–	79	n/a

* $c = 8.960(4)$ Å, rhombohedral crystal structure in the hexagonal description
n/a - not applicable, Lu^{3+} is non-magnetic

is plausible. However, no off-stoichiometry was observed in the EDX data. Negative paramagnetic θ_p suggests antiferromagnetic correlations in all investigated $A_2Zr_2O_7$ members. Interestingly, the θ_p increases noticeably from A = Er to A = Yb. The same trend has been observed in another heavy rare-earth $A_2B_2O_7$ series: $A_2Ir_2O_7$ iridates crystallising in pyrochlore structure [57]. However, the trend is not universal for the $A_2B_2O_7$ family of oxides. Different behaviour was reported for $A_2Ti_2O_7$ members. Namely, $Yb_2Ti_2O_7$ shows a small positive θ_p suggesting rather ferromagnetic correlations between nearest-neighbour moments [197]. Moreover, large values could be ascribed to only high-energy CF excitations, giving little information about ground state ordering.

Low-temperature magnetisation is dominated by two effects: (short-range) correlations between rare-earth moments and the crystal electric field. No clear difference between the magnetisation measured under zero-field-cooled and field-

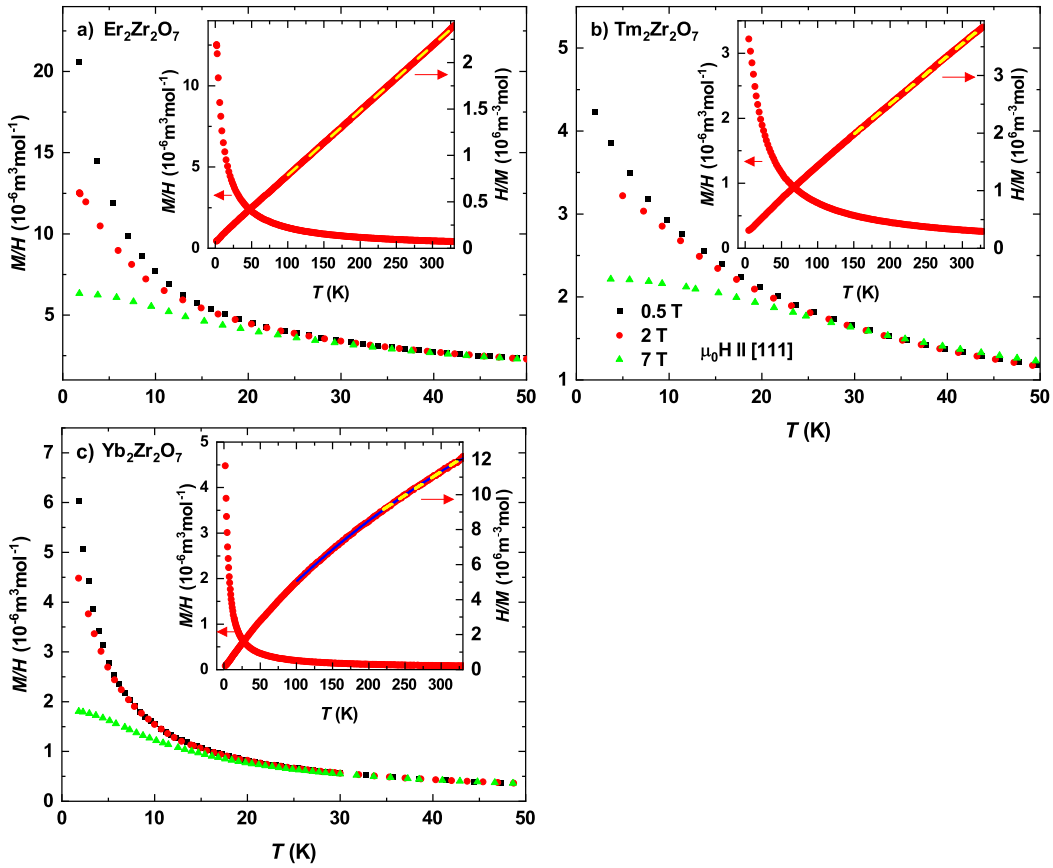

Figure 4.1: Magnetisation measured under ZFC regime with magnetic field applied along the [111] crystallographic direction of $A_2Zr_2O_7$ single crystals with A = Er, Tm, and Yb. The temperature evolutions of the magnetisation in an applied magnetic field at a low temperature are presented. The susceptibility and the inverse susceptibility measured in the whole temperature region are plotted in the insets, together with fits to the Curie-Weiss formula (yellow dashed lines). The blue line in the inset of panel c) stands for fit of the data to the modified Curie-Weiss formula. The figure is adopted from Ref. [177].

cooled regimes was observed down to 2 K. On the other hand, well-observable bifurcation between magnetisation curves measured in different magnetic fields below T_{HT} is revealed in all $A_2Zr_2O_7$ members (see Fig. 4.1 and Table 4.1). Essentially the same behaviour, with similar T_{HT} values, has also been observed in $A_2Ir_2O_7$ pyrochlores and ascribed to the rare-earth magnetism [57]. Simultaneously, only a small anisotropy is observed inspecting the magnetisation data measured with the small magnetic field applied along principal crystallographic directions for all members [177]. In accordance, almost isotropic isothermal magnetisation was measured on respective compounds. The measured data does not indicate any sign of a phase transition induced by the applied magnetic field in any $A_2Zr_2O_7$ compound.

Importantly, the magnetisation value reached in the magnetic field of 7 T at 1.8 K, $\mu_{\mathrm{s}}^{7\mathrm{T}}$ (see Table 4.1), is significantly lower than the expected value for the

A^{3+} free ion. Although the magnetisation curves are not fully saturated in the applied magnetic field of 7 T, they are unlikely to reach the expected value of μ_s in higher field. The saturated value would still be, at least, 50% lower than the theoretical value. The reduced value of saturated magnetisation suggests a strong crystal field anisotropy as speculated analysing the polycrystalline data in Ref. [191]. However, an almost isotropic response was observed by our single crystal measurements [177]. *A*-off-stoichiometry cannot explain such a large difference; the off-stoichiometry must be enormous (more than 50%), which is not supported by EDX analysis, X-ray diffraction data, or determined μ_{eff} values. Fitted μ_{eff} values simultaneously exclude another tempting explanation: Change of valence of rare-earth ions on the atomically disordered lattice and related decrease of the total magnetic moment. Strong spin multipolar fluctuations reducing the total magnetic moment were proposed and partly confirmed in $Nd_2Zr_2O_7$ pyrochlore [199]. Such an explanation could also be used for heavy rare-earth zirconates considering a similarly reduced magnetisation observed for both pyrochlore and defect-fluorite members.

Specific heat. The specific heat data reveal no anomalies in the higher temperature region, in good agreement with the magnetisation data. The low temperature specific heat is then dominated by the crystal electric field effects and a splitting of the ground state multiplet in internal magnetic field generated by short-range correlations between magnetic moments of rare-earth cations (Fig. 4.2). A qualitatively different low-temperature specific heat is observed comparing the $Er_2Zr_2O_7$ and $Yb_2Zr_2O_7$ with the $Tm_2Zr_2O_7$ data. Well-pronounced anomalies at T_{LT} (Table 4.1) are revealed by A = Er and Yb members with a double degenerated ground state protected by symmetry (Kramers' theorem). Considering the highly disordered defect-fluorite structure with A and Zr cations sharing the same Wyckoff site, the anomalies in specific heat are connected rather with spin freezing in these systems, not long-range ordering. In contrast, $Tm_2Zr_2O_7$ data, with Tm^{3+} being non-Kramers' ion, exhibit a broad anomaly at higher temperature. The character and broadness of the anomaly suggest its (pure) crystal-field origin. That is, it reflects the excitations between ground state singlet and excited crystal field levels.

Both, short-range magnetic correlations and crystal field effects are further illustrated by the shift of the specific heat anomaly (and the magnetic entropy) to higher temperatures with an applied magnetic field. The same evolution of the anomaly is followed for A = Er and Yb members, suggesting ferromagnetic correlations in these compounds. Such a conclusion would be, however, in conflict with the negative (for A = Yb member highly negative; Table 4.1) paramagnetic Curie-Weiss temperature. The spin-glass state or a freezing of magnetic moments on disordered geometrically frustrated lattice in the applied magnetic field is thus proposed. $Tm_2Zr_2O_7$, on the other hand, reveals much weaker effect. The anomaly is much broader and there is almost no difference between zero field data and data measured in relatively high magnetic field of 1 T . The

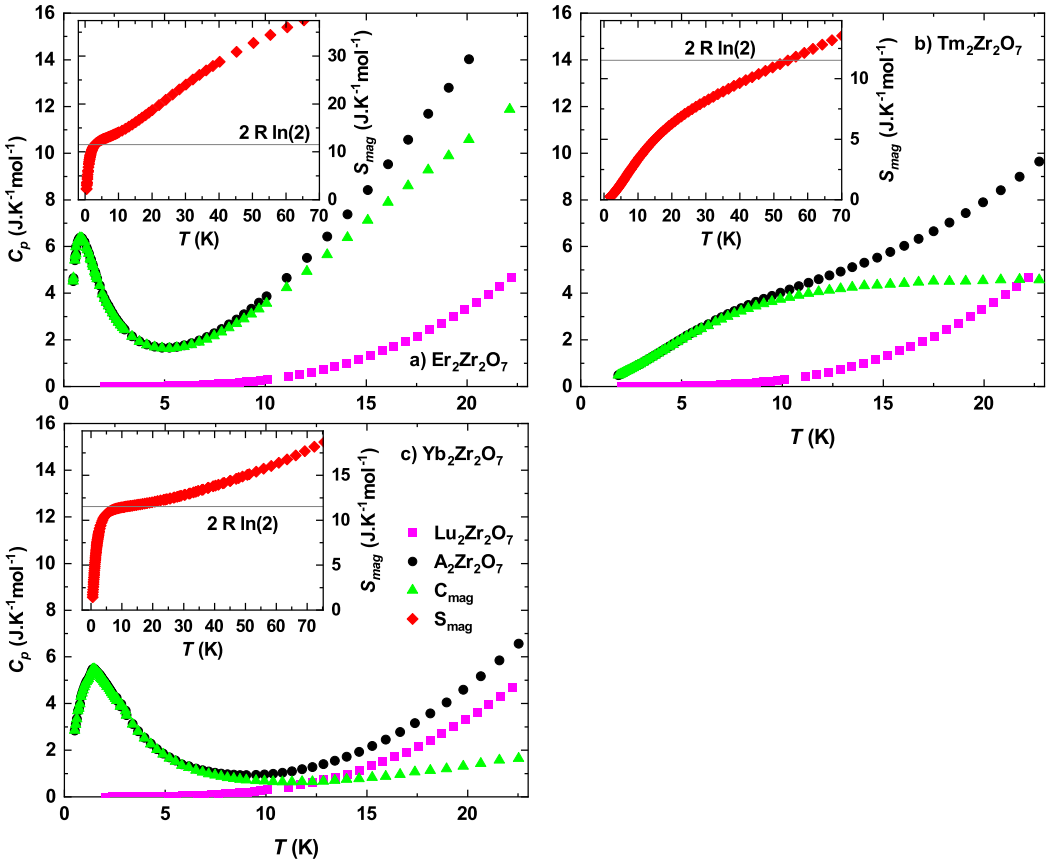

Figure 4.2: Specific heat of $A_2Zr_2O_7$ compounds. Temperature dependence of the specific heat is presented for respective members, together with the non-magnetic $Lu_2Zr_2O_7$ analogue, and their difference standing for magnetic part of specific heat. The insets contain magnetic entropy calculated from the magnetic contribution to the specific heat. The theoretical value of the entropy R.ln(2) for a doublet-ground-state splitting is marked. See the text for details. The figure is adopted from Ref. [177].

difference between investigated members is even better illustrated inspecting the magnetic entropy. The entropy is reaching the value of R.ln(2), corresponding to the doublet-ground-state splitting in the internal magnetic field, just above the high-temperature onset of the specific heat anomaly in $Er_2Zr_2O_7$ and $Yb_2Zr_2O_7$ (see insets in Fig. 4.2). The magnetic entropy of $Tm_2Zr_2O_7$ reaches the same value at the significantly higher temperature, not corresponding to the ground state doublet splitting. Instead, the ground state singlet is proposed, similarly as in pyrochlore analogues $Tm_2Ir_2O_7$ [57, 62] and $Tm_2Ti_2O_7$ [62, 164, 200].

With the knowledge of paramagnetic Curie-Weiss temperature and temperature of the specific heat anomaly, one can calculate the so-called frustration index, f. The frustration index is introduced as a ratio between θ_p and any kind of magnetic transition temperature (in our case T_{LT}) [201]. When $f >> 1$, a strong frustration in the system is present, irrespective whether arising from geometry of the underlying lattice or bond disorder induced by lattice dilution. Defect-fluorite

structure is both: atomically disordered structure with A/Zr cations sharing the same crystallographic position, and geometrically frustrated structure - fcc lattice of cations. Large f values (Table 4.1) were calculated for $Er_2Zr_2O_7$ and especially for $Yb_2Zr_2O_7$, strongly supporting spin glass ground states or freezing of magnetic moments at the low-temperature. As no low-temperature specific heat anomaly was observed in $Tm_2Zr_2O_7$ with singlet ground state, the f index cannot be calculated.

4.2 Average and local crystal structures ¶

Introduction to publications: **1., 3., 13., 15., and 17.**

The majority of the $A_2B_2O_7$ oxides crystallise in a cubic structure of the so-called pyrochlore-type (space group $Fd\bar{3}m$), see Fig. 1.4. The pyrochlore structure, with both A and B sites separately forming lattices of corner-sharing tetrahedra, represents a canonical example of a frustrated lattice. Long-range-ordered magnetic ground-states in compounds with magnetic A or B cations are suppressed due to competing exchange interactions. Instead, frustrated and strongly correlated unconventional ground-states are formed [44, 202, 203]. Another group of $A_2B_2O_7$ oxides crystallise in the so-called defect-fluorite-type of cubic structure (space group $Fm\bar{3}m$). The defect-fluorite structure is also a geometrically frustrated lattice, as the cations form the fcc lattice. In contrast to the fully ordered pyrochlore lattice, the defect-fluorite lattice is characterised by a complete disorder of A and B cations in the single Wyckoff position, and disorder of seven oxygen anions and one vacancy in the second crystallographic site with the multiplicity eight [71, 204]. For these structural properties, the respective compounds have significant application potential [171, 172, 174]. In addition, an orthorhombic structure with the space group $Pnma$ and monoclinic structure with the space group $P21$ have also been observed/proposed for several members of the family [205, 206]. Very recently, another type of a crystal structure, rhombohedral structure with space group $R\bar{3}$, was reported for $Lu_2Zr_2O_7$ zirconate [204].

The crystal structures of $A_2B_2O_7$ have been frequently discussed from the viewpoint of the size ratio between the A and B cations (r_A/r_B). Empirically, the compounds with high values of r_A/r_B crystallise in lower-symmetry structures. The region of the stability for the pyrochlore structure is between approximately $1.48 < r_A/r_B < 1.63$. Lower values of r_A/r_B ratio are typical for compounds crystallising in the defect-fluorite structure. The transition between structures, especially cubic variants, could be understood in the following way: For heavy rare-earth elements and light B elements, the size difference between ions is reduced, leading to a considerable thermodynamic drive for the A/B mixing [175, 176]. Ultimately, a fully disordered defect-fluorite structure is realised. However, recent studies have shown that this explanation, although consistent,

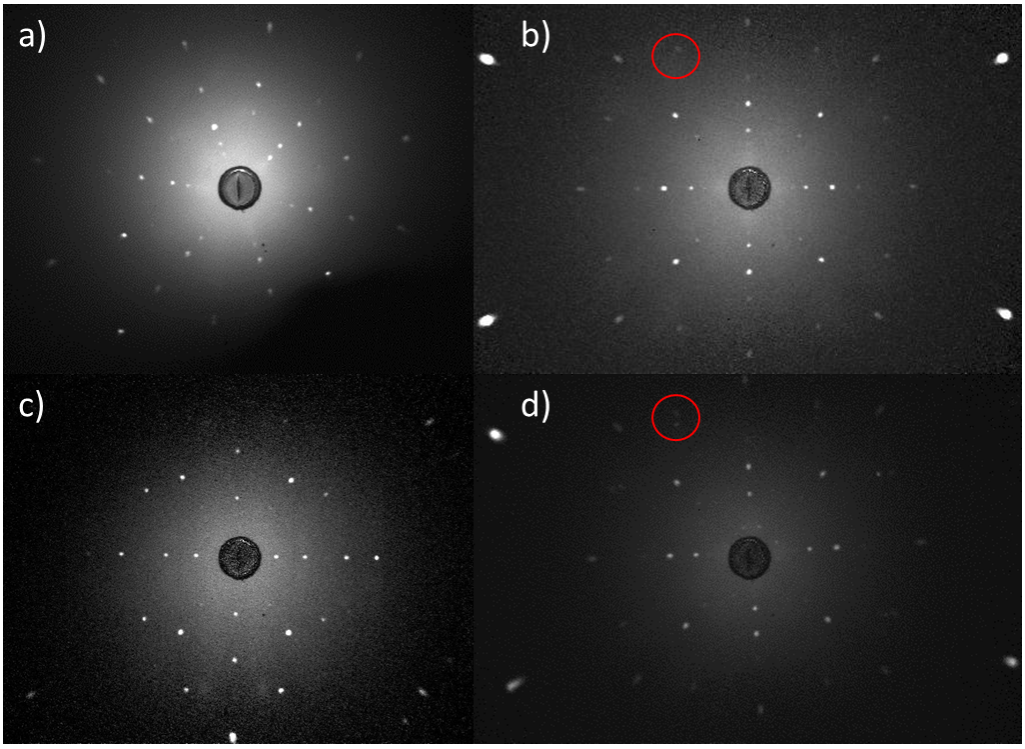

Figure 4.3: Laue X-ray diffraction patterns of investigated $A_2Zr_2O_7$ single crystals: $Er_2Zr_2O_7$ along [111] direction (three-fold symmetry) (a), $Tm_2Zr_2O_7$ along [100] direction (four-fold symmetry) (b), $Yb_2Zr_2O_7$ along [110] direction (two-fold symmetry) (c). $Lu_2Zr_2O_7$ crystallises in a different, lower-symmetry structure (space group $R\bar{3}$). Its Lauegram on panel (d) is to be compared with panel (b). Additional reflections in $Lu_2Zr_2O_7$ patterns are observed around the center of the Lauegram, as well as elsewhere (one of the regions of difference is highlighted by the red circle). The figure is adopted from Ref. [177].

is not fully satisfactory, as demonstrated in the $A_2Zr_2O_7$ series: Light rare-earth members (A = La - Eu) crystallise in an ordered pyrochlore structure. Heavy A = Gd - Yb members adopt an average defect-fluorite structure, instead. However, on a local scale they reveal different lower-symmetry structure [43, 45]! The investigation and identification of the cubic average and low-symmetry local structures in $A_2Zr_2O_7$ series have been the aim of our research introduced below.

4.2.1 Average structures, Rietveld refinement

Single crystals synthesised using the optimised methods described in section 2.3 were investigated by means of X-ray and neutron diffraction techniques. Unlike X-rays, which interact strongly with the material and typically only probe the surface of a crystal, neutrons interact more weakly and penetrate the entire crystal allowing a confirmation of the quality of the entire volume. The Laue X-ray and neutron diffraction patterns indicate that all the investigated $A_2Zr_2O_7$ single crystals are single-phase and high-quality in the volume, see Figs. 2.8, 4.3, and 4.4. The light rare-earth members (A = La, Nd, and Eu) crystallise

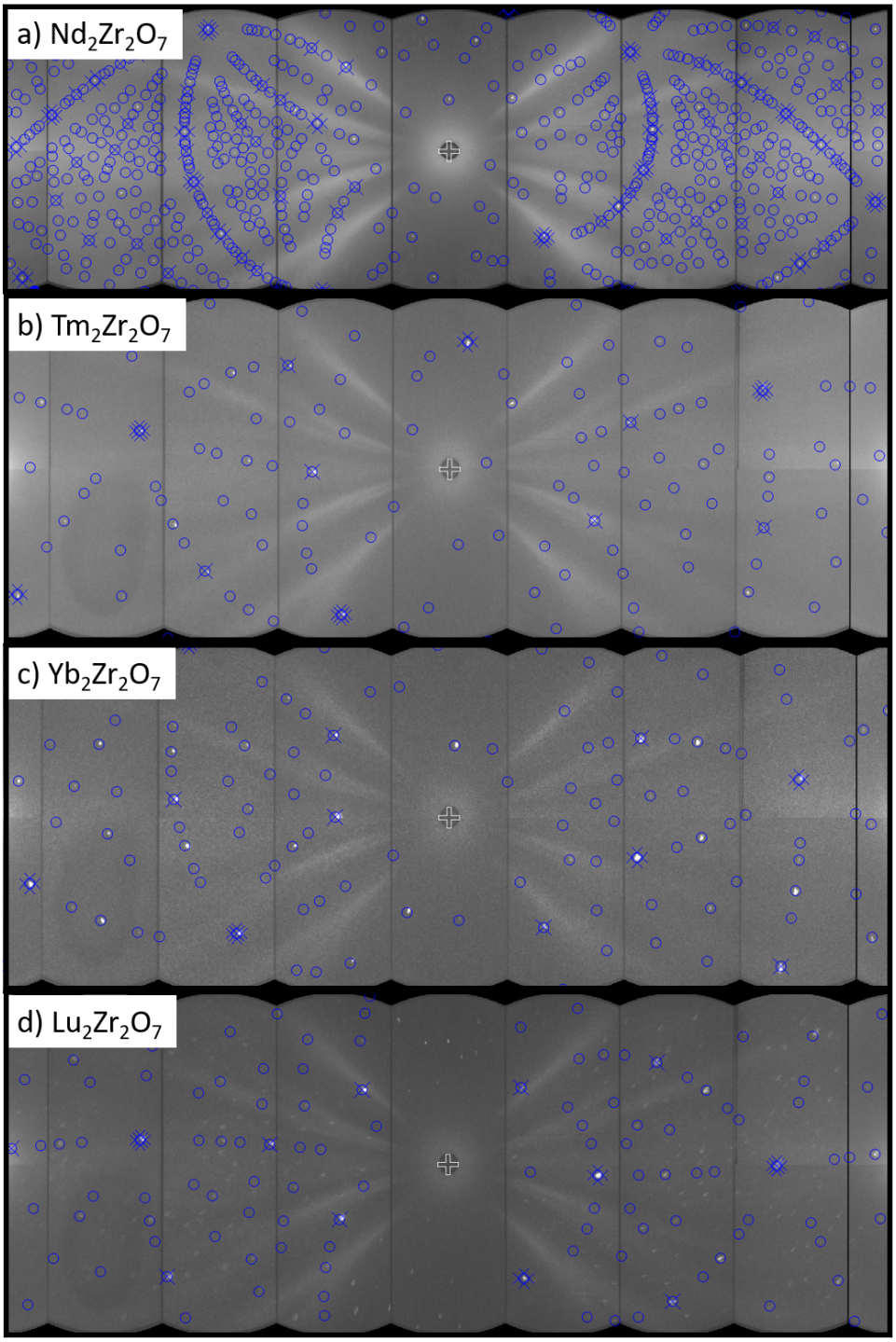

Figure 4.4: Neutron Laue diffraction patterns of selected $A_2Zr_2O_7$ single crystals measured using the CYCLOPS diffractometer at the Institute Laue-Langevin, Grenoble, France, representing three crystal structures: the pyrochlore structure of $Nd_2Zr_2O_7$ (a), the defect-fluorite structure of newly synthesised $Tm_2Zr_2O_7$ (b) and $Yb_2Zr_2O_7$ (c), and the slightly distorted rhombohedral structure of $Lu_2Zr_2O_7$ (d). The calculated patterns for the respective structures are presented as well; regarding $Lu_2Zr_2O_7$, the calculated patterns of defect-fluorite structure are shown for the clarity of presented data and to highlight the difference between the two structures. The figure is adopted from Ref. [99].

in the pyrochlore-type of structure; see Fig. 4.6 for illustration. No superstructure peaks or signs of additional phases are observed in the diffraction patterns. The defect-fluorite structure model fits well for heavier-rare-earth members (A = Gd, Tb, Dy, Ho, Er, Tm, and Yb), as well as A = Y member. The diffraction patterns of $Lu_2Zr_2O_7$ resemble the defect-fluorite structure; we intentionally fitted the Laue neutron diffraction patterns in Fig. 4.4d using the defect-fluorite model (with the lattice parameter a = 5.19(5) Å). However, a large number of weaker reflections cannot be described by this model. The model based on the rhombohedral structure must be used (Table 4.1), see subsection 4.2.2.

Importantly, no further reflections, in addition to the defect-fluorite ones, were observed in the Laue patterns, X-ray and neutron, of other heavy rare-earth zirconates. Such an observation is somewhat surprising, especially in regard to $Yb_2Zr_2O_7$ (Fig. 4.4c) which could be assumed to be a border compound between the defect-fluorite part of the series and the rhombohedral $Lu_2Zr_2O_7$. Therefore, we further investigated $Yb_2Zr_2O_7$ using the powder neutron diffraction technique [99]. The diffraction patterns were well described using the defect-fluorite structure model. No additional peaks were observed. However, a broad signal was followed on top of the background, strongly supporting the presence of short-range structural correlations in this zirconate. Signs of short-range structural correlations in powder X-ray and especially synchrotron X-ray diffraction patterns were observed in all heavy rare-earth zirconates (A = Gd - Yb) [45, 99, 198]. Although no clear extra peaks were seen in the patterns, a broad additional signal on top of the background and signs of tiny superstructure peaks were followed.

The X-ray and synchrotron X-ray diffraction patterns of $A_2Zr_2O_7$ were refined using respective pyrochlore, defect-fluorite, and rhombohedral models, leading to lattice and structural parameters listed in Table 4.1 and Refs. [99, 198]. The refined lattice parameter a of the cubic lattices develops monotonically with A, as illustrated in Fig. 4.5. The development of a follows the lanthanide contraction. That is, the lattice parameter in $A_2B_2O_7$ decreases with increasing atomic number of the rare-earth element. Similar development is manifested for compounds crystallising in both pyrochlore and defect-fluorite structure. A smooth evolution of the lattice parameter within the whole series is illustrated by re-scaling the defect-fluorite unit cell to the pyrochlore unit cell (multiplied the lattice parameter by a factor of two). Generally, the same evolution of a with the ionic radius of rare-earth atom is followed in $A_2Ti_2O_7$ titanates [207], $A_2Hf_2O_7$ hafnates [208, 209, 210, 211], and $A_2Ir_2O_7$ iridates [57, 61, 65, 135, 212].

The lattice parameters of the $Y_2B_2O_7$ analogues were expected to fit in-between those of A = Dy and Ho members, being closer to the $Ho_2B_2O_7$ parameters, due to the respective sizes of their ionic radii. Indeed, $Y_2B_2O_7$ crystallise in respective crystal structures of heavy rare-earth analogues. However, their lattice parameter systematically fits in-between parameters of A = Ho and Er members, instead. $Gd_2Zr_2O_7$ and $Dy_2Hf_2O_7$ stand on the border between the defect-fluorite and pyrochlore stability regions. The approximate border between

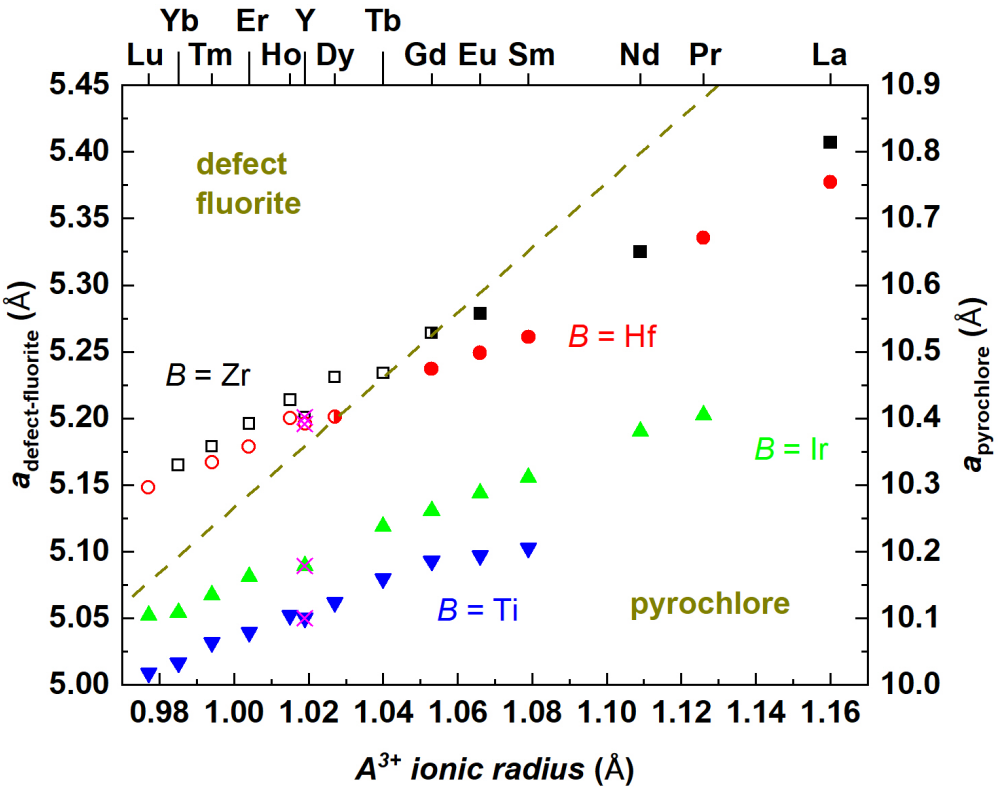

Figure 4.5: Development of lattice parameters with ionic radius of the rare-earth A^{3+} ion. The lattice parameters of $A_2Zr_2O_7$ and $A_2Hf_2O_7$ members crystallising in the defect-fluorite structure (open symbols) were re-scaled (multiplied by a factor of two) to better follow the evolution within the series and compare it to pyrochlore $A_2B_2O_7$ analogues (closed symbols). The lattice parameters of titanes [207], iridates [57, 61, 65, 135, 212], and hafnates [208, 209, 210, 211] were adopted from the respective (our) publications. The lattice parameters of the $Y_2B_2O_7$ compounds are indicated by crossed symbols. $Gd_2Zr_2O_7$ and $Dy_2Zr_2O_7$ form the approximate border between the pyrochlore and defect-fluorite structures (dashed line). $A_2Ti_2O_7$ (A = Nd, Pr, La) crystallise in a different, monoclinic structure [213]. Therefore they are not depicted. The figure is adopted from Ref. [99].

the two regions is indicated by dashed line in Fig. 4.5. The lattice parameter of the $Tb_2Zr_2O_7$ member also lies on this border. Nevertheless, its diffraction patterns clearly indicate the average defect-fluorite structure. Fine structural details of $A_2Zr_2O_7$ are discussed in the following subsection 4.2.2.

4.2.2 Local environment, pair-distribution-function

To address all uncertainties related to the crystal structure (Fig. 4.6) and expected local structural correlations, we performed total scattering experiments on most of heavy rare-earth $A_2Zr_2O_7$ zirconates and analysed the measured pair-distribution-function. The samples were investigated using both synchrotron X-ray and neutron scattering to obtain complementary information. A better resolu-

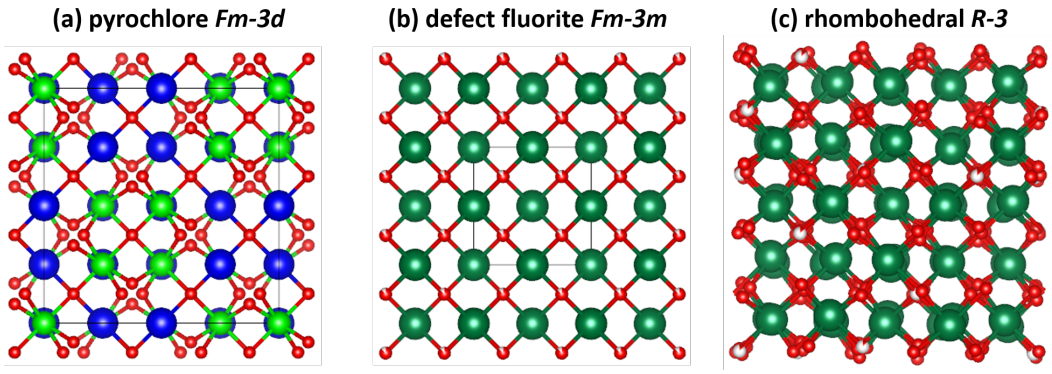

Figure 4.6: Crystallographic structures of $A_2Zr_2O_7$ zirconates: (a) cubic pyrochlore-type (space group $Fd\bar{3}m$), (b) cubic defect-fluorite-type (space group $Fm\bar{3}m$), and (c) rhombohedral structure (space group $R\bar{3}$). In the latter two cases, the A and Zr atoms share the same crystallographic positions, and oxygen sites are only partly occupied. The black lines in (a) and (b) represent respective unit cells. The unit cell in (c) is not shown because the structure is oriented along the former two unit cells and, therefore, the unit cell is not reasonably portrayable. The figure is adopted from Ref. [99]. Compare the structures with respective structures in Fig. 1.4.

tion of X-ray diffraction and higher sensitivity of neutrons to oxygen were utilised. Importantly, the structures discussed in further text were probed by simultaneously refining four sets of data (if available for specific $A_2Zr_2O_7$ compound); that is, X-ray and neutron diffraction patterns and pair-distribution-functions. The respective data and their comparison is presented in Fig. 4.7 and Fig. 4.8.

$La_2Zr_2O_7$ compound was measured as the representative of the pyrochlore part of the series. All data, neutron and synchrotron radiation diffraction and PDF, were, indeed, described by the $Fd\bar{3}m$ structure. Heavier rare-earth $A_2Zr_2O_7$ zirconates revealed considerably different diffraction patterns compared to end-members of the series (Fig. 4.7); perfectly in agreement with the data discussed in precious sections. A = Dy - Tm patterns are almost identical and were well described with the defect-fluorite structure (see our publication in preparation [45]). Also crystal structure of the $Yb_2Zr_2O_7$ member with slightly different diffraction patterns was identified with the $Fm\bar{3}m$ structure. However, the $Lu_2Zr_2O_7$ end-member reveals completely different diffraction patterns, which we confirmed (previously reported in [204]) to be consistent with the rhombohedral $R\bar{3}$ structure. Comparing the diffraction patterns of the end-members with other heavy rare-earth zirconates, no clear similarities were traced.

In contrast, inspecting the PDF data in Fig. 4.8 lead us to the conclusion that PDF pattens of heavy $A_2Zr_2O_7$ including the A = Lu end-member are very similar. Prominently similar PDF data strongly suggest, at least, similar local arrangement of ions in the unit cells of $Lu_2Zr_2O_7$ crystallising in the rhombohedral structure and the rest of heavy rare-earth zirconates adopting the defect-fluorite structure on average (Fig. 4.7). Indeed, fitting these PDF data using the rhom-

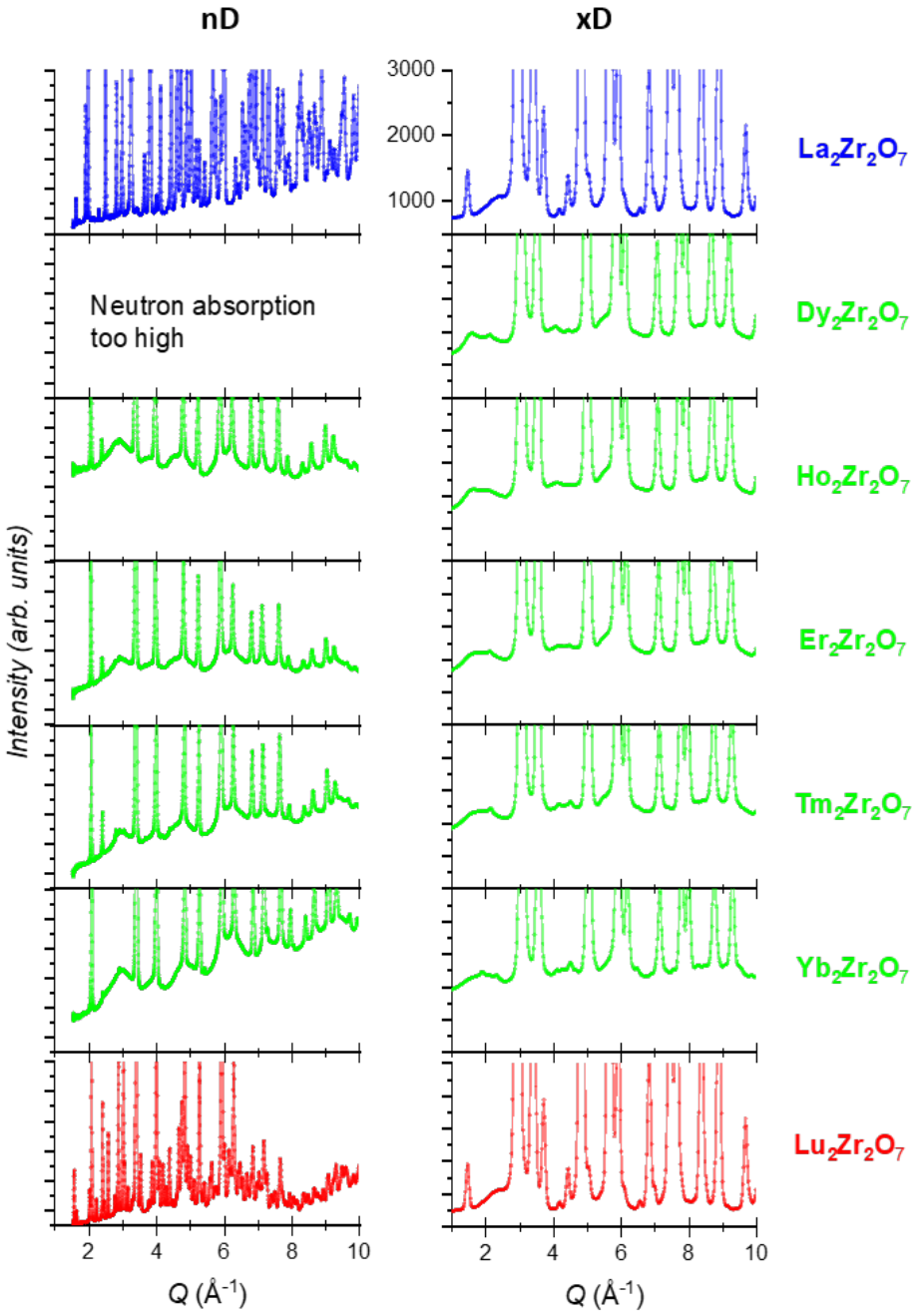

Figure 4.7: Diffraction patterns of the rare-earth $A_2Zr_2O_7$ zirconates. Left column shows neutron diffraction data and right column presents synchrotron X-ray diffraction data for individual members. Clear differences between pyrochlore $La_2Zr_2O_7$, defect-fluorite $A_2Zr_2O_7$ with A = Dy - Yb, and rhombohedral $Lu_2Zr_2O_7$ members is followed (also by colour code).

bohedral model of $Lu_2Zr_2O_7$ leads to a good agreement [45]. We once again highlight that the average (global, Rietveld refined) structures of $Lu_2Zr_2O_7$ and other heavy rare-earth zirconates are not identical (Fig. 4.7), whereas they reveal (almost) identical pair-distribution-function patterns and therefore likely the same local structures.

In fact, refining the PDF patterns of heavy rare-earth $A_2Zr_2O_7$ resulted in the rhombohedral structure model identical to that of $Lu_2Zr_2O_7$. Several trials

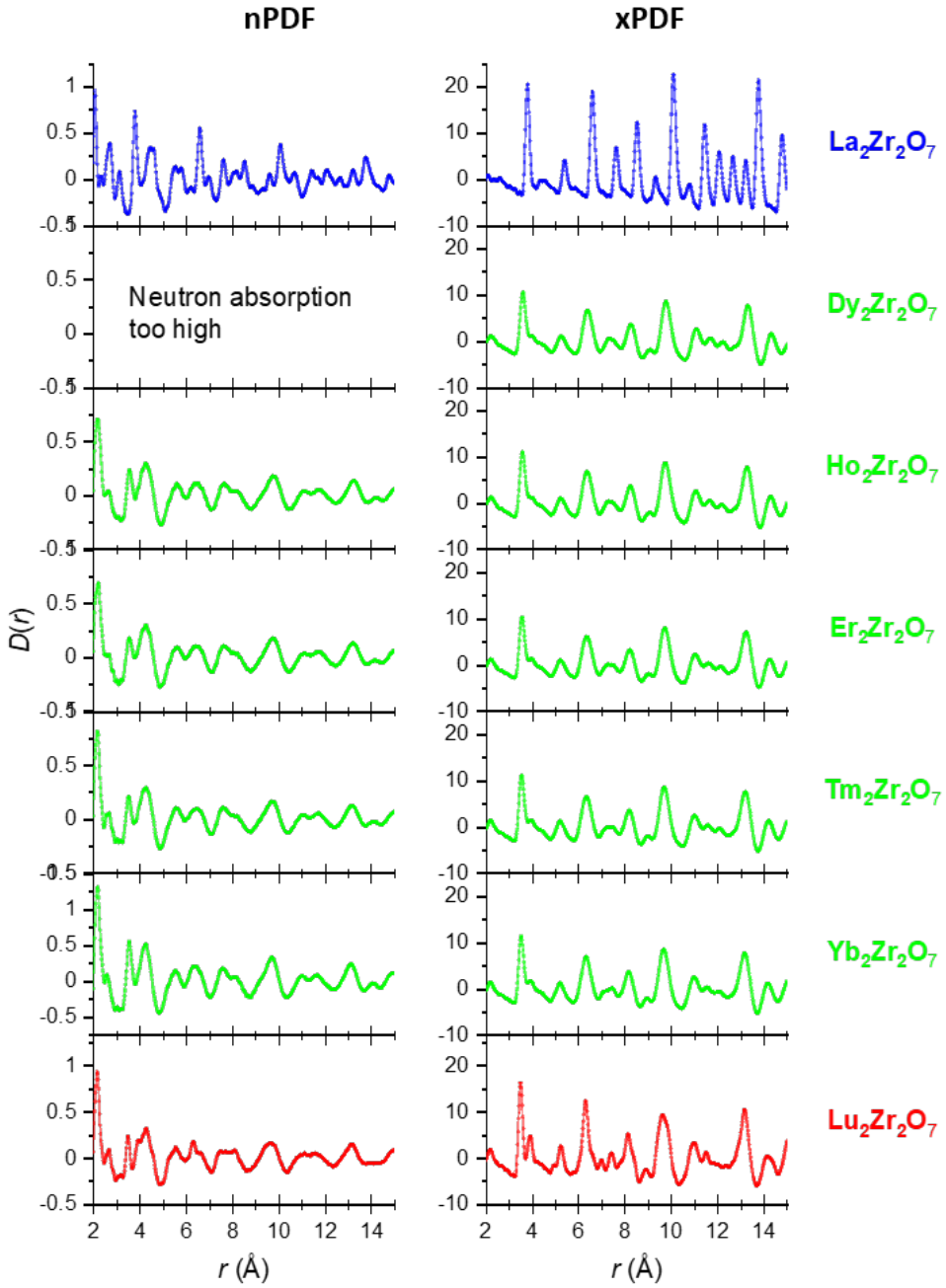

Figure 4.8: Pair-distribution-function patterns of the rare-earth $A_2Zr_2O_7$ zirconates. Left column shows neutron PDF data and right column presents synchrotron X-ray PDF data for individual members. The difference between PDF data of pyrochlore $La_2Zr_2O_7$ and of the rest of the investigated members is observed. Surprisingly, all heavy rare-earth members reveal almost identical PDF patterns, including the $Lu_2Zr_2O_7$ end-member. Colour code is the same as used for diffraction data in Fig. 4.7.

were conducted; see example in Fig. 4.9. First, the defect-fluorite structure model, the model optimised fitting the diffraction patterns of heavy rare-earth zirconates, was used. A strong disagreement was observed comparing the PDF data and model. A slightly better agreement was followed using the pyrochlore model, but some features in the data were still not sufficiently reproduced. Next,

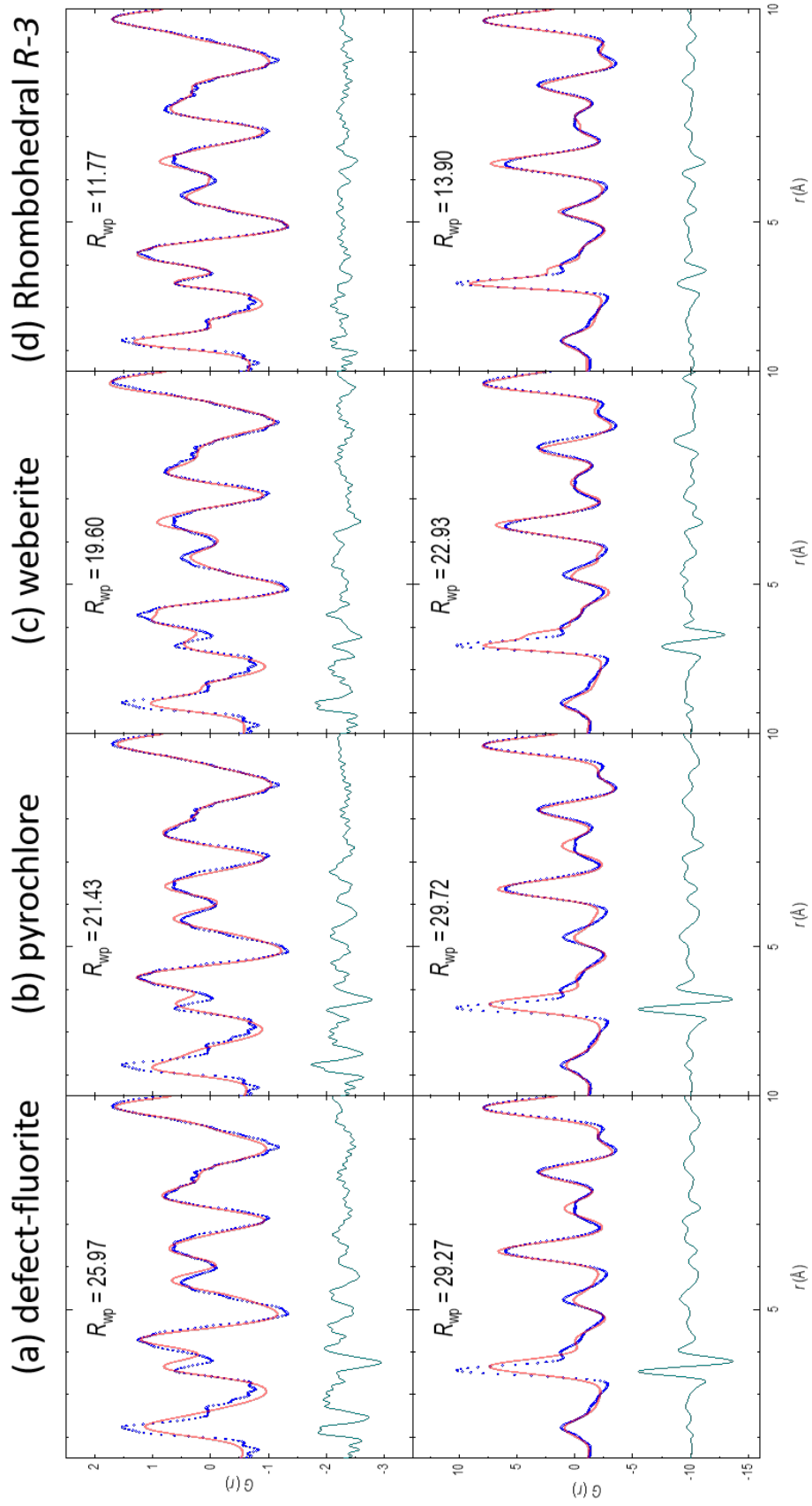

Figure 4.9: Neutron (top row) and synchrotron X-ray (bottom row) pair-distribution-function (PDF) of $Er_2Zr_2O_7$ fitted by four structural models. The data (blue dots), model (red line) and difference curve (green line) are presented together with the agreement factor for each model.

the so-called weberite structure model was employed. This model was introduced for the $Ho_2Zr_2O_7$ member in [43] and confirmed by the DFT calculations to be energetically more stable than other two models. Nevertheless, comparing our PDF data with the weberite model shows only a slightly improved agreement, with respect to, e.g., pyrochlore model. Therefore, we commenced the search for the correct local structural model. The symmetry modes of the system were analysed using the Isodistort program [214, 215]. Checking individual modes and their effect on the diffraction and PDF patterns (program Topas) resulted in a model identical to the rhombohedral structure of $Lu_2Zr_2O_7$. Refining the $A_2Zr_2O_7$ data with this model led to reasonably good fit as illustrated in Fig. 4.9d, and we consider it as a well-justified solution.

Our experimental results were also supported by the theory. The density functional theory (DFT) plane-wave calculations were performed following previous studies of pyrochlore-type compounds [216, 217, 218, 219]. The model structures of pyrochlore, defect-fluorite and weberite used for calculations were exactly the ones used in [219]; that is, produced with the special quasirandom structure approach [220]. The $R\bar{3}$ structure was modelled with a supercell containing 231 atoms with ions distributions reflecting the experimentally refined values. The configurational entropies of the disordered structures were computed from fractional compositions using standard formula as applied in previous studies [218, 216, 219]. See our publication in preparation at the end of the present thesis [45] for details. For the heavy rare-earth $A_2Zr_2O_7$ zirconates, the $R\bar{3}$ structure is clearly energy preferred structure, compared to the weberite structure reported previously for the $Ho_2Zr_2O_7$ member [43], as well as defect-fluorite structure. That is, our experimental and DFT results are perfectly in agreement, allowing us to unambiguously designate the rhombohedral $R\bar{3}$ model as a local crystal structure of the heavy rare-earth $A_2Zr_2O_7$ zirconates.

4.3 Ti-Zr substitution in $A_2Zr_2O_7$ ¶

Introduction to publications: **1., 3., 5., 6., and unpublished.**

Following the studies of average and local structures and correlations in $A_2Zr_2O_7$ compounds, we have aimed our attention at B-substituted $Er_2(Ti,Zr)_2O_7$ and $Lu_2(Ti,Zr)_2O_7$ series'.

In the course of our recent X-ray and neutron diffraction and pair-distribution-function (total scattering) studies of $A_2Zr_2O_7$ series, we found out that the local structure of heavy rare-earth members (including $Er_2Zr_2O_7$) differs from the average (global) defect-fluorite structure (subsection 4.2.2). The rhombohedral structure, which was previously reported as an average structure of $Lu_2Zr_2O_7$ [204] (confirmed by our recent study [45]), has been identified as the local structure of this part of the series. We note a previous publication on $Ho_2Zr_2O_7$ member

reporting different local structure [43]. Our recent joint experimental and theoretical study [45] showed that the rhombohedral structure allows a better data description than the previously reported structure.

Although our local-structure study brought a lot of information about heavy rare-earth zirconates, it missed one crucial point. That is, our study on $A_2Zr_2O_7$ did not allow us to reveal the details of the boundary between the pyrochlore and defect-fluorite parts of the series. $Gd_2Zr_2O_7$ zirconate, representing the very border between the two cubic structures [75, 183, 222], contains a natural mixture of Gd isotopes with enormous absorption cross-section for neutrons. Its effective investigation by neutron scattering is therefore significantly hampered/impossible. Simultaneously, it has been shown in subsection 4.2.2 that only joint analysis of X-ray and neutron data leads to unambiguous results. Therefore, we decided to opt to study the $Er_2(Ti,Zr)_2O_7$ and $Lu_2(Ti,Zr)_2O_7$ series', where the isoelectronic Ti-Zr substitution leads to the change of crystal structure in a similar way as in the $A_2Zr_2O_7$ series substituting rare-earth element; see Fig. 4.10. Of course, such an approach is connected with an additional disorder in the lattice. Regarding the defect-fluorite lattice, a single Wyckoff position is shared by A, Ti, and Zr cations. Such disorder naturally complicates the interpretation of structural, magnetic, and material properties‘ even more than in the $A_2Zr_2O_7$ series.

$Er_2Ti_2O_7$ and $Lu_2Ti_2O_7$ end-members crystallise in the pyrochlore crystal structure [207], while $Er_2Zr_2O_7$ adopts the defect-fluorite structure and $Lu_2Zr_2O_7$ exhibit a lower-symmetry rhombohedral structure [45, 204]. Starting with the pyrochlore $Er_2Ti_2O_7$, the substitution of Ti by Zr is to affect the average and local structures by increasing the disorder on the B site, while maintaining the point symmetry of the Er site. Large Ti-Zr substitutions will lead to further mixing of cations at both A and B sites, ultimately leading to the average defect-fluorite structure. Although locally, only partial disorder and rhombohedral structure will be realised, as demonstrated in the parent $Er_2Zr_2O_7$ [45]. $Lu_2(Ti,Zr)_2O_7$ series is expected to exhibit even more complicated phase diagram. The Ti-Zr substitution is likely to induce the transition from the ordered pyrochlore, through the disordered defect-fluorite, to a partially ordered rhombohedral structure, as schematically indicated in Fig. 4.10.

We synthesised a number of polycrystals and mainly single crystals sufficiently covering the $Er_2(Ti,Zr)_2O_7$ and $Lu_2(Ti,Zr)_2O_7$ series' and investigated them by techniques introduced above for the $A_2Zr_2O_7$ series. In addition to sample characterisation using electron microscopy, laboratory X-ray diffraction, specific heat, and for A = Er series magnetisation measurements, advanced experimental techniques were employed. Namely, synchrotron X-ray and neutron diffraction and pair-distribution-function experiments [223] revealed the fine details of average and local structures in the two series, mostly confirming our assumptions on structure evolution with Ti-Zr substitution. Moreover, for Ti-Zr concentrations close to the border between the pyrochlore and defect-fluorite domains, additional reflections - inconsistent with any of the above introduced structures - have

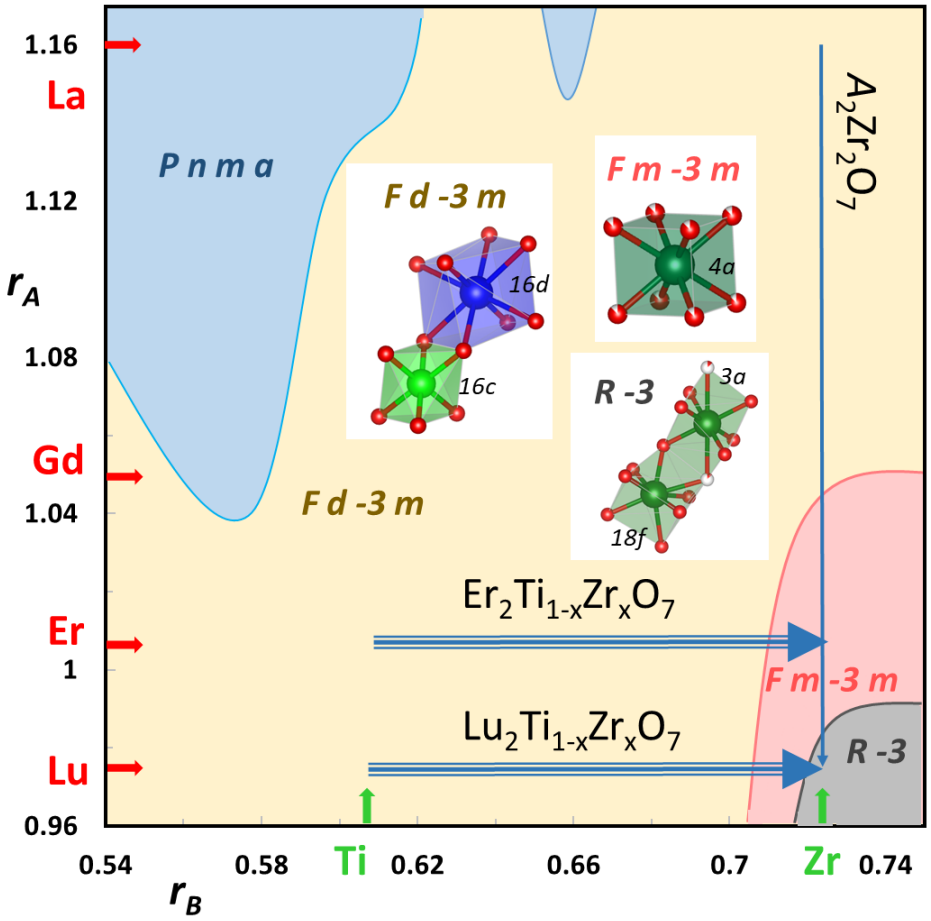

Figure 4.10: Schematic phase diagram of crystal-structure-types of $A_2B_2O_7$ oxides, including our recent results. Atomic radii of A and B cations are plotted on respective axes. Individual cations and oxygen anions orderings in structures relevant for our research are presented. The vertical arrow indicates the $A_2Zr_2O_7$ series, and the horizontal arrows demonstrate $Er_2(Ti,Zr)_2O_7$ and $Lu_2(Ti,Zr)_2O_7$ series'. The figure was adopted from the bachelor thesis of J. Zelenka [221] and slightly modified.

been observed. Furthermore, $Er_2Ti_{1.6}Zr_{0.4}O_7$ and $Lu_2Ti_{1.6}Zr_{0.4}O_7$ compositions, being deeply in the pyrochlore domain, revealed completely different diffraction patterns. Importantly, the same patterns were observed in both A = Er and Lu members! The superstructure is being evaluated at the moment.

Simultaneously, the thermal stability of selected members and evolution of their structural parameters were followed up to extremely high temperatures using powder neutron diffraction. All investigated members showed stable pyrochlore and defect-fluorite structure, respectively, up to 1600 °C. No additional peaks or change of intensity on respective peaks were observed. Standard lattice expansion with increasing temperature was followed. The data is currently being processed.

In addition, phonon modes, their dispersion, and crystal field schemes of selected $Er_2(Ti,Zr)_2O_7$ members were recently investigated using inelastic neutron scattering technique [224]. The experiment allowed us to follow the systematics in the series' depending on the details of (local) structure of respective members.

The measured spectra changed significantly with substituting Ti by Zr, reflecting the change of the local crystallographic environment, point group symmetry, of Er cations in the respective lattices.

All these briefly introduced results are very recent; most of the data was measured in the second half of the year 2023 and at the beginning of the year 2024. We plan to publish these results (at least four publications) in the following year/s.

5. Conclusions and prospects ¶

The present habilitation thesis summarises the outcomes of my six-year scientific work that has been focused on a family of geometrically frustrated $A_2B_2O_7$ oxides, especially rare-earth iridates and zirconates. The results I have collected in collaboration with my colleagues and mainly students have been presented in 17 publications, so far. Further results, just briefly introduced in the present thesis, will be published in the near future.

The thesis overviews our exciting journey establishing the topic of frustrated magnetism on the ground of the Department of Condensed Matter Physics, Faculty of Mathematics and Physics, Charles University. During the six-year period, we have searched for and eventually mastered the optimal synthesis routes for preparation of high-quality polycrystalline samples and mainly single crystals from the $A_2B_2O_7$ family; and investigated them by a spectrum of experimental techniques ranging from standard laboratory methods to advanced microscopic techniques at large-scale facilities abroad. Most notably, we have synthesised world-quality single crystals of selected $A_2Ir_2O_7$ iridates and studied them using neutron scattering and synchrotron X-ray radiation techniques.

The main results of our work are briefly recapitulated in the following points:
(i) Heavy rare-earth $A_2Ir_2O_7$ iridates (A = Dy - Lu) were synthesised using a flux preparation method; including for the first time reported $Tm_2Ir_2O_7$ member. The preparation route was optimised, and high-quality stoichiometric polycrystals have been routinely synthesised at our workplace.
(ii) Synthesis of $A_2Ir_2O_7$ single crystals is intricate, requiring a considerable experience and devotion. Eventually, we succeeded in preparing A = Nd, Ho, Er, Tm, and Lu single crystals of high-quality and importantly correct stoichiometry. In the case of heavy A members, our single crystals are the best crystals available worldwide at present.
(iii) The majority of $A_2Zr_2O_7$ zirconates has been synthesised in polycrystalline and single-crystalline form employing our simplified laser-heated floating-hot-zone and pedestal (Czochralski) methods. The developed preparation recipe allows us to effectively, efficiently, and reliably synthesise the crystals, omitting several intermediate steps commonly performed preparing this type of materials. Furthermore, the method is applicable not only to zirconates, but also to other $A_2B_2O_7$ and even unrelated compounds.
(iv) Synthesised samples were investigated by a variety of experimental techniques, generally confirming their high quality and allowing full characterisation of their macroscopic and microscopic properties. Our studies resulted in a detailed overview on systhematics within respective series'.
(v) Average crystal structures of investigated compounds were revealed/confirmed by laboratory and mainly synchrotron X-ray radiation and neutron diffraction techniques. The respective structures were shown to be stable in a broad temperature range and robust against an applied external pressure of up to 20 GPa.

(vi) Magnetic phase diagram of the Ir-sublattice ordering in $A_2Ir_2O_7$ series was completed, based on our bulk properties measurements and muon spin resonance experiments. The magnetic ordering of the Ir-sublattice was shown to be independent of the rare-earth magnetism or electronic properties. Instead, the interatomic distances and bond-angles in the pyrochlore lattice determine the magnetic ordering of the Ir sublattice and phase transition temperature in respective rare-earth members.
(vii) Conductive properties in $A_2Ir_2O_7$ were studied and explained in the framework of the Slater mechanism. That is, the phase transition from the metal/semimetal/semiconductor high-temperature state to the insulating low-temperature state was proposed to be directly connected with (that is, induced by) the antiferromagnetic ordering of the Ir sublattice.
(viii) The hypothesis on the insulating AIAO and AOAI antiferromagnetic domains and conductive domains-interfaces in $A_2Ir_2O_7$ pyrochlores was partly verified by investigating newly synthesised single crystals. Microscopic experiments fully confirming the hypothesis are proposed for at large-scale facilities.
(ix) Inelastic neutron scattering experiments allowed us to determine the crystal field schemes of $Er_2Ir_2O_7$ and $Tm_2Ir_2O_7$ iridates. The schemes were shown to explain the magnetic properties of respective members connected with a specific rare-earth element, at least at higher temperature. The development of the crystal field parameters within the series was discussed and noticeable systematics highlighted. Crystal field excitations were also measured in the $A_2Zr_2O_7$ series and some Ti-Zr substituted members, crystallising in the disordered structures. The evaluation of crystal field schemes of individual members is inseparably connected with the details of respective crystal structures, and is in progress.
(x) Resonant inelastic X-ray scatterings (RIXS) experiment on $Er_2Ir_2O_7$ and $Lu_2Ir_2O_7$ members probed collective magnetic excitations/low-spin dynamics, spin-orbit, and crystal-field excitations of the Ir sublattice. Quantitative information about the exchanges within the Ir sublattice, but also the f-d exchange between Ir and respective rare-earth (Er) were revealed. Not published yet or included in the present thesis as continuing experiments is scheduled.
(xi) Average and especially local structures were determined in $A_2Zr_2O_7$ zirconates. Light rare-earth zirconates were observed to crystallise in pyrochlore structure on global and local scale, while different average and local structures of heavy A members were found. In addition to the average defect-fluorite structure, a local lower-symmetry rhombohedral structure was identified by analysing our synchrotron X-ray radiation and neutron diffraction and pair-distribution-function data. The same microscopic studies with similar results have been performed on $Er_2(Ti,Zr)_2O_7$ and $Lu_2(Ti,Zr)_2O_7$ series'. Based on the structural details, ionic conductivity pathways were calculated and discussed in these application relevant materials.

In the course of our research, we have commenced numerous collaborations with colleagues interested in the same topic, most importantly with the group of

Dr. Elsa Lhotel, Institut Néel, CNRS, Université Grenoble Alpes, France; and the group of Sylvain Petit, Université Paris-Sacley, France. In the last two years, we performed several joint experiments and are currently working on publishing the obtained results. In addition to sub-kelvin magnetisation measurements on $Er_2Ir_2O_7$ single crystal, we investigated magnetic structure of $Nd_2Ir_2O_7$ in applied magnetic field using single-crystal neutron diffraction and D23 diffractometer at the Institut Laue-Langevin, Grenoble, France; and magnetic excitations in $Er_2Ir_2O_7$ and $Lu_2Ir_2O_7$ single crystals using the resonant inelastic X-ray scattering method and ID20 instrument at the European Synchrotron Radiation Facility, Grenoble, France. Since 2024, our fruitful collaboration continues in the framework of the international mobility project supported by Ministry of Education, Youth and Sports of Czech Republic; and Ministry for Europe and Foreign Affairs and Ministry of Higher Education, Research and Innovation of France, respectively. Recently, a joint experiment that will allow us to further investigate the magnetic structure in $Nd_2Ir_2O_7$ single crystal has been accepted for realisation using ZEBRA diffractometer at the Paul-Sherrer Institute, Villigen, Switzerland. In addition to that, we propose several other experiments at large-scale facilities. Namely, recently accepted experimental proposal at ESRF: synchrotron X-ray micro-diffraction mapping of magnetic domains and domain walls in $Ho_2Ir_2O_7$ single crystal is to be highlighted as it promises highly innovative results.

In addition to introduced research directions and our current intentions and plans, there is a plethora of phenomena to be studied and to be discovered in respective compounds. We restrict ourself to briefly mention just two directions, one for each series, which should be followed by investigating synthesised samples. First, the topological properties associated with the Ir sublattice and the spin-orbit interaction in the $A_2Ir_2O_7$ members. All, topological insulating states, Weyl semi-metallic state, Fermi-arc surfaces, etc., have been proposed and searched for in these materials. The experimental study was, however, severely hindered by the absence of good-quality single crystals. Second, the specifics of the defects, the bonding character, and the crystal structure of the heavy rare-earth $A_2Zr_2O_7$ members are expected to allow their use in solid oxide fuel cells, thermal barrier coatings, or nuclear waste storage. Previous studies focussing on material properties of these oxides and mainly their interpretation were highly problematic due to missing pieces of information on their structural details. These research directions, together with many others, are now open for appropriate examination, and our work contributed to that.

Bibliography

[1] *The Nobel Prize in Physics 2021. Nobel Prize Outreach AB* (2021) (https://www.nobelprize.org/ prizes/physics/2021/summary/).

[2] Wannier, G.H., *Phys. Rev.* **79**, 357 (1950).

[3] Bahrami, F., Hu, X., Du, Y., Lebedev, O., Wang, C., Luetkens, H., Fabbris, G., Graf, M.J., Haskel, D., Ran, Y., Tafti, F., *Scie. Adv.* **8**, eabl5671 (2022).

[4] Banerjee, A., Bridges, C.A., Yan, J.-Q., Aczel, A.A., Li, L., Stone, M.B., Granroth, G.E., Lumsden, M.D., Yiu, Y., Knolle, J., Bhattacharjee, S., Kovrizhin, D.L., Moessner, R., Tennant, D.A., Mandrus, D.G., Nagler, S.E., *Nature Mater.* **15**, 733 (2016).

[5] Gao, B., Chen, T., Tam, D.W., Huang, C.L., Sasmal, K., Adroja, D.T., Ye, F., Cao, H., Sala, G., Stone, M.B., Baines, C., Verezhak, J.A.T., Hu, H., Chung, J.H., Xu, X., Cheong, S.-W., Nallaiyan, M., Spagna, S., Maple, M.B., Nevidomskyy, A.H., Morosan, E., Chen, G., Dai, P., *Nature Phys.* **15**, 1052-1057 (2019).

[6] Khomskii, D.I., *Nature Commun.* **12**, 3047 (2021).

[7] Cathelin, V., Lefrancois, E., Robert, J., Guruciaga, P.C., Paulsen, C., Prabhakaran, D., Lejay, P., Damay, F., Ollivier, J., Fak, B., Chapon, L.C., Ballou, R., Simonet, V., Holdsworth, P.C.W., Lhotel, E., *Phys. Rev. Res.* **2**, 032073 (2020).

[8] Li, Y., Gegenwart, P., Tsirlin, A.A., *J. Phys.: Condens. Matter* **32**, 224004 (2020).

[9] Motome, Y., Nasu, J., *J. Phys. Soc. Jpn.* **89**, 012002 (2020).

[10] Pal, S., Kumar, V., Panda, D.P., Sundaresan, A., Mahajan, A.V., Muthu, D.V.S., Sood, A.K., *Phys. Rev. B* **105**, 235125 (2022).

[11] Lee, D.H., Joannopoulos, J.D., Negele, J.W., Landau, D.P., *Phys. Rev. Lett.* **52**, 433 (1984).

[12] Collins, M.F., Petrenko, O.A., *Can. J. Phys.* **75**, 605 (1997).

[13] Li, Y., Chen, G., Tong, W., Pi, L., Liu, J., Yang, Z., Wang, X., Zhang, Q., *Phys. Rev. Lett.* **115**, 167203 (2015).

[14] Zhu, Z., Maksimov, P.A., White, S.R., Chernyshev, A.L., *Phys. Rev. Lett.* **120**, 207203 (2018).

[15] Ortiz, B.R., Teicher, S.M.L., Hu, Y., Zuo, J.L., Sarte, P.M., Schuller, E.C., Milinda Abeykoon, A.M., Kroqstad, M.J., Rosenkranz, S., Osborn, R., Seshadri, R., Balents, L., He, J., Wilson, S.D., *Phys. Rev. Lett.* **125**, 247002 (2020).

[16] Jiang, Y.X., Yin, J.X., Denner, M.M., Shumiya, N., Ortiz, B.R., Xu, G., Guguchia, Z., He, J., Hossain, M.S., Liu, X., Ruff, J., Kautzsch, L., Zhang, S.S., Chang, G., Belopolski, I., Zhang, Q., Cochran, T.A., Multer, D., Litskevich, M., Cheng, Z.-J., Yang, X.P., Wang, Z., Thomale, R., Neupert, T., Wilson, S.D., Hasan, Z., *Nature Mater.* **20**, 1353-1357 (2021).

[17] Chen, H., Yang, H., Hu, B., Zhano, Z., Yuan, J., Xing, Y., Qian, G., Huang, G., Li, G., Ye, Y., Ma, S., Ni, S., Zhang, H., Yin, Q., Gong, C., Tu, Z., Lei, H., Tan, H., Zhou, S., Shen, C., Dong, X., Yan, B., Wang, Z., Gao, H.-J., *Nature* **599**, 222-228 (2021).

[18] Yin, J.-X., Ma, W., Cochran, T.A., Xu, X., Zhang, S.S., Tien, H.J., Shumiya, N., Cheng, G., Jiang, K., Lian, B.,Song, Z., Chang, G., Belopolski, I., Multer, D., Litskevich, M., Cheng, Z.J., Yang, X.P., Swidler, B., Zhou, H., Lin, H., Neupert, T., Wang, Z., Yao, N., Chang, T.-R., Jia, S., Hasan, Z., *Nature* **583**, 533-536 (2020).

[19] Ye, L., Kang, M., Liu, J., Cube, F. von, Wicker, C.R., Suzuki, T., Jozwiak, C., Bostwick, A., Rotenberg, E., Bell, D.C., Fu, L., Comin, R., Checkelsky, G., *Nature* **555**, 638-642 (2018).

[20] Wang, Q., Neubauer, K.J., Duan, C., Yin, Q., Fujitsu, S., Hosono, H., Ye, F., Zhang, R., Chi, S., Krycka, K., Lei, H., Dai, P., *Phys. Rev. B* **103**, 014416 (2021).

[21] Mustonen, O., Vasala, S., Sadrollahi, E., Schmidt, K.P., Baines, C., Walker, H.C., Terasaki, I., Litterst, F.J., Baggio-Saitovitch, E., Karppinen, M., *Nature Comm.* **9**, 1085 (2018).

[22] Tripathi, R., Adroja, D.T., Ritter, C., Sharma, S., Yang, C.L., Hillier, A.D., Koza, M.M., Demmel, F., Sundaresan, A., Langridge, S., Higemoto, W., Ito, T.U., Strydom, A.M., Stenning, G.B.G., Bhattacharyya, A., Keen, D., Walker, H.C., Perry, R.S., Pratt, F., Si, Q.M., Takabatake, T., *Phys. Rev. B* **106**, 064436 (2022).

[23] Hu, X., Pajerowski, D.M., Zhang, D., Podlesnyak, A., Qiu, Y., Huang, Q., Zhou, H., Klich, I., Kolesnikov, I., Stone, M.B., Lee, S.-H., *Phys. Rev. Lett.* **127**, 017201 (2021).

[24] Chillal, S., Iqhal, Y., Jeschke, H.O., Rodriguez-Rivera, J.A., Bewley, R., Manuel, P., Khalyavin, D., Steffens, P., Thomale, R., Islam, A.T.M.N., Reuther, J., Lake, B., *Nature Comm.* **11**, 2348 (2020).

[25] Boya, K., Nam, K., Kargeti, K., Jain, A., Kumar, R., Panda, S.K., Yusuf, S.M., Paulose, P.L., Voma, U.K., Kermarrec, E., Kim, K.H., Koteswararao, B., *APL Mater.* **10**, 101103 (2022).

[26] Khatua, J., Bhattacharya, S., Ding, Q.P., Vrtnik, S., Strydom, A.M., Butch, N.P., Luetkens, H., Kermarrec, E., Rao, M.S.R., Zorko, A., Furukawa, Y., Khuntia, P., *Phys. Rev. B* **106**, 104404 (2022).

[27] Jacobsen, H., Dashwood, C.D., Lhotel, E., Khalyavin, D., Manuel, P., Stewart, R., Prabhakaran, D., McMorrow, D.F., Boothroyd, A.T., *Phys. Rev. B* **101**, 104404 (2020).

[28] Guo, H., Ritter, C., Komarek, A.C., *Phys. Rev. B* **96**, 144415 (2017).

[29] Bramwell, S.T., Gingras, M.J.P., *Science* **294**, 1495-1501 (2001).

[30] Lefrancois, E., Cathelin, V., Lhotel, E., Robert, J., Lejay, P., Colin, C.V., Canals, B., Damay, F., Ollivier, J., Fak, B., Chapon, L.C., Ballou, R., Simonet, V., *Nature Comm.* **8**, 209 (2017).

[31] Stern, M., Castelnovo, C., Moessner, R., Oganesvan, V., Gopalakrishnan, S., *Phys. Rev. B* **104**, 115114 (2021).

[32] Savary, L., Balents, L., *Rep. Prog. Phys.* **80**, 016502 (2017).

[33] Pearce, M.J., Gotze, K., Szabo, A., Sikkenk, T.S., Lees, M.R., Boothroyd, A.T., Prabhakaran, D., Castelnovo, C., Goddard, P.A., *Nature Comm.* **13**, 444 (2022).

[34] Witczak-Krempa, W., Chen, G., Kim, Y.B., Balents, L., *Annu. Rev. Condens. Matter Phys.* **5**, 57-82 (2014).

[35] Li, Y., Oh, T., Song, J., Kim, M.K., Song, D., Kim, S., Chang, S.H., Kim, C., Yang, B.-J., Noh, T.W., *Adv. Mater.* **33**, 2008528 (2021).

[36] Ladovrechis, K., Meng, T., Roy, B., *Phys. Rev. B* **103**, 241116 (2021).

[37] Otsuka, Y., Yoshida, T., Kudo, K., Yunoki, S., Hatsugai, Y., *Scie. Rep.* **11**, 20270 (2021).

[38] Liang, T., Hsieh, T.H., Ishikawa, J.J., Nakatsuji, S., Fu, L., Ono, N.P., *Nature Phys.* **13**, 599 (2017).

[39] Mondal, S., Modak, M., Maji, B., Ray, M.K., Mandal, S., Mandal, S.K., Sardar, M., Banerjee, S., *Phys. Rev. B* **102**, 155139 (2020).

[40] Subramanian, M.A., Aravamudan, G., Subba Rao, G.V., *Prog. Solid St. Chem.* **15**, 55 (1983).

[41] Kezsmarki, I., Hanasaki, N., Hashimoto, D., Iguchi, S., Taguchi, Y., Miyasaka, S., Tokura, Y., *Phys. Rev. Lett.* **93**, 266401 (2004).

[42] Marck, S.C. van der, *Phys. Rev. E* **55**, 1514 (1997).

[43] Shamblin, J., Feygenson, M., Neuefeind, J., Tracy, C.L., Zhang, F., Finkeldei, S., Bosbach, D., Zhou, H., Ewing, R.C., Lang, M., *Nature Mater.* **15**, 507 (2016).

[44] Sibille, R., Lhotel, E., Hatnean, M.C., Nilsen, G.J., Ehlers, G., Cervellino, A., Ressouche, E., Frontzek, M., Zaharko, O., Pomjakushin, V., Stuhr, U., Walker, H.C., Adroja, D.T., Luetkens, H., Baines, C., Amato, A., Balakrishnan, G., Fennell, T., Kenzelmann, M., *Nature Comm.* **8**, 1 (2017).

[45] Colman, R.H., Kowalski, P., Vlášková, K., Keen, D., Connolly, E., Chater, P., Klicpera, M., to be published in 2024, very preliminary draft of the manuscript is printed at the end of present thesis.

[46] Anantharaman, A.P., Dasari, H.P., *Ceram. Int.* **47**, 4367-4388 (2021).

[47] Hussain, S., Yangping, L., *Energy Trans.* **4**, 113-126 (2020).

[48] Wen, L.C., Li, Z.P., Chen, H.S., Tseng, S.C., *J. Energy Storage* **64**, 107058 (2023).

[49] Fergus, J.W., *J. Power Sources* **162**, 30 (2006).

[50] Zhang, J., Guo, X., Jung, Y.-G., Li, L., Knapp, J., *Surf. Coatings Technol.* **323**, 18 (2017).

[51] Zhang, Y., Zhang, Z., Thorogood, G., Vance, E.R., *J. Nucl. Mater.* **432**, 545 (2013).

[52] Varnava, N., Vanderbilt, D., *Phys. Rev. B* **98**, 245117 (2018).

[53] Jadaun, P., Register, L.F., Banerjee, S.K., *PNAS* **117**, 11878 (2020).

[54] Ok, J.M., Mohanta, N., Zhang, J., Yoon, S., Okamoto, S., Choi, E.S., Zhou, H., Briggeman, M., Irvin, P., Lupini, A.R., Pai, Y.Y., Skoropata, E., Sohn, C., Li, H., Miao, H., Lawrie, B., Choi, W.S., Eres, G., Levy, J., Lee, H.N., *Sci. Adv.* **7**, eabf9631 (2020).

[55] Zhang, T., Jiang, Y., Song, Z., Huang, H., He, Y., Fang, Z., Hongming, W., Fang, C., *Nature* **566**, 475-479 (2019).

[56] Jiang, W., Huang, H., Liu, F., Wang, J.-P., Low, T., *Phys. Rev. B* **101**, 121113 (2020).

[57] Klicpera, M., Vlášková, K., Diviš, M., *J. Phys. Chem. C* **124**, 20367-20376 (2020).

[58] Antonov, V.N., Bekenov, L.V., Kukusta, D.A., *Phys, Rev. B.* **102**, 195134 (2020).

[59] Prando, G., Dally, R., Schottenhamel, W., Guguchia, Z., Baek, S.-H., Aeschlimann, R., Wolter, A.U.B., Wilson, S.D., Buchner, B., Graf, M.J., *Phys. Rev. B* **93**, 104422 (2016).

[60] Matsuhira, K., Wakeshima, M., Hinatsu, Y., Takagi, S., *J. Phys. Soc. Japan* **80**, 094701 (2011).

[61] Lefrancois, E., Simonet, V., Ballou, R., Lhotel, E., Hadj-Azzem, A., Kodjikian, S., Lejay, P., Manuel, P., Khalyavin, D., Chapon, L.C., *Phys. Rev. Lett.* **114**, 247202 (2015).

[62] Klicpera, M., Vlášková, K., Staško, D., Guidi, T., Puente Orench, I., Diviš, M., *Phys. Rev. B* **106**, 094408 (2022).

[63] Ueda, K., Oh, T., Yang, B.-J., Kaneko, R., Fujioka, J., Nagaosa, N., Tokura, Y., *Nature Comm.* **8**, 15515 (2017).

[64] Wu, Y., Li, X., Xie, J., *J. Low Temp. Phys.* **202**, 48 (2021).

[65] Liu, W., Han, H., Ma, L., Pi, L., Zhang, L., Zhang, Y., *J. Alloys Comp.* **741**, 182-187 (2018).

[66] Ueda, K., Kaneko, R., Subedi, A., Minola, M., Kim, B., Fujioka, J., Tokura, Y., Keimer, B., *Phys. Rev. B* **100**, 115157 (2019).

[67] Xu, L., Gong, G., Zhao, C., Song, X., Yuan, S., Tian, Z., *J. Phys. Chem. C* **124**, 22656-22662 (2020).

[68] Anand, V.K., Bera, A.K., Xu, J., Herrmannsdörfer, T., Ritter, C., Lake, B., *Phys. Rev. B* **92**, 1-10 (2015).

[69] Li, Q.J., Xu, L.M., Fan, C., Yhang, F.B., Lv, Z.Z., Ni, B., Zhao, Z.Y., Sun, X.F., *J. Cryst. Growth* **377**, 96-100 (2013).

[70] Hatnean, M.C., Lees, M.R., Balakrishnan, G., *J. Cryst. Growth* **418**, 1-6 (2013).

[71] Vlášková, K., Colman, R.H., Proschek, P., Čapek, J., Klicpera, M., *Phys. Rev. B* **100**, 1-9 (2019).

[72] Vlášková, K., Proschek, P., Pospíšil, J., Klicpera, M., *J. Cryst. Growth* **546**, 125783 (2020).

[73] Radha, A.V., Ushakov, S.V., Navrotsky, A., *J. Mater. Res.* **24**, 3350-3357 (2009).

[74] Sun, J., Hu, Z., Li, J., Zhang, H., Sun, C., *Ceramics Inter.* **40**, 11787-11793 (2014).

[75] Torres-Rodriguez, J., Gutierrez-Cano, V., Menelaou, M., Kaštyl, J., Cihlář, C., Tkachenko, S., González, J., Kalmár, J., Fabián, I., Lázár, I., Čelko, L., Kaiser, J., *Inorg. Chem.* **58**, 14467-14477 (2019).

[76] Millican, J.N., Macaluso, R.T., Nakatsuji, S., Machida, Y., Maeno, Y., Chan, J.Y., *Mater. Res. Bull.* **42**, 928-934 (2007).

[77] Hallas, A.M., Arevalo-Lopez, A.M., Sharma, A.Z., Munsie, T., Attfield, J.P., Wiebe, C.R., Luke, G.M., *Phys. Rev. B* **91**, 1-9 (2015).

[78] Hoekstra, H.R., Gallagher, F., *Inorg. Chem.* **7**, 2553-2557 (1968).

[79] Haghighirad, A.A., Ritter, F., Assmus, W., *Crys. Growth. Des.* **7**, 5-9 (2008).

[80] Shimakawa, Y., Kubo, Y., *Phys. Rev. B* **59**, 59 (1999).

[81] Peng, W., Hu, B., Yan, C., Hu, W.W., Guo, L., Yuan, H.M., Feng, S.-H., *Chem. Res. Chinese Univ.* **27**, 161-165 (2011).

[82] Rodríguez-Carvajal, J., *Phys. B* **192**, 55-69 (1993).

[83] Zhou, Y.C., Rahaman, M.N., *J. Mater. Res.* **8**, 1680-1686 (1993).

[84] Jehn, H., *J. Less-common Met.* **100**, 321-339 (1984).

[85] Lide, D., *CRC Handbook of Chemistry and Physics* **57** (2003).

[86] Vlášková, K., Colman, R.H., Klicpera, M., *Mater. Chem. Phys.* **258**, 123868 (2021).

[87] Laudise, R.A., Nielsen, J.W., *Hydrotherm. Crys. Growth.*, 149-221 (1961).

[88] Koo, H.-J., Whangbo, M.-H., Kennedy, B.J., *J. Solid State Chem.* **136**, 269 (1998).

[89] Das, M., Bhowal, S., Sannigrahi, J., Bandyopadhyay, A., Banerjee, A., Cibin, G., Khalyavin, D., Banerjee, N., Adroja, D., Dasgupta, I., Majumdar, S., *Phys. Rev. B* **105**, 134421 (2022).

[90] Staško, D., Vlášková, K., Kancko, A., Többens, D.M., Daisenberger, D., Garbarino, G., Colman, R.H., Klicpera, M., *arXiv:2403.00477* (2024).

[91] Birch, F., *J. Geophys. Res.* **57**, 227-286 (1952).

[92] Machida, Y., Nakatsuji, S., Maeno, Y., Tayama, T., Sakakibara, T., Onoda, S., *Phys. Rev. Lett.* **98**, 57203 (2007).

[93] Ueda, K., Fujioka, J., Yang, B.-J., Shiogai, J., Tsukazaki, A., Nakamura, S., Awaji, S., Nagaosa, N., Tokura, Y., *Phys. Rev. Lett.* **115**, 56402 (2015).

[94] Ishikawa, J.J., O'Farrell, E.C.T., Nakatsuji, S., *Phys. Rev. B* **85**, 245109 (2012).

[95] Tafti, F.F., Ishikawa, J.J., McCollam, A., Nakatsuji, S., Julian, S.R., *Phys. Rev. B* **85**, 245109 (2012).

[96] Balakrishnan, G., Peterenko, A.O., Lees, M.R., Paul, D.McK., *J. Phys.: Conden. Matter* **10**, 723-725 (1998).

[97] Prabhakaran, D., Boothroyd, A.T., *J. Crys. Growth* **318**, 1053-1056 (2011).

[98] Zajíc, F., Klejch, M., Eliáš, A., Klicpera, M., Beitlerová, A., Nikl, M., Pospíšil, J., *Cryst. Growth Des.* **23**, 2609-2618 (2023).

[99] Staško, D., Vlášková, K., Vojtasová, D., Hájek, F., Král, P., Colman, R.H., Klicpera, M., *SSRN:4684275* (2024).

[100] Ouladdiaf, B., Archer, J., Allibon, J.R., Decarpentrie, P., Lemée-Cailleau, M.-H., Rodrígez-Carvajal, J., Hewat, A.W., York, S., Brauc, D., McIntyre, J., *J. App. Crystal.* **44**, 392-397 (2011).

[101] Guo, H., Ritter, C., Komarek, A.C., *Phys. Rev. B* **94**, 161102 (2016).

[102] Wang, Y., Weng, H., Fu, L., Dai, X., *Phys. Rev. Lett.* **119**, 187203 (2017).

[103] Tokiwa, Y., Ishikawa, J.J., Nakatsuji, S., *Nature Mat.* **13**, 356 (2014).

[104] Moore, J.E., *Nature* **464**, 194 (2010).

[105] Qi, X.-L., Zhang, S.-C., *Phys. Today* **63**, 33 (2010).

[106] Pesin, D.A., Balents, L., *Nature Phys.* **6**, 376 (2010).

[107] Wan, X., Turner, A.M., Vishwanath, A., Savrasov, S.Y., *Phys. Rev. B* **83**, 205101 (2011).

[108] Witzak-Krempa, W., Kim, Y.B., *Phys. Rev. B* **85**, 045124 (2012).

[109] Sushov, A.B., Hofmann, J.B., Jenkins, G.S., Ishikawa, J., Nakatsuji, S., Das Sarma, S., Drew, H.D., *Phys. Rev. B* **92**, 241108 (2015).

[110] Jaiswal, A.K., Wang, D., Wollersen, V., Schneider, R., Le Tacon, M., Fuchs, D., *Adv. Mater.* **134**, 2109163 (2022).

[111] Ueda, K., Moriuchi, N., Fukushima, K., Kida, T., Hagiwara, M., Matsuno, J., *Phys. Rev. Applied* **16**, 034039 (2021).

[112] Disseler, S.M., Dhital, Ch., Amato, A., Giblin, S.R., Cruz, C. de la, Wilson, S.D., Graf, M.J., *Phys. Rev. B* **86**, 014428 (2012).

[113] Donnerer, C., Rahn, M.C., Moretti Sala, M., Vale, J.G., Pincini, D., Strempfer, J., Krisch, M., Prabhakaran, D., Boothroyd, A.T., McMorrow, D.F., *Phys. Rev. Lett.* **117**, 037201 (2016).

[114] Sagayama, H., Uematsu, D., Arima, T., Sugimoto, K., Ishikawa, J.J., O'Farrell, E., Nakatsuji, S., *Phys. Rev. B* **87**, 100403 (2013).

[115] Disseler, S.M., *Phys. Rev. B* **89**, 140413 (2014).

[116] Vlášková, K., Proschek, P., Diviš, M., Le, D., Colman, R.H., Klicpera, M., *Phys. Rev. B* **102**, 054428 (2020).

[117] Klicpera, M., Vlášková, K., Diviš, M., *J. Magn. Magn. Mater.* **506**, 166793 (2020).

[118] Colman, R.H., Vlášková, K., Berlie, A., Klicpera, M., *arXiv:2012.14730* (2020).

[119] Staško, D., Vlášková, K., Proschek, P., Klicpera, M., *J. Phys. Chem. Solids* **176**, 111268 (2023).

[120] Vlášková, K., Diviš, M., Klicpera, M., *J. Magn. Magn. Mater.* **538**, 168220 (2021).

[121] Rajeev, H.S., Telang, P., Singh, S., *Solid State Comm.* **312**, 113863 (2020).

[122] Sleight, A.W., Ramirez, A.P., *Solid State Comm.* **275**, 12 (2018).

[123] Rodionov, Y.I., Syzranov, S.V., *Phys. Rev. B* **91**, 195107 (2015).

[124] LaBarre, P.G., Dong, L., Trinh, J., Siegrist, T., Ramirez, A.P., *J. Phys.: Condens. Matter* **32**, 02LT01 (2020).

[125] Slater, J.C., *Phys. Rev.* **82**, 538 (1951).

[126] Calder, S., Garlea, V.O., McMorrow, D.F., Lumsden, M.B., Stone, M.B., Lang, J.C., Kim, J.-W., Schlueter, J.A., Shi, Y.G., Yamaura, K., Sun, Y.S., Tsujimoto, Y., Christianson, A.D., *Phys. Rev. Lett.* **108**, 257209 (2012).

[127] Mandrus, D., Thompson, J.R., Gaal, R., Forro, L., Bryan, J.C., Chakoumakos, B.C., Woods, L.M., Sales, B.C., Fishman, R.S., Keppens, V., *Phys. Rev. B* **63**, 195104 (2001).

[128] Feng, Y., Wang, Y., Silevitch, D.M., Cooper, S.E., Mandrus, D., Lee, P.A., Rosenbaum, T.F., *Nature Comm.* **12**, 2779 (2021).

[129] Hiroi, Z., Zamaura, J., Hirose, T., Nagashima, I., Okamoto, Y., *APL Mater.* **3**, 041501 (2015).

[130] Banerjee, A., Sannigrahi, J., Giri, S., Majumdar, S., *Phys. Rev. B* **96**, 224426 (2017).

[131] Arita, R., Kuneš, J., Kozhevnikov, A.V., Eguiluz, A.G., Imada, M., *Phys. Rev. Lett.* **108**, 086403 (2012).

[132] Martins, C., Aichhorn, M., Vaugier, L., Biermann, S., *Phys. Rev. Lett.* **107**, 266404 (2011).

[133] Nakayama, M., Kondo, T., Tian, Z., Ishikawa, J.J., Halim, M., Bareille, C., Malaeb, W., Kuroda, K., Tomita, T., Ideta, S., Tanaka, K., Matsunami, M., Kimura, S., Inami, N., Ono, K., Kumigashira, H., Balents, L., Nakatsuji, S., Shin, S., *Phys. Rev. Lett.* **117**, 056403 (2016).

[134] Takatsu, H., Watanabe, K., Goto, K., Kadowaki, H., *Phys. Rev. B* **90**, 235110 (2014).

[135] Ueda, K., Fujioka, J., Terakura, C., Tokura, Y., *Phys. Rev. B* **92**, 121110 (2015).

[136] Zhao, S., Mackie, J.M., MacLaughlin, D.E., Bernal, O.O., Ishikawa, J.J., Ohta, Y., Nakatsuji, S., *Phys. Rev. B* **83**, 180402 (2011).

[137] Clancy, J.P., Gretarsson, H., Lee, E.K.H., Tian, D., Kim, J., Upton, M.H., Casa, D., Gog, T., Islam, Z., Jeon, B.-G., Kim, K.H., Desgreniers, S., Kim, Y.B., Julian, S.J., Kim, Y.-J., *Phys. Rev. B* **94**, 024408 (2016).

[138] Thomas, A., Telang, P., Mishra, K., Cesnek, M., Bednarcik, J., Muthu, D.V.S., Singh, S., Sood, A.K., *Phys. Rev. B* **105**, 075145 (2022).

[139] Feng, Y., Bian, J., Chen, S., Fang, B., Tong, W., Liu, H., *J. Supercond. Nov. Magn.* **32**, 3979 (2019).

[140] Prando, G., Telang, P., Wilson, S.D., Graf, M.J., Singh, S., *Phys. Rev. B* **101**, 174435 (2020).

[141] Zhu, W.K., Wang, M., Seradjeh, B., Yang, F., Zhang, S.X., *Phys. Rev. B* **90**, 054419 (2014).

[142] Liu, H., Bian, J., Chen, S., Wang, J., Feng, Y., Tong, W., Xie, Y., Fang, B., *J. Magn. Magn. Mater.* **498**, 166214 (2020).

[143] Wang, Y., Rosenbaum, T.F., Prabhakaran, D., Boothroyd, A.T., Feng, Y., *Phys. Rev. B* **101**, 220404 (2020).

[144] Sakata, M., Kagayama, T., Shimizu, K., Matsuhira, K., Takagi, S., Wakeshima, M., Hinatsu, Y., *Phys. Rev. B* **83**, 041102 (2011).

[145] Hirose, H.T., Yamaura, J., Hiroi, Z., *Scie. Rep.* **7**, 42440 (2017).

[146] Jing, R., Xiong, L., Hirose, H.T., Shao, Y., Mcleod, A.S., Chen, X., Liu, M., Hiroi, Z., Basov, D.N., *EPL - Europhys. Lett.* **137**, 56001 (2022).

[147] Ma, E.Y., Cui, Y.-T., Ueda, K., Tang, S., Chen, K., Tamura, N., Wu, P.M., Fujioka, J., Tokura, Y., Shen, Z.-X., *Science* **350**, 538 (2015).

[148] Tian, Z., Kohama, Y., Tomita, T., Ishizuka, H., Hsieh, T.H., Ishikawa, J.J., Kindo, K., Balents, L., Nakatsuji, S., *Nature Phys.* **12**, 134 (2016).

[149] Fujita, T.C., Uchida, M., Kozuka, Y., Ogawa, S., Tsukazaki, A., Arima, T., Kawasaki, M., *App. Rev. Lett.* **108**, 022402 (2016).

[150] Evans, P.G., Marks, S.D., Geprags, S., Dietlein, M., Joly, Y., Dai, M., Hu, J., Bouchenoire, L., Thompson, P.B.J., Schulli, T.U., Richard, M.-I., Gross, R., Carbone, D., Mannix, D., *Scie. Adv.* **6**, 9351 (2020).

[151] Tardif, S., Takeshita, S., Ohsumi, H., Yamaura, J., Okuyama, D., Hiroi, Z., Takata, M., Arima, T., *Phys. Rev. Lett.* **114**, 147205 (2015).

[152] Chauleau, J.-Y., Chirac, T., Fusil, S., Garcia, V., Akhtar, W., Tranchida, J., Thibaudeau, P., Gross, I., Blouzon, C., Finco, A., Bibes, M., Dkhil, B., Khalyavin, D.D., Manuel, P., Jacques, V., Jaouen, N., Viret, M., *Nature Mater.* **19**, 386 (2020).

[153] Asih, R., Noraina, A., Mohd-Tajudin, S.S., Matsuhira, K., Guo, H., Wakeshima, M., Hinatsu, Y., Nakano, T., Nozue, Y., Sulaiman, S., Mohamen-Ibrahim, M.I., Biswas, P.K., Watanabe, I., *J. Phys. Soc. Jpn.* **86**, 024705 (2017).

[154] Yanagishima, D., Maeno, Y., *J. Phys. Soc. Jpn.* **70**, 2880 (2001).

[155] Ross, K.A., Savary, L., Gaulin, B.D., Balents, L., *Phys. Rev. X* **1**, 021002 (2011).

[156] Gaudet, J., Hallas, A.M., Kolesnikov, A.I., Gaulin, B.D., *Phys. Rev. B* **97**, 024415 (2018).

[157] Hozoi, L., Gretarsson, H., Clancy, J.P., Jeon, B.-G., Lee, B., Kim, K.H., Yushankhai, V., Fulde, P., Casa, D., Gog, T., Kim, J., Said, A.H., Upton, M.H., Kim, Y.-J., Brink, J. van den, *Phys. Rev. B* **89**, 115111 (2014).

[158] Uematsu, D., Sagayama, H., Arima, T., Ishikawa, J.J., Nakatsuji, S., Takagi, H., Yoshida, M., Mizuki, J., Ishii, K., *Phys. Rev. B* **92**, 094405 (2015).

[159] The Materials Project. Materials Data on Tm2O3 by Materials Project. United States. , *https://doi.org/10.17188/1192617*.

[160] Chateliére, T., Ruggiero, J., Le Gouet, J.-L., Tittel, W., Mun, J.-H., Jouini, A., Yoshikawa, A., Boulon, G., Du, Y.L., Goldner, Ph., Beaudoux, F., Vincent, J., Antic-Fidancev, E., Guillot-Noel, O., *Phys. Rev. B* **77**, 245127 (2008).

[161] Gondek, L., Kaczorowski, D., Szytula, A., *Solid State Comm.* **150**, 368 (2010).

[162] Freeman, A.J., Desclaux, J.P., *J. Magn. Magn. Mater.* **12**, 11-21 (1979).

[163] Bertin, A., Chapuis, Y., Dalmas de Reotier, P., Yaouanc, A., *J. Phys.: Condens. Matter* **24**, 256003 (2012).

[164] Zinkin, M.P., Harris, M.J., Tun, Z., Cowley, R.A., Wanklyn, B.M., *J. Phys.: Condens. Matter* **8**, 193 (1996).

[165] Lefrancois, E., Mangin-Thro, L., Lhotel, E., Robert, J., Petit, S., Cathelin, V., Fischer, H.E., Colin, C.V., Damay, F., Ollivier, J., Lejay, P., Chapon, L.C., Simonet, V., Ballou, R., *Phys. Rev. B* **99**, 060401 (2019).

[166] Nakatsuji, S., Machida, Y., Maeno, Y., Tayama, T., Sakakibara, T., Duijn, J. van, Balicas, L., Millican, J.N., Macaluso, R.T., Chan, J.Y., *Phys. Rev. Lett.* **96**, 087204 (2006).

[167] Tian, Z., Kohama, Y., Tomito, T., Ishizuka, H., Hsieh, T.H., Ishikawa, J.J., Kindo, K., Balents, L., Nakatsuji, S., *Nature Phys.* **12**, 134 (2015).

[168] Yang, W.C., Zhu, W.K., Zhou, H.D., Ling, L., Choi, E.S., Lee, M., Losovyj, Y., Lu, C.-K., Zhang, S.X., *Phys. Rev. B* **96**, 094437 (2017).

[169] Petit, S., Lhotel, E., Canals, B., Hatnean, M.C., Ollivier, J., Mutka, H., Ressouche, E., Wildes, A.R., Lees, M.R., Balakrishnan, G., *Nature Phys.* **12**, 746-750 (2016).

[170] Wen, J.-J., Koohpayeh, S.M., Ross, K.A., Trump, B.A., McQueen, T.M., Kimura, K., Nakatsuji, S., Qiu, Y., Pajerowski, D.M., Copley, J.R.D., Broholm, C.L., *Phys. Rev. Lett.* **118**, 107206 (2017).

[171] Sardar, S., Kale, G., Ghadiri, M., *Ceram. Int.* **46**, 11508-11514 (2020).

[172] He, J., Huang, Y., Hu, M., Jiang, M., Qiao, Y., Li, S., Zeng, H., *Mater. Res. Express* **7**, 055201 (2020).

[173] Wang, Y., Gao, B., Wang, Q., Li, X., Su, Z., Chang, A., *J. Mater. Sci.* **55**, 15405-15414 (2020).

[174] Yang, K., Wang, Y., Lei, P., Yao, T., Zhao, D., Lian, J., *Eur. Ceram. Soc.* **41**, 6018-6028 (2021).

[175] O'Quinn, E.C., Drey, D.L., Lang, M.K., *Front. Chem.* **9**, 733718 (2021).

[176] Simeone, D., Thorogood, G.J., Huo, D., Luneville, L., Baldinozzi, G., Petříček, J., Forcher, F., Ribis, J., Mazerolles, L., Largeau, L., Berar, J.F., Surble, S., *Sci. Rep.* **7**, 3727 (2017).

[177] Klicpera, M., Staško, D., Vlášková, K., Hájek, F., Vojtasová, D., Zelenka, J., Colman, R.H., *J. Alloys Comp.* **978**, 173440 (2024).

[178] Bhardwaj, A., Zhang, S., Yan, H., Moessner, R., Nevidomskyy, A.H., Changlani, H.J., *npj Quantum Mater.* **7**, 51 (2022).

[179] Norman, M.R., *Rev. Mod. Phys.* **88**, 041002 (2016).

[180] Petit, S., Lhotel, E., Guitteny, S., Florea, O., Robert, J., Bonville, P., Mirebeau, I., Ollivier, J., Mutka, H., Ressouche, E., Decorse, C., Hatnean, M.C., Balakrishnan, G., *Phys. Rev. B* **94**, 165153 (2016).

[181] Bahamirian, M., Bastani, A., Hasani, S., Farvizi, M., Seifoddini, A., *Ceram. Int.* **49**, 16717-16731 (2023).

[182] Solomon, J., Shamblin, J., Lang, M., Navrotsky, A., Asta, M., *Sci. Rep.* **6**, 38772 (2016).

[183] Zhang, F.X., Lang, M., Ewing, R.C., *Appl. Phys. Lett.* **106**, 191902 (2015).

[184] Rittman, D.R., Turner, K.M., Park, S., Fuentes, A.F., Yan, J., Ewing, R.C., Mao, W.L., *J. Appl. Phys.* **121**, 045902 (2017).

[185] Xu, Y., Man, H., Tang, N., Baidya, S., Zhang, H., Nakatsuji, S., Vanderbilt, D., Drichko, N., *Phys. Rev. B* **104**, 075125 (2021).

[186] Lutique, S., Javorský, P., Konings, R.J.M., Krupa, J.-C., Genderen, A.C.G. van, Miltenburg, J.C. van, Wastin, F., *J. Chem. Thermodynamics* **36**, 609-618 (2004).

[187] Durand, A.M., Klavins, P., Corruccini, L.R., *J. Phys.: Condens. Matter.* **20**, 235208 (2008).

[188] Klicpera, M., Vlášková, K., Colman, R.H., Proschek, P., Hoser, A., *Acta Phys. Pol.* **137**, 750-752 (2020).

[189] Wang, C.W., Ishida, L., Bernardo, P.L., Leite, M.M., Vichi, F.M., Gardner, J.S., Freitas, R.S., *Phys. Rev. B* **99**, 214442 (2019).

[190] Sheetal, Biswas, P.K., Yokoyama, K., Adroja, D.T., Yadav, C.S., *arXiv:2303.14426v1.*

[191] Sheetal, Yadav, C.S., *J. Magn. Magn. Mater.* **553**, 169255 (2022).

[192] Sheetal, Elghandour, A., Klingeler, R., Yadav, C.S., *J. Phys.: Condens. Matter* **34**, 245801 (2022).

[193] Paddison, J.A.M., Ehlers, G., Cairns, A.B., Gardner, J.S., Petrenko, O.A., Butch, N.P., Khalyavin, D.D., Manuel, P., Fisher, H.E., Zhou, H., Goodwin, A.L., Stewart, J.R., *npj Quantum Mater.* **6**, 99 (2021).

[194] Samarakoon, A.M., Grigera, S.A., Tennant, D.A., Kirste, A., Klemke, B., Strehlow, P., Meissner, M., Hallén, J.N., Jaubert, L., Castelnovo, C., Moessner, R., *PNAS* **119**, e2117453119 (2022).

[195] Fennell, T., Deen, P.P., Wildes, A.R., Schmalzl, K., Prabhakaran, D., Boothroyd, A.T., Aldus, R.J., McMorrow, D.F., Bramwell, S.T., *Science* **326**, 415-417 (2009).

[196] Petit, S., Robert, J., Guitteny, S., Bonville, P., Decorse, C., Ollivier, J., Mutka, H., Gingras, M.J.P., Mirebeau, I., *Phys. Rev. B* **90**, 060410 (2014).

[197] Li, S.J., Che, H.L., Wu, J.C., Zhao, X., Sun, X.F., *AIP Adv.* **8**, 055705 (2018).

[198] Vojtasová, D., Staško, D., Hájek, F., Colman, R.H., Klicpera, M., *J. Phys.: Conden. Matter*, accepted manuscript (2024), DOI: 10.1088/1361-648X/ad483f.

[199] Lhotel, E., Petit, S., Guitteny, S., Florea, O., Ciomaga Hatnean, M., Colin, C., Ressouche, E., Lees, M.R., Balakrishnan, G., *Phys. Rev. Lett.* **115**, 197202 (2015).

[200] Bissengaliyeva, M.R., Knyazev, A.V., Bespyatov, M.A., Gogol, D.B., Taimassova, S.T., Zhakupov, R.M., Sadyrbekov, D.T., *J. Chem. Thermodyn.* **165**, 106646 (2022).

[201] Ramirez, A.P., *Annu. Rev. Mater. Sci.* **24**, 453 (1994).

[202] Rehn, J., Moessner, R., *Philos. Trans. R. Soc. A Math. Phys. Eng. Sci.* **374** (2016).

[203] Gardner, J.S., Gingras, M.J.P., Greedan, J.E., *Rev. Mod. Phys.* **82**, 53 (2010).

[204] Yastrebtsev, A.A., Popov, V.V., Menushenkov, A.P., Beskrovnyi, A.I., Neov, D.S., Shchetinin, I.V., Ponkratov, K.V., *J. Alloys Compd.* **832**, 154863 (2020).

[205] Man, H., Ghasemi, A., Adnani, M., Siegler, M.A., Anber, E.A., Li, Y., Chien, C.-L., Taheri, M.L., Chu, C.-W., Broholm, C.L., Koohpayeh, S.M., *Phys. Rev. Mater.* **7**, 063401 (2023).

[206] Sickafus, K.E., Minervini, L., Grimes, R.W., Valdez, J.A., Ishimaru, M., Li, F., McClellan, K.J., Hartmann, T., *Science* **289**, 748 (2000).

[207] Farmer, J.M., Boatner, L.A., Chakoumakos, B.C., Du, M.-H., Lance, M.J., Rawn, C.J., Bryan, J.C., *J. Alloys Compd.* **605**, 63 (2014).

[208] Turner, K.M., Rittman, D.R., Heymach, R.A., Tracy, C.L., Turner, M.L., Fuentes, A.F., Mao, W.L., Ewing, D.R., *J. Phys.: Condens. Matter* **29**, 255401 (2006).

[209] Mandal, B.P., Garg, N., Sharma, S.M., Tyagi, A.K., *J. Solid State Chem.* **179**, 1990 (2006).

[210] Guskov, A.V., Gagarin, P.G., Guskov, V.N., Khoroshilov, A.V., Gavrichev, K.S., *Inorg. Mater.* **172**, 1990 (2022).

[211] Popov, V.V., Menushenkov, A.P., Yastrebtsev, A.A., Zubavichus, Ya.V., Gavrichev, K.S., *J. Phys.: Conf. Ser.* **747**, 012043 (2016).

[212] Taira, N., Wakeshima, M., Hinatsu, Y., *J. Phys.: Condens. Matter* **13**, 5527 (2001).

[213] Denisova, L.T., Kargin, Y.F., Chumilina, L.G., Ryabov, V.V., Belousova, N.V., Denisov, V.M., *Inorg. Mater.* **54**, 815 (2018).

[214] Stokes, H.T., Hatch, D.M., Campbell, B.J., *ISODISTORT, ISOTROPY Software Suite* **iso.byu.edu**.

[215] Campbell, B.J., Stokes, H.T., Tanner, D.E., Hatch, D.M., *J. Appl. Cryst.* **39**, 607-614 (2006).

[216] Li, Y., Kowalski, P.M., Beridze, G., Birnie, A.R., Finkeldei, S., Bosbach, D., *Scr. Mater.* **107**, 18-21 (2015).

[217] Li, Y., Kowalski, P.M., *J. Nucl. Mater.* **505**, 255-261 (2018).

[218] Finkeldei, S., Kegler, P., Kowalski, P.M., Schreinemachers, C., Brandt, F., Bukaemskiy, A., Vinograd, V., Beridze, G., Shelyug, A., Navrotsky, A., Bosbach, D., *Acta Mater.* **125**, 166-176 (2017).

[219] Kowalski, P.M., *Scr. Mater.* **189**, 7-10 (2020).

[220] Zunger, A., Wei, S.-H.., Ferreira, L.G., Bernard, J.E., *Phys. Rev. Lett.* **65**, 353-356 (1990).

[221] Zelenka, J., *Development of crystal structure of (Er,Lu)$_2$(Ti,Zr)$_2$O$_7$ materials.* Bachelor thesis under supervision of Klicpera, M., Prague: Charles University, Faculty of Mathematics and Physics, Department of Condensed Matter Physics (2023).

[222] Kennedy, B.J., Zhou, Q., Avdeev, M., *J. Solid State Chem.* **184**, 1695-1698 (2011).

[223] Colman, R.H., Klicpera, M., Staško, D., *Temperature evolution of crystallographic parameters in pyrochlore iridates [dataset]. European Synchrotron Radiation Facility.* doi.org/10.15151/ESRF-ES-1178037339, (2023).

[224] Klicpera, M., *Magnetic and lattice excitations in pyrochlore-fluorite series Er$_2$(Ti,Zr)$_2$O$_7$. STFC ISIS Neutron and Muon Source.* doi.org/10.5286/ISIS.E.RB2220424, (2023).

6. List of attached publications ¶

The list of 17 publications authored and co-authored by Milan Klicpera. The publications are listed in chronological order (since 2019). Only publications related to the subject of the submitted thesis are listed. Milan Klicpera has been usually first author or last author, i.e., group leader, and corresponding author of listed publications. Other publications (total number of publications >70) of the author are listed in his Curriculum vitae and they are accessible via Web of Science and SCOPUS portals.

In addition to bibliographic information on the publication activity, the author's contribution to the respective publication is listed (♠). At the same time, the relation of the publication to the respective chapters and sections of the present thesis is indicated (♣).

1. **Evidence for spin-glass ground state in fluorite-defect $Er_2Zr_2O_7$ single crystals**

   Vlášková, K., Colman, R.H., Proschek, P., Čapek, J., Klicpera, M.

   ***Phys. Rev. B* 100**, 214405 (2019)

   DOI: 10.1103/PhysRevB.100.214405

   ♠ *MK's contribution:* 60%; conceptualisation, sample synthesis and characterisation, manuscript editing

   ♣ *introduced by thesis sections:* chapter 2, section 2.3, chapter 3, section 4.1, section 4.2, and section 4.3

2. **Low-temperature properties of pyrochlore $Lu_2Ir_2O_7$**

   Klicpera, M., Vlášková, K., Diviš, M.

   ***J. Magn. Magn. Mater.* 506**, 166793 (2020)

   DOI: 10.1016/j.jmmm.2020.166793

   ♠ *MK's contribution:* 70%; conceptualisation, sample characterisation, manuscript writting and editing

   ♣ *introduced by thesis sections:* chapter 2, section 2.1, chapter 3, and section 3.1

3. **Spin-glass state in a defect-fluorite $Er_2Zr_2O_7$**

   Klicpera, M., Vlášková, K., Colman, R.H., Proschek, P., Hoser, A.

   ***Acta Phys. Pol. A* 137**, 753-755 (2020)

   DOI: 10.12693/APhysPolA.137.753

♠ *MK's contribution:* 60%; conceptualisation, sample synthesis, manuscript writting and editing

♣ *introduced by thesis sections:* section 2.3, chapter 3, section 4.1, section 4.2, and section 4.3

4. **Magnetic properties and crystal field splitting of the rare-earth pyrochlore $Er_2Ir_2O_7$**

   Vlášková, K., Proschek, P., Diviš, M., Le, D., Colman, R.H., Klicpera, M.

   ***Phys. Rev. B* 102**, 054428 (2020)

   DOI: 10.1103/PhysRevB.102.054428

   ♠ *MK's contribution:* 80%; conceptualisation, neutron scattering data measurement, processing and analysis, manuscript writting and editing

   ♣ *introduced by thesis sections:* chapter 3, and section 3.2

5. **High temperature structural study on an $Er_2Ti_2O_7$ single crystal**

   Vlášková, K., Vondráčková, B., Daniš, S., Klicpera, M.

   ***Acta Phys. Pol. A* 137**, 750-752 (2020)

   DOI: 10.12693/APhysPolA.137.750

   ♠ *MK's contribution:* 40%; conceptualisation, sample synthesis, manuscript editing

   ♣ *introduced by thesis sections:* section 2.3, chapter 4, and section 4.3

6. **Low-temperature study of an $Er_2Ti_2O_7$ single crystal synthesized by floating zone technique and simplified feed rod preparation route**

   Vlášková, K., Proschek, P., Pospíšil, J., Klicpera, M.

   ***J. Cryst. Growth* 546**, 125783 (2020)

   DOI: 10.1016/j.jcrysgro.2020.125783

   ♠ *MK's contribution:* 60%; conceptualisation, sample synthesis, manuscript editing

   ♣ *introduced by thesis sections:* chapter 2, section 2.3, chapter 4, and section 4.3

7. **Characterisation and magnetic properties of heavy rare-earth $A_2Ir_2O_7$ pyrochlore iridates, the case of $Tm_2Ir_2O_7$**

Klicpera, M., Vlášková, K., Diviš, M.

***J. Phys. Chem. C* 124**, 20367-20376 (2020)

DOI: 10.1021/acs.jpcc.0c04847

♠ *MK's contribution:* 70%; conceptualisation, sample characterisation, manuscript writting and editing

♣ *introduced by thesis sections:* chapter 2, section 2.1, chapter 3, section 3.1, and section 3.2

8. **Spin dynamics in the pyrochlore iridate, $Er_2Ir_2O_7$, investigated by muSR spectroscopy**

   Colman, R.H., Vlášková, K., Berlie, A., Klicpera, M.,

   arXiv (2020)

   DOI: 10.48550/arXiv.2012.14730

   ♠ *MK's contribution:* 30%; conceptualisation, sample characterisation, manuscript editing

   ♣ *introduced by thesis sections:* chapter 3, and section 3.1

9. **Synthesis of $Er_2Ir_2O_7$ pyrochlore iridate by solid-state-reaction and CsCl flux method**

   Vlášková, K., Colman, R.H., Klicpera, M.,

   ***Mater. Chem. Phys.* 258**, 123868 (2021)

   DOI: 10.1016/j.matchemphys.2020.123868

   ♠ *MK's contribution:* 40%; conceptualisation, sample synthesis and characterisation, manuscript editing

   ♣ *introduced by thesis sections:* chapter 2, and section 2.1

10. **The magnetic behaviour of $Dy_2Ir_2O_7$ – Beyond the mean field approximation**

    Vlášková, K., Diviš, M., Klicpera, M.

    ***J. Magn. Magn. Mater.* 538**, 168220 (2021)

    DOI: 10.1016/j.jmmm.2021.168220

    ♠ *MK's contribution:* 30%; conceptualisation, manuscript editing

    ♣ *introduced by thesis sections:* chapter 3, section 3.1, and section 3.2

11. **Neutron scattering study of the $Tm_2Ir_2O_7$ pyrochlore iridate**

    Klicpera, M., Vlášková, K., Staško, D., Guidi, T., Puente Orench, I., Diviš, M.

    ***Phys. Rev. B* 106**, 094408 (2022)

    DOI: 10.1103/PhysRevB.106.094408

    ♠ *MK's contribution:* 80%; conceptualisation, sample synthesis and characterisation, neutron scattering data processing and analysis, manuscript writting and editing

    ♣ *introduced by thesis sections:* chapter 3, and section 3.2

12. **Conductive properties of heavy-rare-earth $A_2Ir_2O_7$ iridates synthesized by the CsCl-flux method**

    Staško, D., Vlášková, K., Proschek, P., Klicpera, M.

    ***J. Phys. Chem. Solids* 176**, 111268 (2023)

    DOI: 10.1016/j.jpcs.2023.111268

    ♠ *MK's contribution:* 60%; conceptualisation, sample synthesis, manuscript writting and editing

    ♣ *introduced by thesis sections:* chapter 3, section 3.1, and section 3.2

13. **Magnetic frustration in rare-earth zirconates $A_2Zr_2O_7$, the case of laser heated pedestal method synthesised A = Er, Tm, Yb, and Lu single crystals**

    Klicpera, M., Staško, D., Vlášková, K., Hájek, F., Vojtasová, D., Zelenka, J., Colman, R.H.

    ***J. Alloys Comp.* 978**, 173440 (2024)

    DOI: 10.1016/j.jallcom.2024.173440

    ♠ *MK's contribution:* 70%; conceptualisation, sample synthesis, specific heat analysis, manuscript writting and editing

    ♣ *introduced by thesis sections:* chapter 2, section 2.3, chapter 4, section 4.1, and section 3.2

14. **Low-temperature properties of magnetically frustrated rare-earth zirconates $A_2Zr_2O_7$**

    Vojtasová, D., Staško, D., Hájek, F., Colman, R.H., Klicpera, M.

    J. Phys.: Conden. Matter, accepted manuscript (2024)

    DOI: 10.1088/1361-648X/ad483f

♠ *MK's contribution:* 70%; conceptualisation, sample synthesis, specific heat analysis, manuscript writting and editing

♣ *introduced by thesis sections:* chapter 4, and section 4.1

15. **The Synthesis of the Rare Earth $A_2Zr_2O_7$ single crystals by Simplified Laser-Heated Floating Hot Zone and pedestal methods**

Staško, D., Vlášková, K., Vojtasová, D., Hájek, F., Král, P., Colman, R.H., Klicpera, M.

SSRN, manuscript very recently accepted to ***Materials Today Chemistry*** (2024)

DOI: 10.2139/ssrn.4684275

♠ *MK's contribution:* 80%; conceptualisation, sample synthesis, neutron and synchrotron X-ray diffraction experiments and analysis, manuscript writting and editing

♣ *introduced by thesis sections:* chapter 2, section 2.3, chapter 4, and section 4.2

16. **Robustness of the pyrochlore structure in rare-earth $A_2Ir_2O_7$ iridates and pressure-induced structural transformation in IrO_2**

Staško, D., Vlášková, K., Kancko, A., Többens, D.M., Daisenberger, D., Garbarino, G., Colman, R.H., Klicpera, M.

arXiv, manuscript under review in ***Ceramics International*** (2024)

DOI: 10.48550/arXiv.2403.00477

♠ *MK's contribution:* 40%; sample synthesis, synchrotron X-ray diffraction experiments, manuscript writting and editing

♣ *introduced by thesis sections:* chapter 2, section 2.1, chapter 3, and section 3.1

17. **Local structure of the defect fluorite heavy rare-earth zirconates revisited**

Colman, R.H., Kowalski, P., Vlášková, K., Keen, D., Connolly, E., Chater, P., Klicpera, M.

to be published in 2024, very preliminary draft of the manuscript is printed at the end of the present thesis

♠ *MK's contribution:* 35%; sample synthesis, synchrotron X-ray diffraction experiments, manuscript writting and editing

♣ *introduced by thesis sections:* chapter 2, section 2.3, chapter 4, and section 4.2

7. Published manuscripts ¶

The publications listed in the previous chapter are printed below in the same order.

The publications are inserted in pdf format as published in scientific journals, which results in different format and possibly worse printed quality of following text compared to the body of the habilitation thesis.

Removed from this version of habilitation thesis.